



LIBRARY Michigan State University

This is to certify that the

dissertation entitled

CHARACTERIZING THE LOW-ORDER FRICTION DYNAMICS IN A FORCED OSCILLATOR

presented by

Jin-Wei Liang

has been accepted towards fulfillment of the requirements for

Ph.D. degree in Mechanical Engineering

Date May 20, 1996

MSU is an Affirmative Action/Equal Opportunity Institution

0-12771

PLACE IN RETURN BOX to remove this checkout from your record. TO AVOID FINES return on or before date due.

DATE DUE	DATE DUE	DATE DUE

MSU is An Affirmative Action/Equal Opportunity Institution ctoircidatedus.pm3-p.1

CHARACTERIZING THE LOW-ORDER FRICTION DYNAMICS IN A FORCED OSCILLATOR

 $\mathbf{B}\mathbf{y}$

Jin-Wei Liang

A DISSERTATION

Submitted to
Michigan State University
in partial fulfillment of the requirements
for the degree of

DOCTOR OF PHILOSOPHY

Department of Mechanical Engineering

1996

ABSTRACT

CHARACTERIZING THE LOW-ORDER FRICTION DYNAMICS IN A FORCED OSCILLATOR

By

Jin-Wei Liang

This thesis is devoted to the study of low-order friction dynamics. It applies an air-track system for isolating the source of friction and compares direct and indirect friction measurements, which are the two most common measuring methods. It has shown that the air-track system can efficiently isolate friction source. The comparison between direct and indirect friction measurements indicates that the indirect approach reveals more transient dynamics and random sound noise caused by the air-track system. However, both friction measurements are consistent in the macroscopic motion features as well as the friction level.

A compliant, massless contact model is then used to describe the friction dynamics of the direction-reversal event for a steel-on-steel contact problem. We analytically predict elasto-frictional behaviors in both macroscopic pure-sliding and stick-slip motions. The compliant contact model captures most of the direction-reversal friction dynamics of our experimental system, including the spring-like feature in the macroscopic sliding motion and the transition oscillation during a macroscopic stick-slip process. The wavelet transform is then applied to characterize the transition behaviors of a stick-slip process for both experimental and simulated acceleration signals.

The thesis then investigates the sliding instability that induces frictional noise. An

experimental linear-bearing system is adopted for this study. We first identify damping characteristics of the linear-bearing system by proposing a decrement method. The new decrement method can simultaneously estimate viscous and Coulomb damping. Numerical and experimental verifications show the reliability and feasibility of this decrement method. The squeak of a rubber-on-steel contact problem is explored using the linear-bearing system. A basic squeak mechanism for this rubber-on-steel contact problem is proposed based on the experimental observations.

To my parents and my wife

ACKNOWLEDGMENTS

I am deeply grateful to many who helped me in the completion of this thesis. First, I would like to express my sincere gratitude to my advisor, Professor Brian Feeny, for his friendship and excellent guidance. His insight in nonlinear dynamics and friction problems have been invaluable in helping me complete this study. I am also indebted to him for the endless discussions of many research details. Next, I thank the other members of my thesis committee, Professors Alan Haddow, Charles MacCluer, Clark Radcliffe, David Yen, and Steven Shaw, for their many valuable suggestions to my research work. I am always happy to be a member of the dynamics/control group since this group has an outstanding research atmosphere.

A special appreciation goes to Dr. Jen Her and Dr. Henry Hsieh of Ford Motor Co. They provided a grant to investigate the squeak problem in automobiles. This problem broadened my research to industrial applications. I am also grateful to senior technician, Robert Rose, for his help in setting up the experiment and his ideas in dealing with electronics.

My last four years of studying in M.E. Department were enjoyable. It is my great colleagues who accompanied me day and night in the nonlinear dynamics laboratory. Among these people, Rocky (Shy-Leh Chen) has enlightened my mind such that many mathematics-related problems can be conquered. Ramana Kappagantu, who helped me in many computer problems, is appreciated. James (Cheng-Tang Lee) introduced Latex and Lasoda packages to me and helped me with some latex skills. Other colleagues, Ching-Ming Yuan, Wei Li, C. P. Chao, Tanner Önsay, Chris Hause,

and Sachin Gogate, shared their valuable research experiences with me. I would like to express my appreciation to all of these wonderful colleagues.

My parents did not have a chance for a formal education. However they always encourage me in my attempts to further educate myself. My wife, Shu-Ming, joined my parents' effort after we were married. She dedicates herself in supporting my study and taking care of my daughters. Jo-Hua and Jo-Han, my lovely daughters, always give me a lot of fun. It is these people who give me emotional support during my stay in the "cold" Michigan. Without them, I would never be able to finish my Ph.D.

I have been financially supported through TA opportunities by M.E. Department for which I am grateful. I am especially indebted to MingChi Institute of Technology (Taiwan) who provided the chance and financial aid for my overseas study.

TABLE OF CONTENTS

LIST OF FIGURESiz
LIST OF TABLESxv
LIST OF APPENDICESxvi
CHAPTER
1. INTRODUCTION
1.1 Contributions of This Thesis
1.2 Thesis Overview
1.3 General Statement
1.4 Modeling of Dry Friction in Mechanical Systems
1.5 Stick-Slip Process
1.6 The Comparison of Direct and Indirect Friction Measurements
1.7 Effects of Tangential Contact Stiffness on a Harmonically Forced
Oscillator: Pure Sliding Motion
1.8 Effects of Tangential Contact Stiffness on a Harmonically Forced
Oscillator: Stick-Slip Motion
1.9 Characterizing Stick-Slip Process Using Wavelet Transform 13
1.10 A Decrement Method for the Simultaneous Estimation of
Coulomb and Viscous Friction
1.11 Squeak Criterion10
2. THE COMPARISON OF DIRECT AND INDIRECT
FRICTION SIGNALS

	2.1 Introduction
	2.2 Apparatus and Instrumentation
	2.3 Phase Relationships between Accelerometer and LVDT Signals23
	2.4 The Comparison of Friction Signals27
	2.5 Sensor Dynamics
	2.6 Conclusions
3.	THE EFFECTS OF TANGENTIAL CONTACT STIFFNESS
	ON A HARMONICALLY FORCED OSCILLATOR: PURE
	SLIDING MOTION
	3.1 Introduction
	3.2 A Harmonically Forced Coulomb Oscillator
	3.3 The Idealized Tangential Contact Model
	3.4 Transition Features in f - \dot{x} Plots
	3.5 Experiments in Macroscopic Sliding Motion
	3.5.1 Extraction of the Contact Stiffness
	3.5.2 The Estimations of the Transition Speeds
	3.6 Numerical Studies53
	3.7 Summary
4.	THE EFFECTS OF TANGENTIAL CONTACT STIFFNESS
	ON A HARMONICALLY FORCED OSCILLATOR:
	STICK-SLIP MOTION 62
	4.1 Introduction
	4.2 The Transition Oscillations in a Experimental Stick-Slip Process . 64
	4.3 Numerical Investigations of Stick-Slip Phenomenon
	4.4 Numerical Investigations of the State-Variable Friction Model 74
	4.5 Micro Stick-Slip in a Compliant Contact with Inertia Effect82

	4.5.1 Modeling of the Compliant-Inertial Contact Problem82
	4.5.2 Numerical Simulations of Microscale Stick-Slip Motion 85
	4.6 Conclusions92
5.	WAVELET ANALYSIS OF STICK-SLIP IN AN OSCILLATOR
	WITH DRY FRICTION95
	5.1 Introduction
	5.2 Wavelet Transform
	5.3 Wavelet Analysis of Stick-Slip Signals
	5.4 Conclusions
6.	ESTIMATING COULOMB AND VISCOUS FRICTION
	FROM FREE-VIBRATION DECREMENTS 114
	6.1 Introduction
	6.2 Free Vibration with Coulomb and Viscous Damping116
	6.3 Numerical Solutions
	6.4 Experiments on Systems I
	6.4.1 Experiments on MKC and MKF Systems
	6.4.2 Identification of the MKCF Systems
	6.5 Experimental System II: A Linear Bearing System
	6.6 Error Analysis
	6.6.1 Bounds on Estimation Errors
	6.6.2 Numerical Examples
	6.7 Conclusions
7.	SQUEAK CRITERION OF A RUBBER-ON-STEEL
	CONTACT 150
	7.1 Introduction
	7.2 Features in f - \dot{x} Plots

	7.3 Coupling Between Subsystems	160
	7.4 Discussions and Conclusions	165
8.	CLOSING REMARKS	167
	8.1 Conclusions	167
	8.2 Future Works	173
APPEN	NDICES	176
	A. THE MOVING AVERAGE METHOD	176
	B. DISCHARGE CHARACTERISTIC OF LOAD CELL	179
	B.1 Discharge Time Constant	179
	B.2 Decay Rate in the Low-Frequency Signal	180
BIBLIC	OGRAPHY	182

LIST OF FIGURES

<u>Figure</u>	
2.1 Schematic diagram of the experimental apparatus	20
2.2 Free vibration response for a mass-spring system without external friction and base excitation	21
2.3 Free vibration results without external friction and excitation, f1: the experimental spring force= $kS_1(t)$; f2: the experimental inertial force= $mS_2(t+\tau)$.	22
2.4 Forced vibration results without external friction, excitation frequency = 3 Hz; f1: the experimental spring force= $kS_1(t)$; f2: the experimental inertial force= $mS_2(t+\tau)$; f3: the experimental excitation force= $kS_3(t)$	23
2.5 Forced vibration results without external friction, excitation frequency = 10 Hz; f1: the experimental spring force= $kS_1(t)$; f2: the experimental inertial force= $kS_2(t+\tau)$; f3: the experimental excitation force= $kS_3(t)$	25
2.6 Forced vibration results without external friction, excitation frequency = 20 Hz; f1: the experimental spring force= $kS_1(t)$; f2: the experimental inertial force= $mS_2(t+\tau)$; f3: the experimental excitation force= $kS_3(t)$	26
2.7 Time domain comparison of direct and indirect friction measurements, excitation frequency = 3.5 Hz, stable pure sliding case, in (a) f1: the experimental spring force= $kS_1(t)$; f2: the experimental inertial force= $mS_2(t+\tau)$; f3: the experimental excitation force= $kS_3(t)$; (b) F(t) is the calculated friction force; (c) F1(t) is the averaged version of F(t); (d) F2(t) represents the load cell measurement after averaging	27
2.8 Time domain comparison of direct and indirect friction measurements, excitation frequency = 5.5 Hz, stable pure sliding case, in (a) f1: the experimental spring force= $kS_1(t)$; f2: the experimental inertial force= $mS_2(t+\tau)$; f3: the experimental excitation force= $kS_3(t)$; (b) F(t) is the calculated friction force; (c) F1(t) is the averaged version of F(t); (d) F2(t) represents the load cell measurement after averaging	28
2.9 Time domain comparison of direct and indirect friction measurements, excitation frequency = 7.5 Hz, stable pure sliding case, in (a) f1: the experimental	

spring force= $kS_1(t)$; f2: the experimental inertial force= $mS_2(t+\tau)$; f3: the experimental excitation force= $kS_3(t)$; (b) F(t) is the calculated friction force; (c) F1(t) is the averaged version of F(t); (d) F2(t) represents the load cell measurement after averaging	29
2.10 Time domain comparison of direct and indirect friction measurements, excitation frequency = 3.5 Hz, stick-slip motion case, in (a) f1: the experimental spring force= $kS_1(t)$; f2: the experimental inertial force= $mS_2(t+\tau)$; f3: the experimental excitation force= $kS_3(t)$; (b) F(t) is the calculated friction force; (c) F1(t) is the averaged version of F(t); (d) F2(t) represents the load cell measurement after averaging	30
2.11 Results of impact test: (a) acceleration response; (b) friction force response; (c) power spectrum of acceleration response; (d) power spectrum of friction response	31
3.1 A schematic diagram showing the massless compliant contact model	38
3.2 Hypothetical responses of the idealized model. Dashed lines indicate the gross sliding phase and solid lines correspond to the microsticking phase	39
3.3 A schematic diagram showing the f - x relationship in an "ideal" compliant contact during harmonic motion of the sliding mass. Dashed and solid lines correspond to sliding and microsticking phases	40
3.4 A schematic diagram showing the f - \dot{x} relationship in a compliant contact during harmonic motion of the sliding mass. Dashed and solid lines correspond to sliding and microsticking phases	41
3.5 A schematic diagram showing the f - x relationship in a compliant contact during harmonic motion of the sliding mass, for $f_s > f_k$. Dashed and solid lines correspond to sliding and microsticking phases	42
3.6 A schematic diagram showing the f - \dot{x} relationship in a compliant contact during harmonic motion of the sliding mass, for $f_s > f_k$. Dashed and solid lines correspond to sliding and microsticking phases	
3.7 Schematic diagrams showing (a) the Stribeck friction characteristic for a rigid contact, and (b) the f - \dot{x} relationship and (c) the f - x relationship in an "ideal" compliant contact during harmonic motion of the sliding mass. Dashed and solid lines correspond to sliding and microsticking phases	
3.8 Experimental sliding motion with 5.61Hz excitation: time-domain responses of (a) displacement, (b) velocity, (c) friction force, and (d) acceleration	45
3.9 Experimental sliding motion with 5.61 Hz excitation: (a) time-domain response of displacement, (b) power spectrum of the displacement response shown	

in linear scale, and (c) power spectrum shown in logarithmic scale	46
3.10 Experimental sliding motion with 8.7 Hz excitation: responses of (a) displacement, (b) velocity, (c) acceleration, and (d) friction force	47
3.11 Experimental sliding motion with 11.1Hz excitation: responses of (a) displacement, (b) velocity, (c) acceleration, and (d) friction force	48
3.12 Experimental f - x and f - \dot{x} characteristics for 5.61Hz excitation: (a) detail of sticking in f - x plot, (b) f - x characteristics, (c) detail of sticking in f - \dot{x} plot, and (d) f - \dot{x} characteristics	50
3.13 Experimental f - x and f - \dot{x} characteristics for 8.7 Hz excitation: (a) detail of sticking in f - x plot, (b) f - x characteristics, (c) detail of sticking in f - \dot{x} plot, and (d) f - \dot{x} characteristics	51
3.14 Experimental f - x and f - \dot{x} characteristics for 11.1 Hz excitation: (a) detail of sticking in f - x plot, (b) f - x characteristics, (c) detail of sticking in f - \dot{x} plot, and (d) f - \dot{x} characteristics	52
3.15 Experimental f - x and f - \dot{x} characteristics for 11.1 Hz excitation: (a) detail of sticking in f - x plot, (b) f - x characteristics, (c) detail of sticking in f - \dot{x} plot, and (d) f - \dot{x} characteristics	53
3.16 Numerical simulations of the pure sliding motion (ω =5.61 Hz) with the tangential contact model, responses of: (a) displacement, (b) velocity, (c) acceleration, and (d) friction force	56
3.17 Numerical simulations of the pure sliding motion (ω =8.7 Hz) with the tangential contact model, responses of: (a) displacement, (b) velocity, (c) acceleration, and (d) friction force	57
3.18 Numerical simulations of the pure sliding motion (ω =11.1 Hz) with the tangential contact model, responses of: (a) displacement, (b) velocity, (c) acceleration, and (d) friction force	58
3.19 Simulation of tangential contact model (ω =5.61 Hz), numerical versions of: (a) zoom-in detail of sticking in f - x characteristic, (b) f - x plot, (c) zoom-in detail of sticking in f - \dot{x} plot, and (d) f - \dot{x} characteristic	60
3.20 Simulation of tangential contact model (ω =8.7 Hz), numerical versions of: (a) zoom-in detail of sticking in f - x characteristic, (b) f - x plot, (c) zoom-in detail of sticking in f - \dot{x} plot, and (d) f - \dot{x} characteristic	60
3.21 Simulation of tangential contact model ($\omega=11.1$ Hz), numerical versions of: (a) zoom-in detail of sticking in f - x characteristic, (b) f - x plot, (c) zoom-in detail of sticking in f - \dot{x} plot, and (d) f - \dot{x} characteristic.	61

4.1 Experimental stick-slip motion with 2.5 Hz excitation: time-domain responses of (a) displacement, (b) velocity, (c) acceleration, and (d) friction force.	65
4.2 Results of free-vibration test: (a) friction force time-domain response, (b) acceleration time-domain response, and (c) power spectrum of friction force signal	66
4.3 Experimental f - x and f - \dot{x} characteristics with stick-slip process: (a) zoomin detail of sticking in f - x plot (b) f - x characteristics (c) zoom-in detail of sticking in f - \dot{x} plot (d) f - \dot{x} characteristics	68
4.4 Numerical simulations of stick-slip phenomenon with tangential contact model, case 1, responses of: (a) displacement, (b) velocity, (c) acceleration, and (d) friction force	69
4.5 Simulation of tangential contact model, case 1, numerical versions of: (a) zoom-in detail of sticking in f - x characteristic, (b) f - x plot, (c) zoom-in detail of sticking in f - \dot{x} plot, and (d) f - \dot{x} characteristic	70
4.6 Numerical simulations of stick-slip phenomenon with tangential contact model, case 2, responses of: (a) displacement, (b) velocity, (c) acceleration, and (d) friction force	71
4.7 Simulation of tangential contact model, case 2, numerical versions of: (a) zoom-in detail of sticking in f - x characteristic, (b) f - x plot, (c) zoom-in detail of sticking in f - \dot{x} plot, and (d) f - \dot{x} characteristic	72
4.8 Numerical simulations of stick-slip phenomenon with the state-variable friction model, responses of: (a) displacement, (b) velocity, (c) acceleration, and (d) friction force	75
4.9 Numerical simulations of stick-slip phenomenon with the state-variable friction model, numerical versions of: (a) zoom-in detail of sticking in f - x characteristic, (b) f - x plot, (c) zoom-in detail of sticking in f - \dot{x} plot, and (d) f - \dot{x} characteristic	76
4.10 Numerical simulations of pure-sliding motion with the state-variable friction model, $\omega = 5.61$ Hz, responses of: (a) displacement, (b) velocity, (c) acceleration, and (d) friction force	78
4.11 Simulation of the state-variable friction model, pure-sliding motion, $\omega = 5.61$ Hz, numerical versions of: (a) zoom-in detail of sticking in f - x characteristic, (b) f - x plot, (c) zoom-in detail of sticking in f - \dot{x} plot, and (d) f - \dot{x} characteristic.	79
4.12 Numerical simulations of pure-sliding motion with the state-variable friction model, $\omega = 8.7$ Hz, responses of: (a) displacement, (b) velocity, (c) acceleration, and (d) friction force	80

4.13 Simulation of the state-variable friction model, pure-sliding motion, $\omega = 8.7$ Hz, numerical versions of: (a) zoom-in detail of sticking in f - x characteristic, (b) f - x plot, (c) zoom-in detail of sticking in f - \dot{x} plot, and (d) f - \dot{x} characteristic.
4.14 A schematic diagram showing a contact with both compliance and inertia effects
4.15 Numerical simulations of micro-scale stick-slip phenomenon, responses of the normalized: (a) relative displacement, (b) relative velocity, (c) displacement of the contact, and (d) velocity of the contact; case 1
4.16 Numerical simulations of micro-scale stick-slip phenomenon, responses of the normalized: (a) relative displacement, (b) relative velocity, (c) displacement of the contact, and (d) velocity of the contact; case 2
4.17 Sticking boundaries and double sticking events, (a) macroscopic sticking boundary, $\tilde{y}_s(\tau)$ (dashed line), and $y(\tau)$ (solid line) and (b) microscale sticking boundary $\tilde{y}'_{ms}(\tau)$ (dashed line) and $y'(\tau)$ (solid line); case 2
4.18 Phase portraits of (a) relative coordinate and (b) coordinate of the contact point; case 1
4.19 Phase portraits of (a) relative coordinate and (b) coordinate of the contact point; case 2
5.1 Representations of Morlet wavelet function: (a) real part of $h(t)$ (b) imaginary part of $h(t)$ (c) Fourier transform $H(\omega)$
5.2 Window representations in the time-frequency plane: (a) Fourier transform (b) STFT (c) wavelet transform
5.3 Wavelet transform of an impulse signal: (a) input signal (b) wavelet contour plot
5.4 Wavelet transform of a sinusoidal function carrying an impulse signal: (a) input signal (b) wavelet contour plot
5.5 Wavelet analysis of the simulated stick-slip acceleration, Coulomb friction model: (a) time-domain response, and (b) wavelet contour plot 105
5.6 Wavelet analysis of the simulated stick-slip acceleration signal, state-variable friction model: (a) time-domain response, and (b) wavelet contour plot 106
5.7 Wavelet analysis of the simulated stick-slip acceleration, tangential contact model, case 1: (a) time-domain response, and (b) wavelet contour plot 107

5.8 Wavelet analysis of the experimental stick-slip acceleration: (a) time-domain response, and (b) wavelet contour plot
5.9 Wavelet analysis of the simulated stick-slip acceleration, tangential contact model, case 2: (a) time-domain response, and (b) wavelet contour plot 109
5.10 Detailed wavelet analysis of micro stick-slip event, tangential contact model, case 1: (a) time-domain response, and (b) wavelet contour plot
5.11 Detailed wavelet analysis of micro stick-slip event, tangential contact model, case 2: (a) time-domain response, and (b) wavelet contour plot
6.1 Simulated response of MKCF system, solid line: displacement response of MKCF system; dashed line I: amplitude envelopes of the purely viscous system; dashed line II: amplitude envelopes of the purely dry-friction system
6.2 Exponential decay of amplitude difference in the simulated MKCF system, dashed lines: exponential envelopes; "o": amplitude differences ΔX_i 121
6.3 Schematic diagram of system I
6.4 Experimental displacement response of system I (the MKF system), case 1
6.5 Experimental displacement response of system I (the MKF system), case 2
6.6 Experimental displacement response of system I (the MKC system), case 1
6.7 Experimental displacement response of system I (the MKC system), case 2
6.8 Experiment displacement response of system I (the MKCF system), case 1
6.9 Experiment results showing the exponential decay of amplitude differences, system I (the MKCF system), case 1
6.10 Experimental displacement response of system I (the MKCF system), case 2. Comparison between experimental and identified results (solid line: experimental result; dotted line: identified result)
6.11 Experiment results showing the exponential decay of amplitude differences, system I (the MKCF system), case 2
6.12 A schematic diagram showing the experimental setup of system II 132

6.13 Experimental displacement response of system II
6.14 Experiment results showing the exponential decay of amplitude differences, system II
6.15 Comparison between experimental and identified displacement responses of system II (solid line: experimental result; dashed line: identified result) 135
6.16 Simulation of effects of random error: (a) displacement response and (b) zoom-in detail of random error
6.17 Simulation of effects of quantization error: (a) displacement response and (b) zoom-in detail of quantization error
6.18 Simulation of effects of error of sampling process: (a) displacement response and (b) zoom-in detail of sampling error
7.1 The stable sliding motion in rubber-on-steel contact, high normal-load and dry friction interface case (nominal normal load=6.13 N), $\omega = 5$ Hz, response of (a) displacement, (b) velocity, (c) acceleration, and (d) friction force 154
7.2 The unstable sliding motion in rubber-on-steel contact, high normal-load and wet friction interface case (nominal normal load=6.13 N) $\omega=5$ Hz, response of (a) displacement, (b) velocity, (c) acceleration, and (d) friction force 155
7.3 Comparison of the f - x and f - \dot{x} plots between the stable and unstable sliding motions for nominal normal load=6.13 N, (a) f - x and (b) f - \dot{x} characteristics of the stable sliding (dry friction interface), (c) f - x and (d) f - \dot{x} characteristics of the unstable sliding motion (wet friction interface)
7.4 The stable sliding motion in rubber-on-steel contact, low normal-load and dry friction interface case (nominal normal load=1.23 N), $\omega = 5$ Hz, response of (a) displacement, (b) velocity, (c) acceleration, and (d) friction force 157
7.5 The stable sliding motion in rubber-on-steel contact, low normal-load and wet friction interface case (nominal normal load=1.23 N), $\omega = 5$ Hz, response of (a) displacement, (b) velocity, (c) acceleration, and (d) friction force 158
7.6 Comparison of the f - x and f - \dot{x} plots between different interface conditions for nominal normal load=1.23 N, (a) f - x and (b) f - \dot{x} characteristics of the stable sliding motion (dry friction interface), (c) f - x and (d) f - \dot{x} characteristics of the stable sliding motion (wet friction interface)
7.7 A schematic diagram showing the transducers for measuring normal and torsional vibrations, and sound pressure.

7.8 Time-domain responses of (a) tangential acceleration $\ddot{x}(t)$, (b) friction force $f(t)$, (c) sound pressure, and (d) torsional velocity $\dot{\theta}(t)$ during unstable sliding motion, with high normal load and wet friction interface, $\omega = 5$ Hz, sampling rate=10 kHz, the sound pressure signal low-passed with 5 kHz cut-off frequency. 162
7.9 Time-domain responses of (a) normal acceleration $\ddot{y}(t)$, (b) friction force $f(t)$, (c) sound pressure, and (d) torsional velocity $\dot{\theta}(t)$ during unstable sliding motion, with high normal load and wet friction interface, $\omega = 5$ Hz, sampling rate=10 kHz, the sound pressure signal low-passed with 5 kHz cut-off frequency. 163
7.10 Power spectrum of (a) $\ddot{y}(t)$ in Figure 7.9, and (b) $\dot{\theta}(t)$ in Figure 7.9 164
7.11 Power spectrum of (a) friction force in Figure 7.9(b), (b) $\ddot{x}(t)$ in Figure 7.8(a), and (c) sound pressure in Figure 7.9(c)
A.1 Magnitude and phase response of five-point moving average method 177
B.1 A schematic diagram showing the discharge characteristic 180

LIST OF TABLES

$\Gamma_{ m able}$			
3.1]	Extraction of the Effective Contact Stiffness	19	
3.2]	Estimation of the transition speed based on the analysis in Section 3.4 . 5	54	
	Amplitudes of harmonic base excitation (Z_{e1} and Z_{e2} representing the ation values of the tangential contact model and the state-variable model, as \hat{Z}_{e} denoting the experimental values)	59	
3.1]	Extreme excursions in Figure 6.1	20	
	Estimations of MKCF systems (σ represents the standard deviation of each sted and measured values)	25	
6.3	Extreme excursions in Figure 6.16 ($\delta = 0.005$)	38	
8.4]	Estimation errors and bounds for the case of random error ($\delta=0.005$) . 14	10	
8.5]	Extreme excursions in Figure 6.17 ($\delta = 0.001$)	13	
8.6 F	Estimation errors and bounds for the case of quantization error ($\delta=0.001$) 14	13	
6.7]	Extreme excursions in Figure 6.18 ($\delta = 0.0038$)	15	
3.8 0. 003 8	Estimation errors and bounds for the case of sampling-type error ($\delta = 0$)	15	
6.9	Estimation errors and bounds for the case of random error ($\delta=0.005$) . 14	16	
8. 10 I	Estimation errors and bounds for the case of quantization error ($\delta=0.001$) 14	17	
	Estimation errors and bounds for the case of sampling-type error ($\delta = 3$)	17	

LIST OF APPENDICES

<u>Appendix</u>				
A.	THE MOVING AVERAGE METHOD	.76		
В.	DISCHARGE CHARACTERISTIC OF LOAD CELL	79		

CHAPTER 1

INTRODUCTION

1.1 Contributions of This Thesis

The most important contribution of this thesis is the development of an experimental approach that can be used to investigate frictional problems. This approach is applied to systematically explore the frictional dynamics of a two-directional forced oscillator. The contributions include the following:

- Isolating source of friction using an air-track system that generates an excellent environment for friction study and provides a single degree-of-freedom oscillator (Chapter 2)
- Validation of the measurement of friction through the comparison of two commonaccepted approaches (Chapter 2)
- A thorough study of the effects of the tangential, contact stiffness on a harmonically forced oscillator focusing on the direction-reversal event (Chapters 3 and 4)
- Successful establishment of a detecting tool (wavelet analysis) that can identify the occurrence of the elasto-frictional behaviors during a stick-slip process (Chapter 5)

- Development of a new decrement method that can simultaneously estimate dry and viscous damping from a combined-damping system (Chapter 6)
- Development of another anti-friction slider system with damping characteristics provided (Chapter6)
- Suggesting a basic squeak mechanism for a rubber-on-steel contact problem (Chapter 7)

1.2 Thesis Overview

The ultimate goal of this thesis is to experimentally characterize the friction-induced noise problem using the friction-velocity plot. In order to achieve this, a reliable friction measurement is required which calls for a good friction testing setup and a reliable friction record technique.

To isolate the external friction, we introduced an air-track system that possesses extremely low damping. Thus, the external friction that is added to the air-track system can be considered as an isolated force. Damping characteristic of this experimental setup is addressed in Chapter 2. In the same chapter, we also compare two friction measurements, including the application of load cell and the calculation of friction force from the system's ordinary differential equation, to validate the friction measurement that is used in the subsequent studies.

In Chapters 3 and 4, we focus on the interpretation of friction measurement observed in the friction-velocity plot. Two special elasto-frictional phenomena are discussed: the spring-like behavior during the pure-sliding motion and the transition

oscillation during a stick-slip process. These phenomena relate with the direction-reversal event and experience low relative velocity in frictional interface. Thus, the study presented in Chapters 3 and 4 can be treated as investigations of friction in the low-velocity range.

To explain the elasto-frictional behavior in the low-velocity range, an idealized tangential, contact model is examined analytically and numerically. Comparisons between the results of the modeling and the experiment are accomplished. We also explore the state-variable friction model; which over some parameter ranges can generate the transition oscillations. The idealized tangential, contact model can efficiently describe the elasto-frictional behaviors observed, but the state-variable due to the lack of a physical mechanism cannot completely capture the elasto-frictional behavior of the real system.

An important elasto-frictional feature during a stick-slip process is the high-frequency transition oscillation. In order to detect the occurrence of this event, we apply wavelet analysis on the numerical and experimental stick-slip data. This analysis is presented in Chapter 5. The result shows that wavelet analysis is very efficient in detecting the occurrence and representing the features of the transition oscillations.

To continue the development of the experimental friction approach, we proceed to study the friction dynamics in the sliding regime, which has the relative velocity much larger than zero. Because the ultimate application is a noise problem, the air-track system is no longer applicable. This is due to the inherent noise problem of this air-track system. Hence, we develop another anti-friction slider (liner-bearing

system) for the frictional noise study.

Although the linear-bearing system is designed to be free of friction, it contains both dry and viscous damping. To characterize the damping of the linear-bearing system, we propose a new decrement method in Chapter 6. This chapter shows the analytical, numerical and experimental investigations of the new decrement method. Through the study, damping information of the linear-bearing system is identified.

Chapter 7 performs the investigation of the friction dynamics in the sliding regime. The study explores the squeak noise generated in a rubber-on-steel contact due to the sliding instability. Different parameters are varied to examine the possible mechanism that causes the unstable sliding motion. Finally, we suggest a basic squeak mechanism for this rubber-on-steel contact problem.

In Chapter 8, conclusions of this research and several directions of future work are summarized.

1.3 General Statements

Friction is important in many dynamical engineering applications, including those associated with servo-control problems in machine tools and robotics; noise problems in railway, brake, or automobile suspension systems; and wear and heat problems in manufacturing processes or in anti-friction mechanical components. Recent survey articles by Armstrong-Hélouvery et al. [3], Ibrahim [32], [33], and Oden and Martins [54] relating dynamical systems with friction contain hundreds of references. Research activities in this field can be divided into different categories. For example, people in the control community either want to dispose of friction or request

a reliable and simple friction model such that a high-performance controller can be implemented. In contrast, researchers in tribology (lubrication) are interested in understanding the physical process occurring at the friction interface. Their results can be applied to achieve design criterion for improving the performances of mechanical components such as cutting tools or bearings but may be too complicated to be incorporated with control schemes. On the other hand, dynamicists, who know little about tribology, focus on the investigation of the coupling between mechanical systems and friction process. Research results from this field can hopefully help fill the gap between control applications and lubrication studies.

This dissertation belongs to the dynamical regime. It studies the dynamics of mechanical systems with dry friction, with the intent of extracting information about friction dynamics.

The experimental system in this study, in general, has a steel-on-steel contact with engineering finishes and is subjected to two-directional, harmonic excitations. Although most of the previous friction studies that can be found in the survey papers by Armstrong-Hélouvery et al. [3], Ibrahim [32], [33], and Oden and Martins [54] concentrated on unidirectional problems, close-loop control systems often involve oscillating motion with direction reversals. Some but not many two-directional friction studies were reported in the literature; which include, for instance, the experimental works by Den Hartog [15], Marui and Kato [44], and Wojewoda et al. [80] and the analytical works by Den Hartog [15], Hundal [30], and Shaw [69] etc. It is of interest to understand the dependences of friction behaviors on the direction of motion as well as the oscillation frequency.

1.4 Modeling of Dry Friction in Mechanical Systems

While dry friction has been studied for centuries by researchers in different communities through various methods, the process occurring at the friction interface is not yet completely understood. Due to the complexity of the friction process, it is believed that a single and universal friction law is almost impossible to attain. Friction modeling is more-or-less system and task dependent. General considerations address the materials, the geometry, the chemical process, and the motion scale at the friction interface. Research in this area begins with Leonardo da Vinci (1452-1519), who defined friction laws based on direct measurements and addressed the concept of coefficients of friction. Coulomb [12], on the other hand, observed that both static and kinetic friction exist and found that they are almost identical for the metallic contacts. The terms static and kinetic coefficients of friction were proposed by Morin [48].

Even though the Coulomb friction model is reliable in describing some macroscopic frictional behaviors such as the stick-slip phenomenon (Den Hartog [15], Hundal [30], Shaw [69], and Marui and Kato [44]), it is not able to model subtle friction features. These include (1) the frictional memory effect or hysteresis characteristic in the sliding regime (Ibrahim [32], [33], Ruina [66], Dieterich [17], [16]); (2) rate and time dependencies of the static friction (rising static coefficient of friction) (Kato et al. [36], Armstrong-Hélouvry et al. [3]); and (3) influences of normal vibrations (e.g. Tolstoi [75], Oden and Martins [54], Tworzydlo and Becker [76], Tworzydlo et al. [77]).

To supplement the Coulomb friction law, different friction models have been re-

cently proposed. For example, state-variable and time-delay friction models were proposed to accommodate the frictional memory effects (Ruina [66], Hess and Soom [28], and Dieterich [17], [16]). The frictional memory effect manifests itself in a loop structure seen in friction-velocity plot such that the friction in the accelerating phase is higher than that in the decelerating phase during a single motion cycle. An explanation of this phenomenon suggested by Rabinowicz [60] stated that friction is possibly memory dependent. If the steady-state friction decreases as the sliding velocity increases; then during the accelerating phase, the averaged velocity over a proceeding critical distance will be larger than that in the decelerating phase, centering at the same steady-state sliding velocity (Ibrahim [32]). Oden and Martins [54] took the normal vibrations into consideration and developed an elastic constitutive relationship in the friction interface. A striking feature of the resulting friction model is that there will be no loop structure in the friction-velocity relationship if the friction coefficient is taken as the instantaneous ratio of friction force to normal force. In other words, the frictional memory effect vanishes if the dynamics in the normal direction is considered. Some numerical studies applying Oden and Martins' friction model predicted the occurrences of sliding instability caused by the coupling between tangential, normal, and rotational dynamics (Twozrydlo et al. [76], [77]).

New friction models are still developing. For example, Polycarpou and Soom [57] proposed a two-dimensional friction model that included both tangential and normal dynamics. This model was developed according to the observations made from a specific system. Canudas de Wit et al. [10] suggested a friction model that treats the friction interface as the contact between bristles. This model can capture fric-

tion phenomena such as Stribeck effect, spring-like sticking characteristic and the hysteresis effect in sliding regime. Hsu [29] applied identification techniques to a hydraulic actuator system and developed a parameterized friction model. This model can account for unmodeled dynamics caused by the inaccuracy of the physically based equations, the inherent stochastic mechanisms, and the measurement noises that can occur in a real friction process.

Although we will apply a massless, compliant contact model to interpret some experimental friction observations, the main focus of this dissertation is in the study of dynamic friction behaviors rather than the friction modeling.

1.5 Stick-Slip Process

Stick-slip alone is a very important feature of dry friction and has been the focus of many works. It occurs when the relative velocity at sliding interface is zero. The motion tends to be intermittent such that during the sticking phase the static friction balances other forces present, and sliding motion resumes when the static friction cannot sustain the resultant force. The occurance of a stick-slip limit cycle is undesirable in control applications since it may cause the deterioration of controller performance, particularly in the high-accuracy regulating and the low-velocity tracking problems (Armstrong-Héluovry [3], Radcliffe [61], Dupont [19], Southward et al. [70], Brandenburg and Schafer [8], Suzuki and Tomizuka [73], Canudas de Wit et al. [10], Canudas de Wit and Seront [10], and Maqueria and Masten [43]). Furthermore, stick-slip is also a suspected mechanism of high-frequency frictional noise occurring in railway and automobile systems (Nakai and Yokoi [51], Ibrahim [32], [33]).

Many researchers have studied stick-slip phenomenon analytically. For a harmonically excited single degree of freedom (DOF) system with Coulomb friction, Den Hartog [15] solved the steady-state periodic solutions. The steady-state solutions consist of stick-slip processes with various numbers of sticking events per forcing cycle (Den Hartog [15]). Hundal [30] investigated a similar system with harmonic base-excitation motion. His work, incorporated with the Coulomb friction model, yielded closed form solutions with a stable stick-slip process. More recently, Shaw [69] determined the stability of the steady-state periodic solutions and conducted bifurcation studies of system parameters. It is of interest to note that the mechanical friction systems generate not only the stable stick-slip motion but also chaotic behaviors. For example, Popp and Stelter [58] numerically studied a unidirectional belt-drive system incorporated with nonlinear friction characteristic and found a chaotic attractor in their system. The route to chaos in that study tends to be intermittency. Conversely, Feeny and Moon [25] investigated a system with a linearly displacement-dependent friction characteristic. This system, when subjected to harmonic excitations, can exhibit chaotic behaviors with period doubling as the route to chaos. Nevertheless, even a regular stick-slip process can possess abundant dynamics especially at the onset of sticking.

1.6 The Comparison of Direct and Indirect Friction Measurements

Among many techniques that can be used to record friction, the direct employment of load cell and the computation of friction force in accordance with the system's ODE are commonly accepted in literature. However, commercial load cells are limited by resolution and frequency response. They are unable to account for all of the events occurring in the friction interface. The friction signal registered by the load cell is usually attenuated over the high-frequency range since the load cell acts like a low-pass filter.

In contrast to the direct approach, calculating the friction force incorporated with the system's ODE requires more than one transducer. Such a computation approach is called the AVD method by Ko and Brockley in [38] because it involves the direct measurements of acceleration, velocity, and displacement of the moving specimen. This method is liable to error because different sensors typically respond at different speeds leading to a phase shift among transducers. Although the phase shift among different transducers can be regulated by careful calibration work, regarding these two approaches, some interesting issues arise. What will be the difference between the resulting friction signals obtained from direct and indirect methods? Moreover, will the phase shift among transducers depend on the frequency contents of the signal?

These questions will be answered partially in Chapter 2. In order to successfully measure the friction force, the source of friction must be isolated. Isolating friction is nontrivial. To achieve it, we introduce the air track system, which has very small dry-friction effect. The mass of the main system will therefore glide on this air track with an external friction source. Guidelines for interpreting friction signals are obtained through this investigation.

1.7 Effects of Tangential Contact Stiffness on a Harmonically Forced Oscillator: Pure Sliding Motion

Friction depends on several parameters, including relative velocity, normal load, time, temperature, materials, geometry, and roughness of the sliding surfaces. The Coulomb friction model states that the friction force of constant magnitude will alternate sign depending on the direction of the relative velocity of sliding surfaces. In the real world, the friction contact can have compliance at the asperity joints or at the surrounding structures. As a result, there might be an elastic deformation period prior to the sliding motion. This elastic characteristic is termed a "spring-like" sticking behavior by Canudas de Wit et al. [14]. The displacement induced by this elastic deformation is typically small (of the order of a micron) and was denoted as "preliminary displacement", "micro displacement", or "presliding displacement" in the literature (Oden and Martins [54], Canudas de Wit [14], and Harnoy et al. [26]). Although many previous experimental results have indicated its existence, the origin of this elastic component is not clear. It could be the elastic deformation of the specimen or that of the testing apparatus (Oden and Martins [54]).

According to our preliminary experimental experiences, the occurance of the "micro displacement" was observed. Associated with this micro displacement in a harmonically forced system there is certain velocity at which the transition between micro and gross sliding displacements takes place. This specific velocity is shown to be dependent on the oscillation frequency in the case of harmonic excitation. The elasto-frictional (spring-like) characteristic occurring at low velocity manifests itself in a hysteretic structure in friction-velocity plot.

To further study this "spring-like" sticking behavior, a simple compliant contact model is investigated in Chapter 3. Focusing on pure-sliding motion, geometric analysis leads to quantitative and qualitative sticking features. These predictions are verified by experiments and numerical simulations.

1.8 Effects of the Tangential Contact Stiffness on a Harmonically Forced Oscillator: Stick-Slip Motion

Experimental studies on the stick-slip phenomenon often reveal oscillations during the transition from sliding to sticking. The measurements of Marui and Kato [44] showed an oscillation of friction force during the transition phase of stick-slip process, which suggested a dynamical friction behavior. A similar oscillation was observed in a boundary-lubricated system measured by Polycarpou and Soom [56], where both the acceleration and friction force exhibited oscillations in the transition phase. Ko and Brockly [38] focused on measuring dry friction with a unidirectional pin-ondisk apparatus and found such oscillations in their velocity signal. The key feature was that there were high-frequency oscillations superimposed on a low-frequency periodic stick-slip signal. The low-frequency stick-slip response can be obtained by considering a mass-spring system incorporated with a Coulomb friction model. Based on this model, the acceleration response is zero during the sticking interval and has a jump event at each onset of sticking. However, there is no high-frequency transition oscillation occurring in this model. In the real system, the jump in the friction force due to the sticking feature acts like a pulse or step input to the mass-spring system with frictional contact and can excite the coupling dynamics between the main system and contact point. This feature is evident when the contact possesses tangential compliance.

Moreover, a specific state-variable friction model incorporated with the system's ODE can generate similar transition oscillations over some parameter ranges. Features of the simulated transition oscillation of this friction mode resemble those observed in experiments. It appears that the state-variable may be able to capture the transition features of a real system.

In Chapter 4, we apply the massless tangential contact model to interpret the transition oscillation that has been observed in the experimental system. A free-vibration test was conducted to measure the frequency of this transition oscillation. It was found that this experimentally observed frequency matched the prediction based on the tangential, contact model. Furthermore, a double stick-slip event was revealed in both the experimental data and the numerical simulations of the tangential, contact model. This event illustrates the coexistence of the macroscopic and microscopic stick-slip process. Numerical studies focusing on the tangential, contact model can reasonably describe the experimental sticking behaviors, qualitatively and quantitatively.

1.9 Characterizing Stick-Slip Process Using Wavelet Transform

There are modern signal processing techniques that are efficient in dealing with the signals containing both high and low frequency components. Among these techniques, the short-time Fourier transform (STFT) uses a translational window in the time domain and expands the frequency contents with respect to the signal inside the window (Allen and Rabiner [1], Portnoff [59]). Therefore, it can be interpreted as a general Fourier transform with time localization. Due to the uncertainty principle, the resolution in time and frequency of this approach cannot be arbitrarily small and limits the application of this method (Vetterli [78]). The wavelet transform is another candidate for extracting time-frequency information from a signal with a wide range of frequency components (Rioul and Vetterli [64], Williams [79]). The advantage of wavelet transform over the STFT is that it uses a varying window length depending on the frequency contents of the signal, such that it is possible to zoom into different structures in both time and frequency domains. This technique has been introduced in the vibration studies recently and was showed to be efficient for some cases (e.g. Önsay and Haddow [55], Newland [52], [53], Chen and Wang [10], Mooney and Soom [47], Hunt [31], Kishimoto et al. [37]).

Due to the facts that the stick-slip acceleration data have high-frequency events superimposed on the low-frequency periodic response, and the wavelet transform is efficient in extracting time-frequency informations of signals with a wide range of frequency components. An important question is, "Can the wavelet transform be used as a tool to characterize the transition behaviors of stick-slip motion so that the occurance of subsystem/coupling dynamics can be detected?"

An investigation focusing on this question is presented in Chapter 5.

1.10 A Decrement Method for the Simultaneous Estimation of Coulomb and Viscous Friction

One of the motivations of this thesis is the investigation of frictional noise. To

study a noise problem, a quiet environment is required. The air track that we introduced for isolating friction is no longer applicable since there is inherent noise caused by the air sound. This inherent air noise is irreducible because some threshold air pressure is necessary for supporting the sliding mass. Another low-friction element applied widely in friction study is the linear bearing system (Dweib and D'Souza [20], [18] and Aronov et al. [6], [4], [5]). This system is also used in many control applications, particularly in the high-speed position control. We adopt this element for the study of the frictional noise problem. A linear bearing, while designed to be frictionless, is not friction free. In order to identify the dry friction and viscous damping existing in this linear bearing system, a decrement method is proposed in Chapter 6.

The logarithmic decrement method was formulated by Rayleigh in 1877 [62]. The idea, however, goes back to Hermann Helmholtz [27], who applied the logarithmic decrement to determine frequency information in musical tones in 1863. This decrement method can be used to estimate the linear viscous damping effect. In contrast, the constant decrement in free-vibration response due to Coulomb friction was addressed by Lorenz in 1924 [41]. The method considers the constant decrement in successive oscillation amplitudes so as to determine the sliding friction characteristic. Both of these estimation algorithms can be found in a modern vibration textbook such as Meirovitch [46]. However, an analytical prediction algorithm for a system possessing both dry friction and viscous damping effects has not yet been seen. Estimating damping characteristics from this combined-damping system is important since many control schemes call for thorough modeling information, particularly in

the applications of model-referenced adaptive control (Ioannou and Sun [34]). Lack of modeling information certainly deteriorates the performance and robustness of the controller.

Following the existing ideas, a decrement method is developed in Chapter 6 to simultaneously estimate the dry-friction and viscous-damping effects. Numerical and experimental investigations validate this proposed method. The damping characteristics of the linear bearing system are estimated.

1.11 Squeak Criterion

Among the various undesirable friction-induced problems, squeak and squeal in automobile brake and suspension systems have drawn particular attention. This problem is important because the annoyance of the high-frequency noise decreases the enjoyment of driving and ultimately the profits of the automakers. The frictional noise problems are difficult to be solved or prevented because unclear mechanisms and irrepeatability are generally involved in the frictional noise problem.

Various types of frictional noise can be observed in sliding systems. For example, the noise caused by the random surface roughness is usually of low level and is similar to rubbing noise (Nakai and Yokoi [51]). The noise of more importance in applications is the one of high level, referred to as a "screaming noise". This kind of noise is believed to be caused by the friction-induced self-excited vibrations (Nakai and Yokoi [51], Dweib and D'Souza [20], [18], and Aronov et al. [6], [4], [5]). Many mechanisms are suspected to be responsible for friction-induced vibration including stickslip, sprag-slip, negative slope in the friction-velocity relationship and coupling of

degrees of freedom. (Dweib and D'Souza [20], [18], Nakai and Yokoi [51], Tworzydlo et al. [77], Aronovet al. [6], [4], [5], Earles and Lee [21], Spurr [71], Ibrahim [32], [33]). However, the experimental observations reported in literature indicated that the coupling between different degrees of freedom system is prevalent during the occurrence of the sliding instability. This observation is somewhat consistent in the works of Dweib and D'Souza, Aronov et al., Nakai and Yokoi, and Tworzydlo et al. The previous studies also concentrated in the investigations of unidirectional system.

A two-directional, harmonically excited system is considered in Chapter 7. The system has rubber-on-steel contact. Observations focusing on the squeak generation are made to reveal the possible mechanism or criterion for this noise problem. This study is motivated by the squeak problem observed in a automobile stabilizer bar which has a rubber-on-steel contact. Coupling between different degrees of freedom was observed during the squeak generation. Moreover, the negative slope in friction-velocity plot seems to correspond to the existence of sliding instability and frictional noise.

CHAPTER 2

THE COMPARISON OF DIRECT AND INDIRECT FRICTION SIGNALS

2.1 Introduction

Two techniques are commonly adopted for recording friction forces. These are the direct employment of load cell signal and the calculation of friction force from system's governing equation incorporated with the measured motion signals. Installing a load cell to frictional systems is equivalent to adding a mass-spring subsystem to the main system. The dynamical effect of this extra degree of freedom seems to be insignificant because commercial load cells are usually stiff compared to the mechanical friction systems. However, every load cell has its own natural frequency and bandwidth and acts as a low-pass filter on the friction signal. The measured friction force signal will be more or less attenuated over the high-frequency range. Thus, the signal obtained from a load cell may not be able to completely depict actual friction forces.

On the other hand, calculating the friction force from the system's ordinary differential equation (ODE) requires more than one transducer. This approach is therefore liable to parasitic interference and calibration errors. These problems occur because each transducer has it own response which does not coincide absolutely with the

responses of other transducers (Antoniou [2]). Moreover, a smoothening algorithm is often required to handle digital data (e.g. Sakamoto [67], [68], and Dupont and Dunlap [19]) and may affect the apparent friction characteristics.

As a result, the comparison between friction signals from both direct and indirect friction measurements becomes an important issue. While neither method can represent the absolute story of the friction process occurring at the interface, they each partially reveal the process. By combining specific features associated with individual techniques, guidelines for interpreting signals from these methods can be made, as will be the completeness of friction-process information. Such a comparison is carried out in this chapter.

This chapter is organized as follows. The next section describes the experimental instrumentation. In Section 2.3, some vibration tests in the absence of frictional contact were conducted in order to investigate the phase shift between sensors. This information is necessary for the indirect calculation of the friction force. Section 2.4 compares friction signals obtained from direct and indirect techniques. Examined cases include one stick-slip motion and three pure sliding cases with different excitation frequencies. The friction interface is steel-on-steel. The consistencies and discrepancies between the two approaches are demonstrated. In Section 2.5, a frequency response approach is adopted to investigate dynamics associated with different sensors and mountings. Through this investigation, discrepancies occurring in the comparison of direct and indirect friction signals can be explained. Section 2.6 concludes this chapter with some discussions regarding the impact of this study on friction applications.

2.2 Apparatus and Instrumentation

A schematic diagram of the apparatus is presented in Figure 2.1. The apparatus consists of a sliding mass, helical springs, and the friction-contact mechanism. The sliding mass, comprising mostly the inertia of the accelerometer, moves in an air track. Motion in the air track is almost friction free, with a nondimensional viscous damping factor equal to 0.0008. The friction-contact mechanism consists of a pinched-flange structure which is designed for balancing the normal loads on both sliding surfaces.

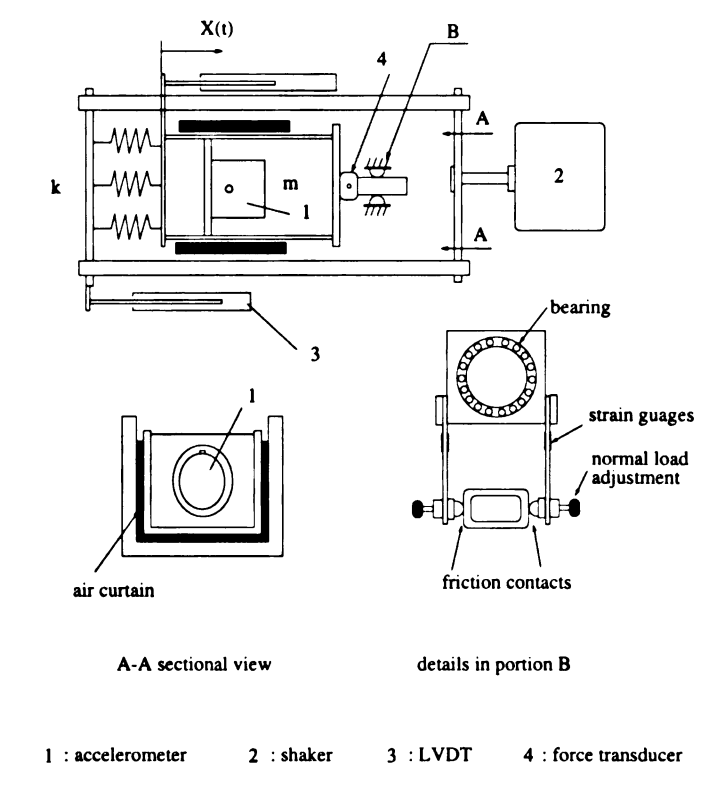


Figure 2.1: Schematic diagram of the experimental apparatus.

The displacements of both the sliding mass and the base excitation were sensed by linear variable differential transformer (LVDT). This LVDT was made by Rabinson-Halpern Co. (Model 210A-0500) and had a resolution of 2.5 μ m after quantization

in the digital data acquisition process. The seismic accelerometer (PCB, Model 393C) was adopted to record the acceleration signal. This accelerometer had a frequency range from 0.025 to 800 Hz with 5% transverse sensitivity. The nominal sensitivity of the accelerometer was 1 volt/g with a resonant frequency of 3.5 kHz. The friction force was measured by a piezoelectric load cell (PCB, Model 208B) which had 0.0002 lb resolution in a range of 10 lb in both tension and compression. The nominal sensitivity was 500 mvolt/lb with a stiffness of 10 lb/ μ in. The discharge time constant of this load cell was 50 sec and the resonant frequency was 70 kHz.

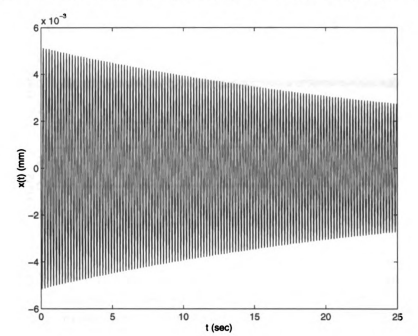


Figure 2.2: Free vibration response for a mass-spring system without external friction and base excitation.

The system was driven by an electromagnetic shaker (LDS, Model 400) associated with a power amplifier/signal generator. This unit was capable of producing a harmonic signal to excite the sliding mass. The lowest operating frequency for which the shaker can produce satisfactory harmonic signal was 1 Hz. The maximum displacement amplitude of the shaker was 8 mm. The friction contact was steel-on-

steel. The planner surfaces were ground and rubbed with 400-grit, silicon-carbide paper. The other contact surfaces had hemispherical geometry and were lathed with an engineering finish then rubbed by the same type of paper. Finally, the surfaces were cleaned by a degreaser (Measurement Group, Inc., Model CSM-1). The surfaces were then engaged in sliding motion for at least 30 minutes to attain a steady-state friction characteristic before the data were recorded.

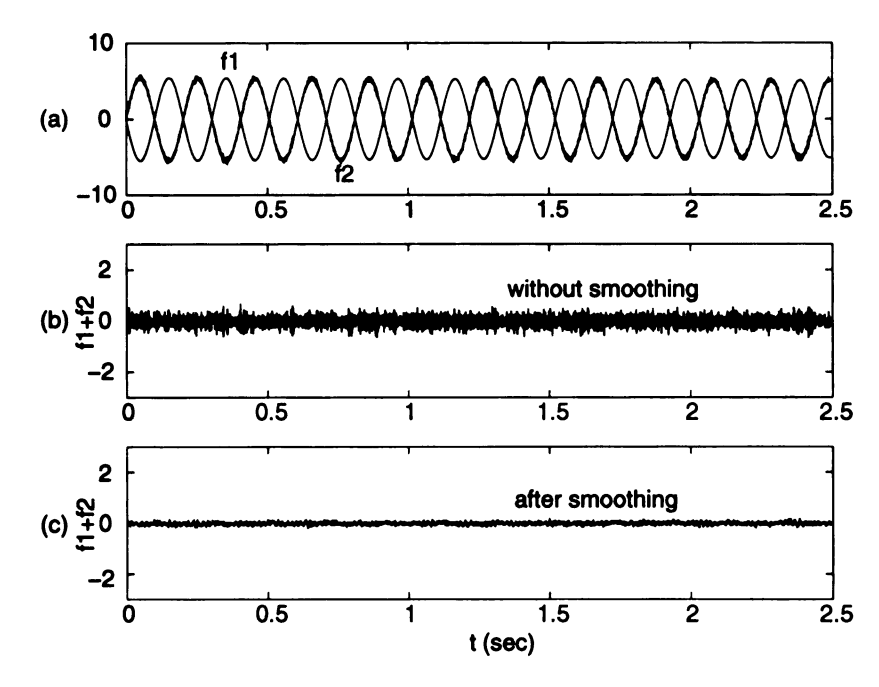


Figure 2.3: Free vibration results without external friction and excitation, f1: the experimental spring force= $kS_1(t)$; f2: the experimental inertial force= $mS_2(t+\tau)$.

In order to gain an idea of how the air track can affect the friction investigation, a free-vibration test, with the base fixed, was carried out in the absence of frictional contact. The result is presented in Figure 2.2. The damping of the mass/spring in the air track is nearly viscous with very little dry friction effect. According to the logarithmic decrement algorithm, the damping factor of the mass and spring in the air track is 0.0008. The spring may also possess internal damping. Thus,

the damping effect shown above can be induced by either the air damping or the material damping. Nevertheless, the damping is quite small and we will neglect this effect in the subsequent studies. Moreover, because the inherent damping of this air-track system is so insignificant compared to the external friction exerted by the pinched-flange mechanism, we will consider that the latter friction is an isolated friction source.

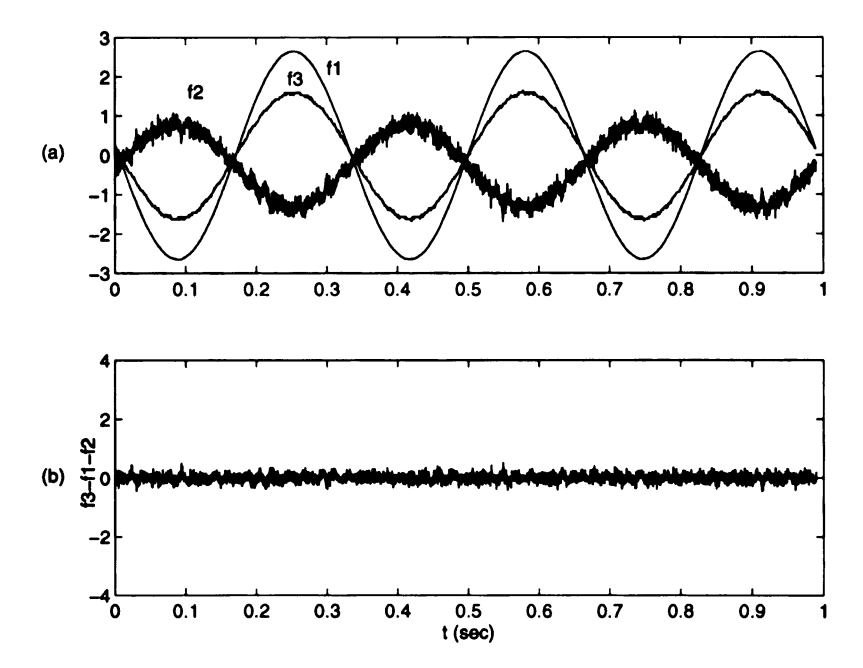


Figure 2.4: Forced vibration results without external friction, excitation frequency = 3 Hz; f1: the experimental spring force= $kS_1(t)$; f2: the experimental inertial force= $mS_2(t + \tau)$; f3: the experimental excitation force= $kS_3(t)$.

2.3 Phase Relationships between Accelerometer and LVDT Signals

Phase shifts between different sensors is always an issue in experimental work. For instance, Ko and Brockly [38] observed a 1-degree phase shift between the acceleration and displacement signals (the response speeds vary among various commercial

transducers). To investigate the phase shift between signals from the accelerometer and LVDT, a free-vibration test for the mass-spring system with the air track was conducted with the base constrained. The results are shown in Figure 2.3. In this figure, the natural frequency (ω_n) of the system is 30.91 rad/sec. The damping in this system is the same as that of Figure 2.2. Due to the small damping effect, the amplitude of oscillation in Figure 2.3(a) decreases slowly.

This free-vibration test involved the balancing of experimental inertial and spring forces. Figure 2.3(a) presents experimental inertial and spring forces during the vibrating process, whereas Figure 2.3(b) presents the resultant force, namely $mS_2(t+\tau)+kS_1(t)$. The measurements of displacement and acceleration are labeled as $S_1(t)$ and $S_2(t)$ respectively. There was a phase shift of $\phi=0.0389$ radians by which the accelerometer signal leads the LVDT signal. This phase angle was converted to a time shift using $\tau=\phi/\omega_n$, and it was chosen such that the resultant force was close to zero with some random noise. The random noise could be induced by the sound and the pressure fluctuation of the air track or another source. In order to have a clearer representation, we smoothened the resultant force signal in Figure 2.3(b) by applying a five-point, moving-average algorithm (see Appendix A) and obtained the data shown in Figure 2.3(c). Both raw and smoothened data illustrate the cancelation of spring and inertial forces.

A reasonable question for this investigation might be, "Can this force balance hold for a wide range of excitation frequency? In other words, will the time (phase) shift be affected by excitation frequency?" It is conceivable that such a phase shift will depend on the excitation to some extent. However, by carefully calibrating the transducers,

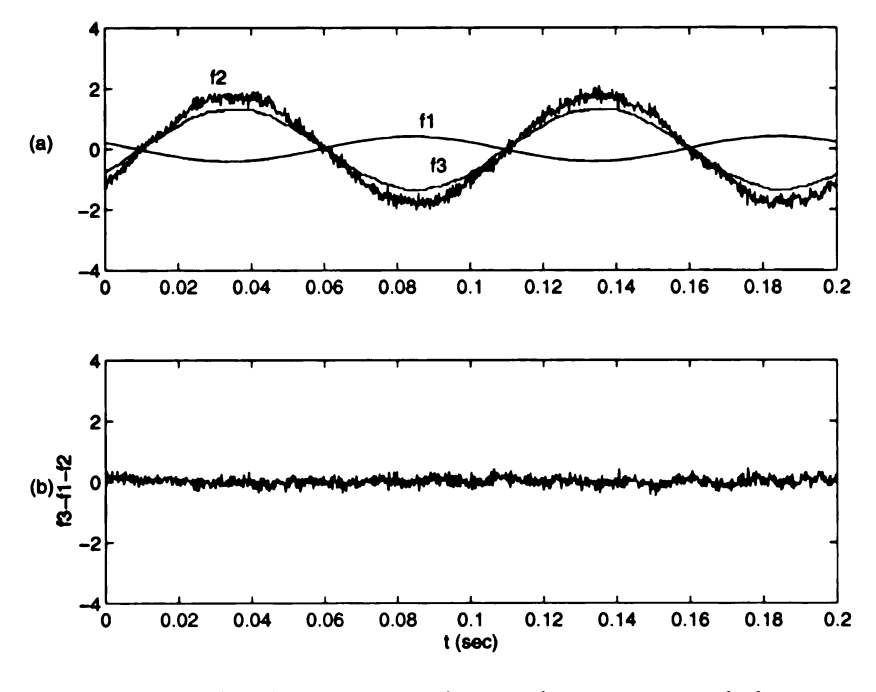


Figure 2.5: Forced vibration results without external friction, excitation frequency = 10 Hz; f1: the experimental spring force= $kS_1(t)$; f2: the experimental inertial force= $mS_2(t+\tau)$; f3: the experimental excitation force= $kS_3(t)$.

the results are promising. Figures 2.4-2.6 present three cases in which harmonic base excitations were applied without the presence of external dry friction. Under these situations, the equation which we are trying to balance is $mS_2(t+\tau)+kS_1(t)\approx kS_3(t)$, where $S_3(t)$ denotes the measurement of the base-excitation motion with different frequencies (3, 10, 20 Hz here). As with the case shown in Figure 2.3, experimental force components such as inertial, spring, and excitation forces are shown in Figures 2.4-2.6(a). The resultant forces, $kS_3(t)-kS_1(t)-mS_2(t+\tau)$, for different excitation frequencies, are presented in Figures 2.4-2.6(b). There was no smoothing process applied to these data and the same time shift, τ , was employed in the calculation of resultant forces.

Observations made from Figures 2.4-2.6 imply that the dependence of the phase

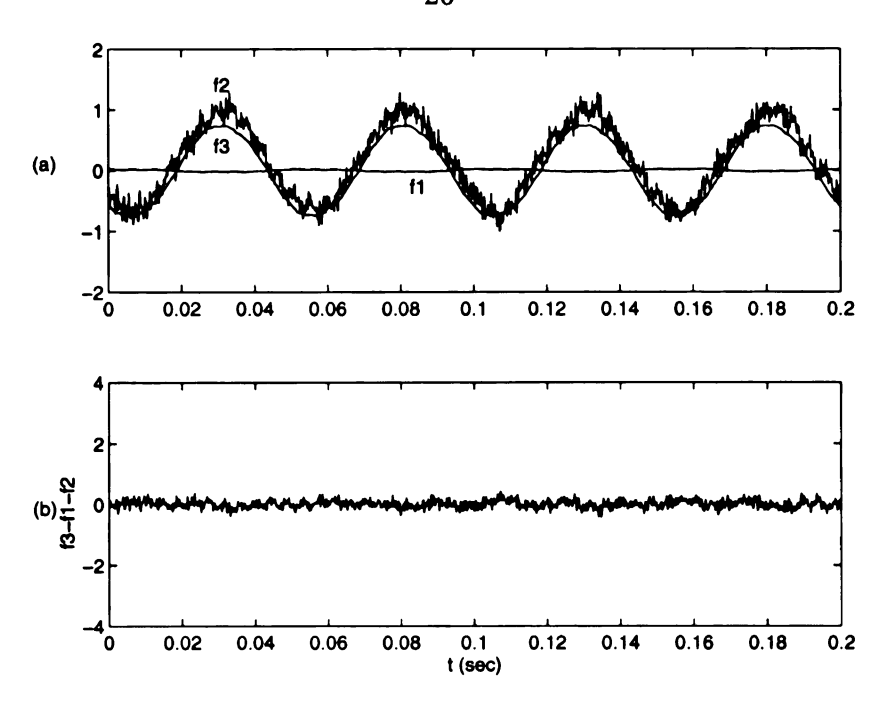


Figure 2.6: Forced vibration results without external friction, excitation frequency = 20 Hz; f1: the experimental spring force= $kS_1(t)$; f2: the experimental inertial force= $mS_2(t+\tau)$; f3: the experimental excitation force= $kS_3(t)$.

shift on the excitation frequency is not serious over a reasonable range. The LVDT chosen in this study is incorporated with signal conditioner. The response speed of LVDT itself over a reasonable frequency range is therefore a constant. Without signal conditioning, the response speed of LVDT cannot be controlled, thus there will be no guarantee for a constant phase angle. On the other hand, the phase angle of accelerometer can be presumed to be approximately equal to zero if one considers that the resonant frequency of the accelerometer is 3.5 kHz and the operating frequency range for this study is limited to 20 Hz. We did not check excitation frequencies higher than 20 Hz because that the actuator was not able to sustain a large enough response in $S_1(t)$ required for quantization purposes during high-frequency excitations.

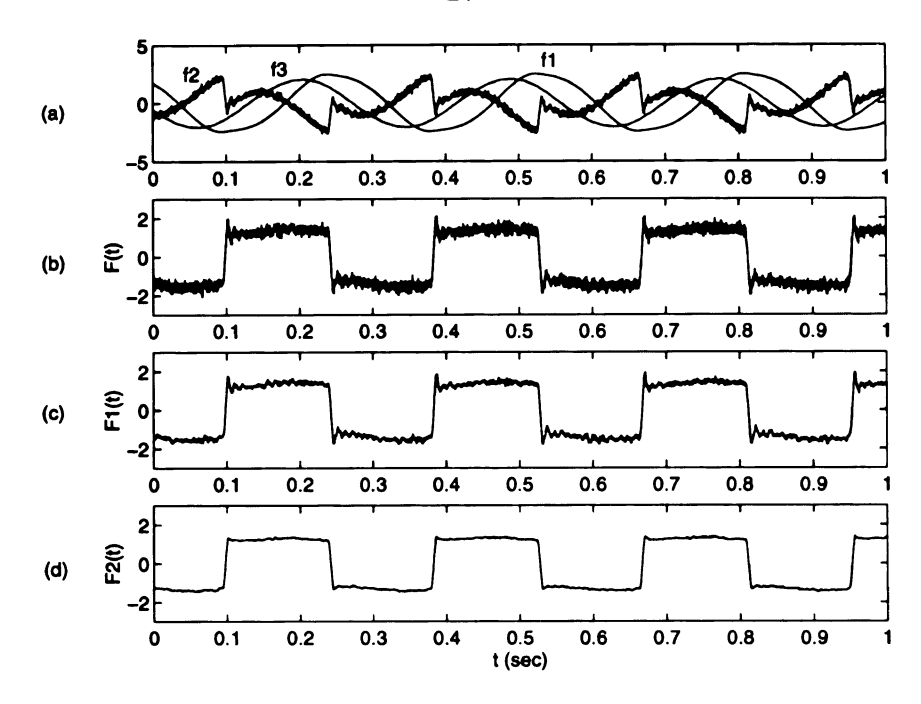


Figure 2.7: Time domain comparison of direct and indirect friction measurements, excitation frequency = 3.5 Hz, stable pure sliding case, in (a) f1: the experimental spring force= $kS_1(t)$; f2: the experimental inertial force= $mS_2(t+\tau)$; f3: the experimental excitation force= $kS_3(t)$; (b) F(t) is the calculated friction force; (c) F1(t) is the averaged version of F(t); (d) F2(t) represents the load cell measurement after averaging.

2.4 The Comparison of Friction Signals

As mentioned in Section 2.1, the friction force can be acquired either from the direct employment of a load cell or the indirect calculation based on the system's ODE. For direct measurements, a piezoelectric load cell which had resonant frequency at 70 kHz was applied. Since this load cell has a high resonant frequency, zero phase shift between acceleration and friction signals is assumed in implementing the comparison between the two approaches. The external friction source induced by the pinched-flange mechanism will be exerted on the mass-spring system during the test process hereafter.

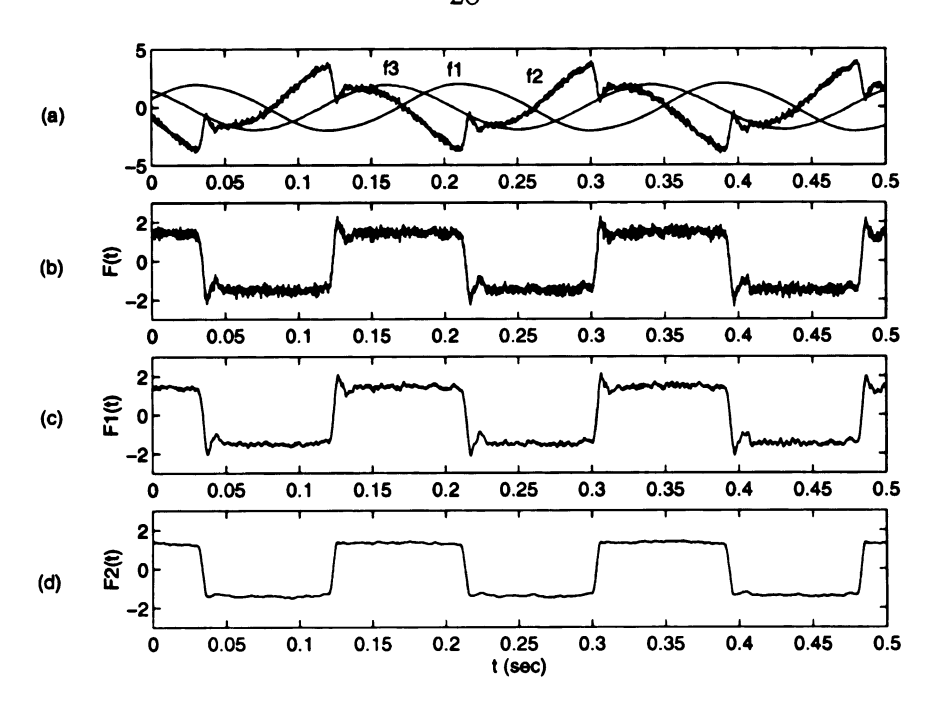


Figure 2.8: Time domain comparison of direct and indirect friction measurements, excitation frequency = 5.5 Hz, stable pure sliding case, in (a) f1: the experimental spring force= $kS_1(t)$; f2: the experimental inertial force= $mS_2(t+\tau)$; f3: the experimental excitation force= $kS_3(t)$; (b) F(t) is the calculated friction force; (c) F1(t) is the averaged version of F(t); (d) F2(t) represents the load cell measurement after averaging.

To calculate friction force from system's equation of motion, namely $F(t) = kS_3(t) - kS_1(t) - mS_2(t+\tau)$, motion signals such as $S_1(t), S_2(t)$, and $S_3(t)$ are required. An accelerometer and two LVDTs are used for such measurements. System parameters have the values m = 2.42 kg and k = 2310 N/m. The phase shift between $S_1(t)$ (or $S_3(t)$) and $S_2(t)$ (or $F_2(t)$) are the same as in previous case, i.e $\phi = 0.0389$ radians. Four frictional vibration tests were carried out for the comparison. These include one stick-slip process and three pure-sliding cases with different excitation frequencies. Results are presented in Figures 2.7-2.10.

Figure 2.7(a) illustrates the time-domain histories of the experimental inertial forces, $mS_2(t+\tau)$, spring force, $kS_1(t)$, and the base-excitation force, $kS_3(t)$. The

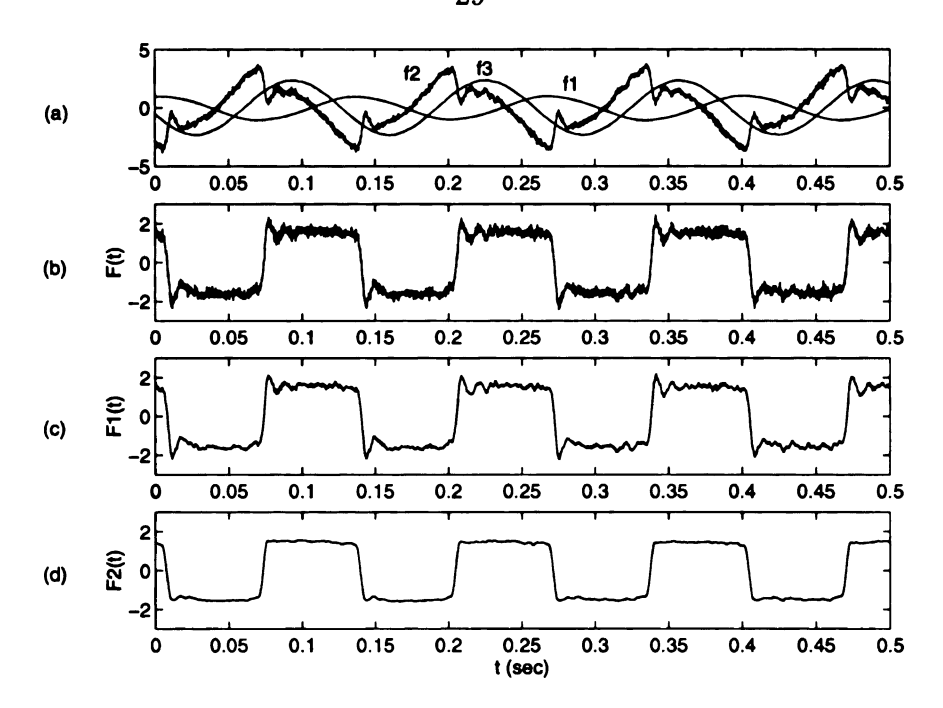


Figure 2.9: Time domain comparison of direct and indirect friction measurements, excitation frequency = 7.5 Hz, stable pure sliding case, in (a) f1: the experimental spring force= $kS_1(t)$; f2: the experimental inertial force= $mS_2(t+\tau)$; f3: the experimental excitation force= $kS_3(t)$; (b) F(t) is the calculated friction force; (c) F1(t) is the averaged version of F(t); (d) F2(t) represents the load cell measurement after averaging.

frequency of harmonic excitation is 3.5 Hz. The response of the slider is a stable puresliding motion. It is followed by Figure 2.7(b) in which the calculated friction force is presented and denoted as F(t). Random noise caused mostly by the air track was superimposed on the calculated friction signal. To reduce this effect, a smoothening algorithm (five-point moving average) was applied to this signal to generate the data shown in Figure 2.7(c) and denoted as F1(t). Next, the friction force obtained from the direct measurements of the load cell after the same smoothening process (for comparison) is illustrated in Figure 2.7(d) as F2(t). The signal F2(t) is obtained by subtracting the inertial component on the load cell due to the mass of the flange from the readout of the load cell. Moreover, the raw version of F2(t) is very much

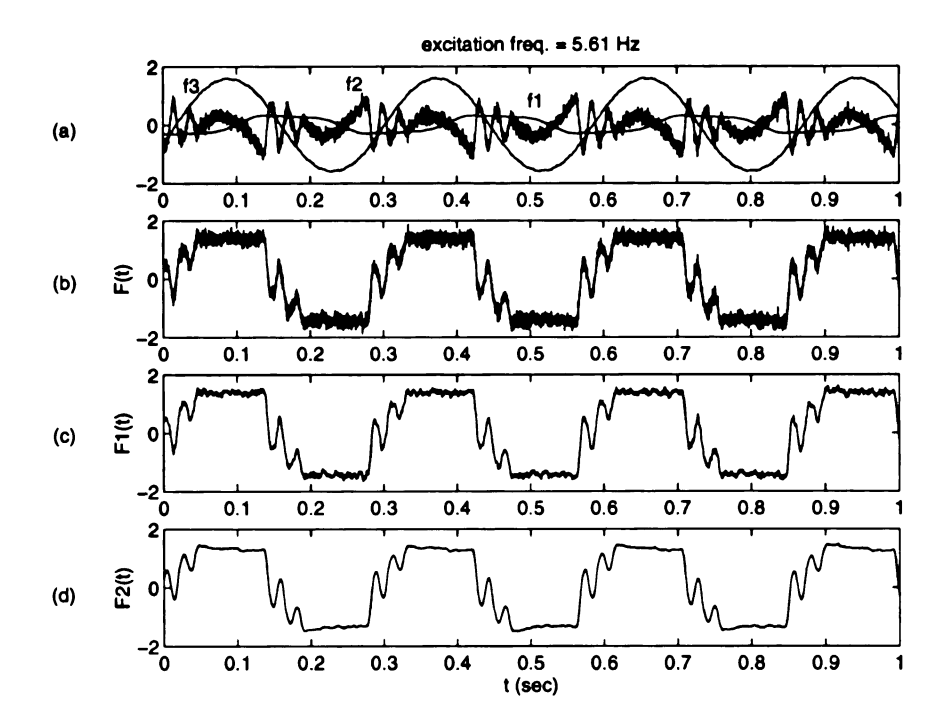


Figure 2.10: Time domain comparison of direct and indirect friction measurements, excitation frequency = 3.5 Hz, stick-slip motion case, in (a) f1: the experimental spring force= $kS_1(t)$; f2: the experimental inertial force= $mS_2(t+\tau)$; f3: the experimental excitation force= $kS_3(t)$; (b) F(t) is the calculated friction force; (c) F1(t) is the averaged version of F(t); (d) F2(t) represents the load cell measurement after averaging.

the same as the averaged version since it does not register much transient dynamics as in the computation case.

Three observations are made from Figures 2.7(b), (c), and (d). (1) During the whole test, the friction-force magnitudes are more-or-less constant. (2) Both methods are consistent regarding the macroscopic dynamics friction feature. (3) There are subtle difference between two approaches which occur at the onset of a change in sliding direction. Regarding observation (3), we note that more dynamics, especially, high-frequency dynamical response, are registered in the calculated friction force than in the directly measurement friction force. This observation agrees with our

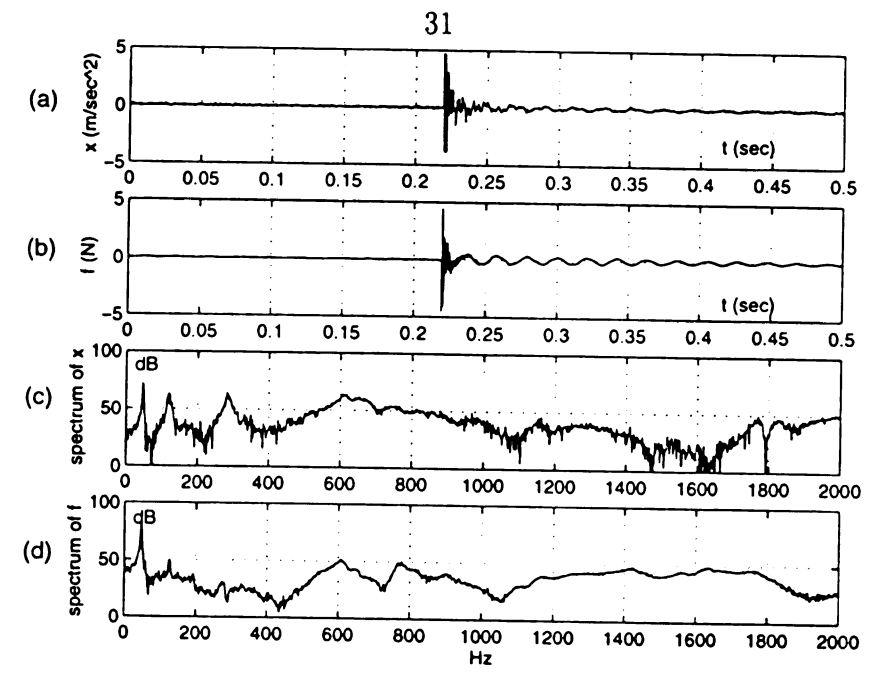


Figure 2.11: Results of impact test: (a) acceleration response; (b) friction force response; (c) power spectrum of acceleration response; (d) power spectrum of friction response.

prediction that the load cell, acting as a low-pass filter, will attenuate high-frequency signal. Furthermore, some high-frequency oscillation is evident in the calculated friction signal immediately following a velocity reversal. In order to explain this phenomenon, more insight associated with sensor dynamics is required. A detail discussion of this issue is included in the next section.

Similar to above case, two other stable pure-sliding cases are shown in Figure 2.8 and Figure 2.9 in which the excitation frequencies are 5.5 and 7.5 Hz respectively. Consistencies and discrepancies between the two approaches are preserved in these tests. Since the same phase relationship was employed between the sensors at each excitation frequency, the consistent results indeed illustrate the reliability of the indirect approach over a reasonable frequency range.

Next, we illustrate a case that has stick-slip motion, shown in Figure 2.10. The excitation frequency is 3.5 Hz. Due to the presence of stick-slip, features of the

friction force are different, especially during the transition of sliding to sticking. A high-frequency transition oscillation caused by the coupling effect between frictional contact and main system appears. A more complete discussion of this transition oscillation is included in Chapter 4.

2.5 Sensor Dynamics

This section investigates subsystem and coupling dynamics that could occur during the transition of stick-slip process or at the turning points of a pure-sliding motion. An abrupt force change usually occurs at the onset of the sticking phase in the stick-slip process and at the onset of the directional reversal in the pure-sliding motion. Such an abrupt force change can excite different subsystem dynamics or coupling dynamics.

In order to understand the possible subsystem and coupling dynamics, we first conducted an impact test on the experimental system with the friction contact engaged. In this test, the base was constrained and the impact excitation was given at the slider end. The responses were sensed by both the accelerometer and the load cell. Time-domain and frequency-domain responses corresponding to this test are illustrated in Figure 2.11. In Figures 2.11(a) and (b), the acceleration and friction time traces are presented. Figures 2.11(c) and (d) show the power spectra of the acceleration and friction signals. A harmonic at 47 Hz is contained Figures 2.11(c) and (d). This harmonic corresponds to the frequency of the transition oscillation seen in Figure 2.10. Moreover, the power spectrum of the acceleration signal registers two more spikes which correspond to 125 Hz and 250 Hz respectively. Other impact

tests show that the 125 Hz harmonic corresponds to the fundamental frequency of the accelerometer with its mounting and the 250 Hz harmonic is the fundamental frequency of the load cell and its mounting.

To this end, we have investigated the frequency responses of the accelerometer and load cell subjected to an impact excitation through the slider. Recall from the previous results of pure-sliding motion, the accelerometer addressed more transient dynamics at the onset of the direction reversal. These transient signals were suspected to be induced by the dynamics of the accelerometer subsystem (including mounting) since the dominate frequency of these transient signals was on the order of 100 Hz (Figures 2.7-2.9 (c)) which is close to the fundamental frequency of the accelerometer subsystem.

2.6 Conclusions

In this study, we compared friction measurements computed from motion sensors with those obtained directly from a load cell. We measured the friction applied to a mass gliding in an air track. The air track provided an excellent environment for isolating the friction force. Phase relationships among different transducers were investigated to implement the indirect calculation of friction force from system's ODE. Upon careful calibration of the transducers, force balances were achieved in free-vibration and forced-vibration tests. Both direct and indirect friction measurements were conducted and compared when the system was exerted by dry friction. Comparisons of these techniques showed that, although load cell can register most of the friction dynamics, its high-frequency contents will be attenuated to some ex-

tent. The calculated friction addressed more complete details over the low and high frequency ranges and also captured the noise generated by the air track. Oscillations occurring in the friction signal at velocity reversals were shown to be caused by sensor/mounting dynamics.

CHAPTER 3

THE EFFECTS OF TANGENTIAL CONTACT STIFFNESS ON A HARMONICALLY FORCED OSCILLATOR: PURE SLIDING MOTION

3.1 Introduction

Chapters 3 and 4 focus on the investigations of two experimental phenomena observed in mechanical friction systems. This chapter is devoted to the investigations of hysteresis phenomenon which is also called "spring-like" sticking behavior in the literature (Canudas de Wit et al. [10]), whereas the next chapter studies the stick-slip phenomenon as well as the transition oscillations.

Experimental investigations on the spring-like phenomenon were reported by Dahl [14] and Courtney-Pratt and Eisner [13]. Both of these studies concluded that a junction, acting like a spring during a stick, induces presliding displacement before breakaway occurs.

Efforts for modeling elastic contact problems have been put forth by many researchers. Due to the fact that the displacement change in this elasto-frictional event is so small, it has been called "preliminary displacement", "micro displacement", or "presliding displacement" in the literature (Oden and Martins [54], Canudas de Wit [10], and Harnoy [26]). However, we will denote this motion as "microsticking"

so that it is consistent with our modeling details. Previous modeling works regarding this problem include Dahl [14], Canudas de Wit et al. [10], and Harnoy [26] etc. Dahl's model is equivalent to Coulomb friction model incorporated with a lag in friction force change when the direction of motion reverses. This model is therefore suitable for describing the system possessing both contact compliance and Coulomb-like slipping behaviors. Canudas de Wit et al. [10] proposed a friction model which treats the friction interface as a contact between bristles. Such a model can numerically generate "spring-like" behaviors during a stick. It can also describe Stribeck and frictional memory effects in the sliding regime. Our tangential contact model is similar to their linearized model taken with respect to the undeformed position.

Harnoy et al. [26] proposed a compliant-contact model incorporated with another hydrodynamic sliding model to study a journal bearing problem. Numerical simulations of a lubricated journal bearing system were given even though the proposed model was not limited to a specific system. Several important friction features were revealed in their simulation results including "Dahl effect" (presliding or elastic deformation motion), the hysteresis in sliding motion (frictional memory), and the effect of coupling between presliding and sliding modes (Harnoy et al. [26]). However, their results did not include quantitative verifications in a real system, nor the investigation of the sticking dynamics. In our study, details of the presliding motion and the sticking dynamics will be addressed.

3.2 A Harmonically Forced Coulomb Oscillator

A mass-spring system on a rigid surface with Coulomb friction can have sta-

ble pure-sliding and stick-slip motions when subjected to harmonic base excitation (Hundal [30], Shaw [69], Marui and Kato [44]). These motions will be denoted as "macroscopic" sliding and stick-slip motions in contrast with the "spring-like micro" motion that occurs in the elastic contact point during a stick. The study of the existence and stabilities of these macroscopic motions can be found in the literature (e.g. Den Hartog [15], Shaw [69], Hundal [30], Marui and Kato [44]). The model of this system consists of a second-order differential equation which is piecewise linear and solvable. In fact, the solution to the steady-state, pure-sliding motion contains sinusoidal terms with both the forcing frequency and the natural frequency, and a friction term with an alternating sign depending on the sliding direction (Shaw [69]). This pure-sliding motion is sometimes called continuous motion to distinguish it from the stick-slip motion that contains at least one stop per forcing cycle.

If one conducts an FFT on a macroscopic, pure-sliding displacement response with small friction, the resulting spectrum is dominated by a harmonic corresponding to the forcing frequency. Therefore, this pure-sliding motion will be approximated as a harmonic sliding input to the compliant-contact problem discussed in this chapter.

In the next section, an idealized compliant contact model is added to the harmonically forced Coulomb oscillator. Due to the compliance of the friction contact, elastic deformations (or microsticking events) will take place when sliding mass changes its direction of motion.

3.3 The Idealized Tangential Contact Model

The model investigated here concerns the compliance effect of the frictional con-

tact. A schematic diagram illustrating the forced Coulomb oscillator together with the idealized contact model is presented in Figure 3.1, where x(t) and z(t) represent the displacements of sliding mass and base excitation respectively, y(t) denotes the displacement of the hypothetical contact surface, and K_y represents the stiffness of the contact joint. Friction will be assumed to be Coulomb friction model without difference between static and kinetic friction, namely $f_s = f_k$. The mass motion, x(t), is approximated by a harmonic function. The experiment performed later in this chapter will confirm that the above approximation is reasonable in a specific compliant-contact problem.

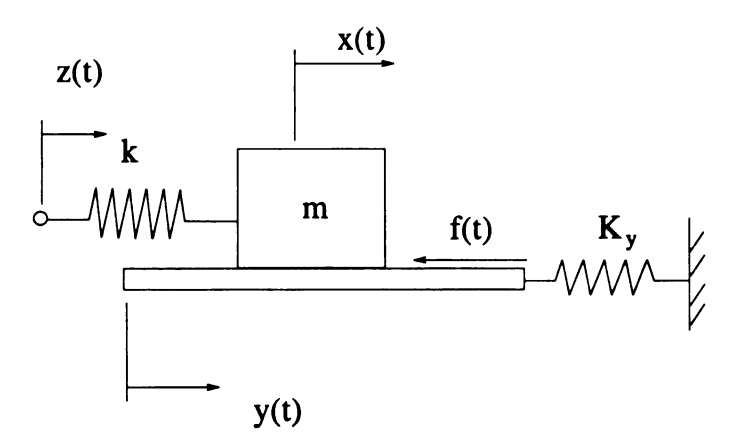


Figure 3.1: A schematic diagram showing the massless compliant contact model.

During the sliding interval, the mass moves relative to the contact surface. The contact surface is assumed to be motionless during such interval so that y(t) is a constant, i.e. $\pm Y_m \equiv \pm f_k/K_y$. There is no dynamics in y during sliding. The "microsticking" starts when the relative velocity is zero, or $\dot{x}(t) = 0$. During microsticking, both the sliding mass and the contact surface undergo the same motion, namely $\dot{x}(t) = \dot{y}(t)$. This relationship holds until the static friction force can no longer sustain the stiffness force exerted by the compliant contact joint, i.e. $|K_y y(t)| > f_k$. The

motion is called "microsticking" since when K_y is large, both the sticking interval and the elastic displacement are small.

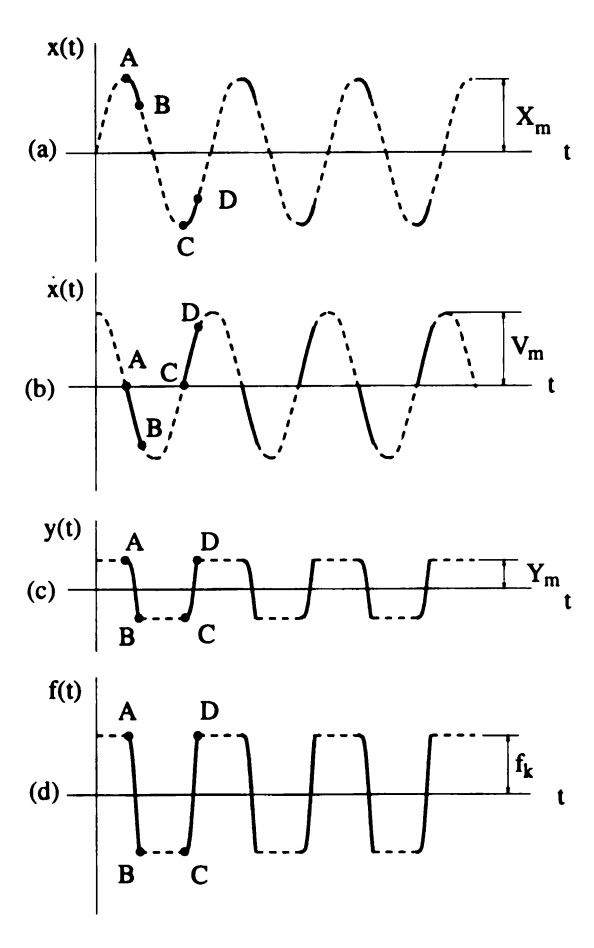


Figure 3.2: Hypothetical responses of the idealized model. Dashed lines indicate the gross sliding phase and solid lines correspond to the microsticking phase.

Hypothetical time-domain traces of $x(t), \dot{x}(t), y(t)$, and f(t) are shown in Figure 3.2, where f(t) depicts the friction force occurring at the friction interface. The dashed lines in this figure represent macroscopic sliding motion, whereas the solid lines denote the elastic deformation or the microsticking motion. According to Figure 3.2, microsticking commences at the onset of each direction reversal. Upon this microsticking, the contact joint deforms in a linearly elastic manner such that the friction force equals the spring force exerted by the effective contact stiffness. Hence,

 $f(t) = K_y y(t)$. The schematic representations of x(t), y(t) and f(t) possess similar features during the microsticking interval. On the other hand, a constant kinetic friction force is assumed during the sliding interval.

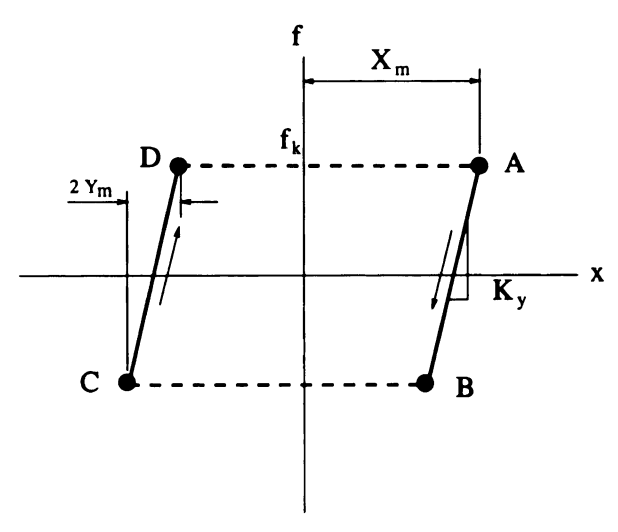


Figure 3.3: A schematic diagram showing the f-x relationship in an "ideal" compliant contact during harmonic motion of the sliding mass. Dashed and solid lines correspond to sliding and microsticking phases.

Because of the contact compliance, microsticking events replace the instantaneous jump events (which are caused by the discontinuity feature of the Coulomb law) seen during pure sliding against a rigid contact. This "microsticking" event occurs right after the mass changes its sliding direction but before sliding resumes. At the onset of sliding, the mass will have certain velocity which will be denoted as the "transition speed".

Based on the information collected from Figure 3.2(a) and (d), a qualitative f-x characteristic can be established and is illustrated in Figure 3.3. As can be seen in this plot, a constant friction force, f_k , is assumed during the sliding, while the friction force evolves in a linearly elastic way during the microsticking. The slope of the straight lines AB and CD in the f-x plot depicts the effective contact stiffness,

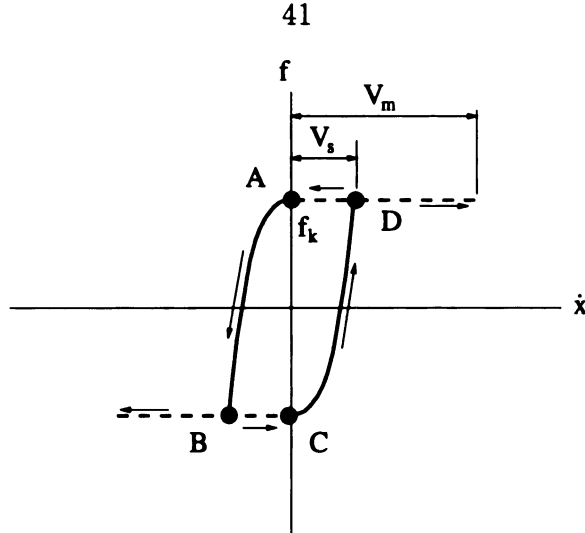


Figure 3.4: A schematic diagram showing the f- \dot{x} relationship in a compliant contact during harmonic motion of the sliding mass. Dashed and solid lines correspond to sliding and microsticking phases.

 K_y . In addition, the micro displacement in the sticking interval is twice the amplitude of the contact motion. Thus, $2Y_m = 2f_k/K_y$. The amplitude of harmonic motion of the sliding mass is X_m .

The effective stiffness of the contact joint, K_y , can be estimated from the slope of the straight lines in the f-x plot. This will be used later in the experimental study.

Next, we consider the f- \dot{x} characteristic. By manipulating features in Figure 3.2(b) and (d), a plot which dictates f- \dot{x} relationship for the harmonic sliding motion can be derived, as shown in Figure 3.4.

Figure 3.4 addresses that the maximum velocity of sliding is V_m . The "transition speed", which distinguishes microsticking and sliding, is labeled as V_s . The slanted curves AB and CD describe microsticking motion and the horizontal lines depict sliding motion. The relationship between the transition speed, V_s , the friction force level, f_k , the oscillation frequency of sliding mass, ω , and the amplitude of the oscillation, X_m , will be analyzed in the next section. Moreover, plots in Figure 3.3

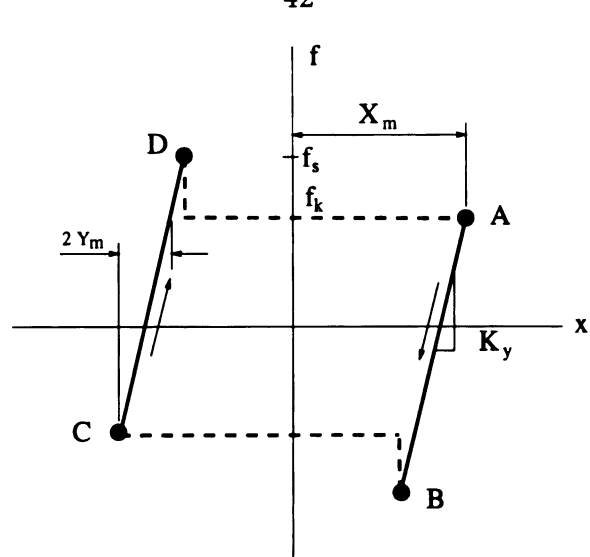


Figure 3.5: A schematic diagram showing the f-x relationship in a compliant contact during harmonic motion of the sliding mass, for $f_s > f_k$. Dashed and solid lines correspond to sliding and microsticking phases.

and Figure 3.4 are for the case in which there is no difference between the static and kinetic friction forces. The effect of $f_s > f_k$ is taken into account in the f-x and f- \dot{x} plots shown in Figure 3.5 and Figure 3.6. A jump occurs at each onset of sliding due to the transition from f_s to f_k .

An example which includes the Stribeck effects is shown in Figure 3.7(a), in which v_r represents the relative velocity at the sliding interface. Over the low velocity range, this friction characteristic has a negative slope, which usually induces instability in a friction system. This friction characteristic has been experimentally observed in many frictional systems including dry friction and boundary-lubricated systems (Bell and Burdenkin [7], Hess and Soom [28]). If we substitute this relationship into the compliant-contact model, the resulting $f - \dot{x}$ and f - x plots can be obtained as in Figure 3.7(b) and (c).

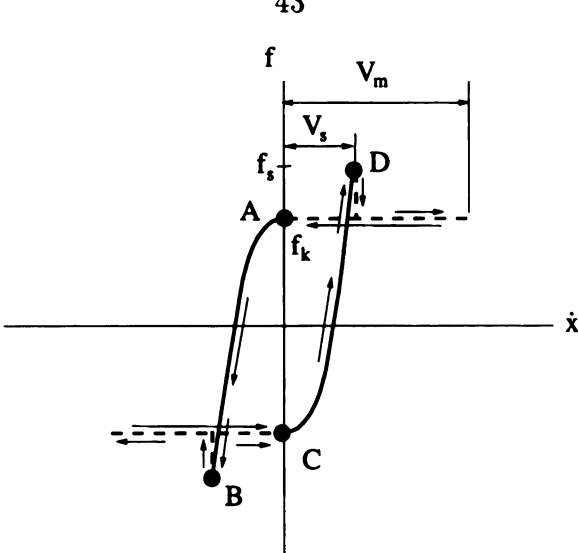


Figure 3.6: A schematic diagram showing the f- \dot{x} relationship in a compliant contact during harmonic motion of the sliding mass, for $f_s > f_k$. Dashed and solid lines correspond to sliding and microsticking phases.

3.4 Transition Features in $f-\dot{x}$ Plots

The transition speed V_s is the velocity of the mass when sliding begins. Focusing on the sticking interval in Figure 3.4, we note that the mass sticks at point "C" which corresponds to the time instant $t = t_1$, so that $\dot{x}(t_1) = 0$ and $x(t_1) = -X_m$. The contact then starts to deform elastically until sliding initiates at point "D" corresponding to $t = t_2$ (at which the transition speed is defined). Nearly harmonic motion will be assumed to be preserved during this deformation process. Thus, for $t > t_1$, the following equation is assumed:

$$x(t) = -X_m \cos \omega (t - t_1). \tag{3.1}$$

Next, we consider the conditions that are required at the point "D". The increment in displacement of the sliding mass during the interval CD is $2f_k/K_y$. Thus,

$$x(t_2) = -X_m + \frac{2f_k}{K_u} = -X_m \cos \omega (t_2 - t_1). \tag{3.2}$$

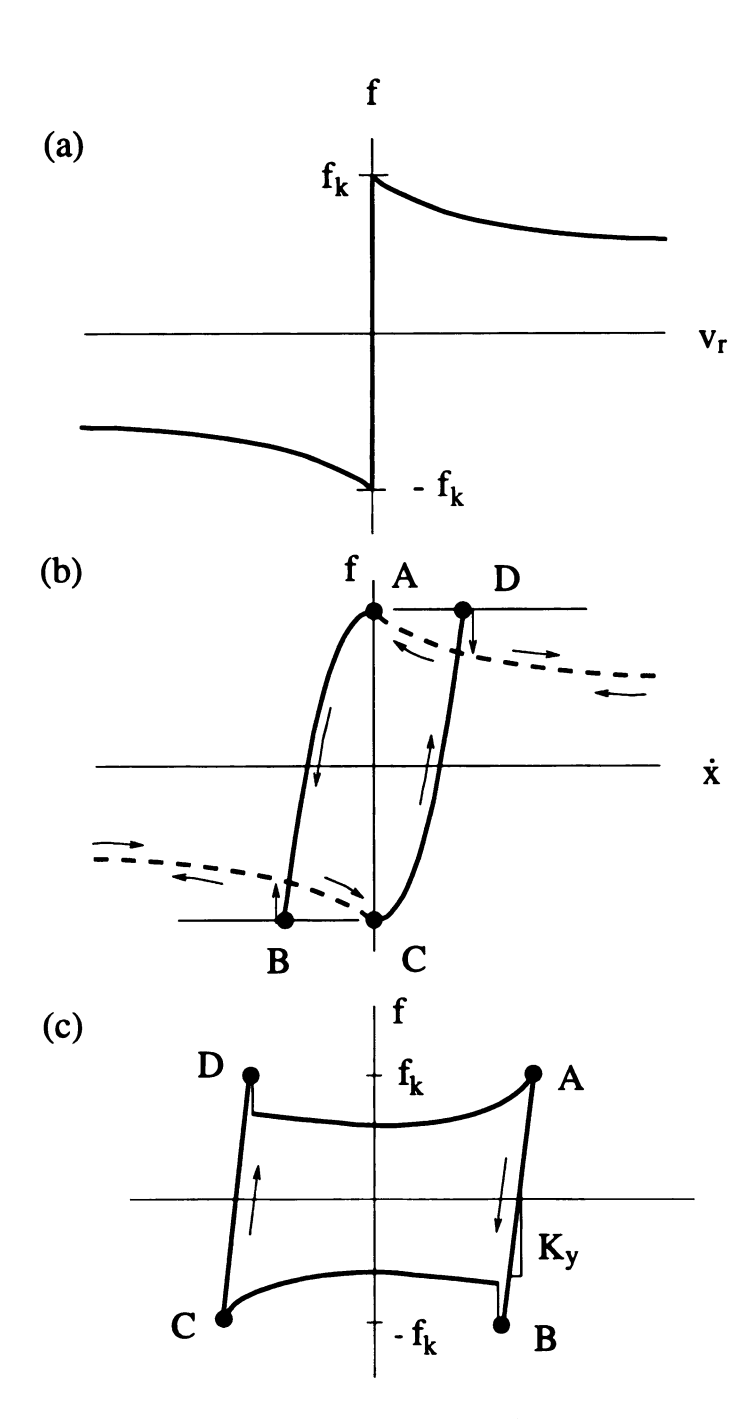


Figure 3.7: Schematic diagrams showing (a) the Stribeck friction characteristic for a rigid contact, and (b) the f- \dot{x} relationship and (c) the f-x relationship in an "ideal" compliant contact during harmonic motion of the sliding mass. Dashed and solid lines correspond to sliding and microsticking phases.

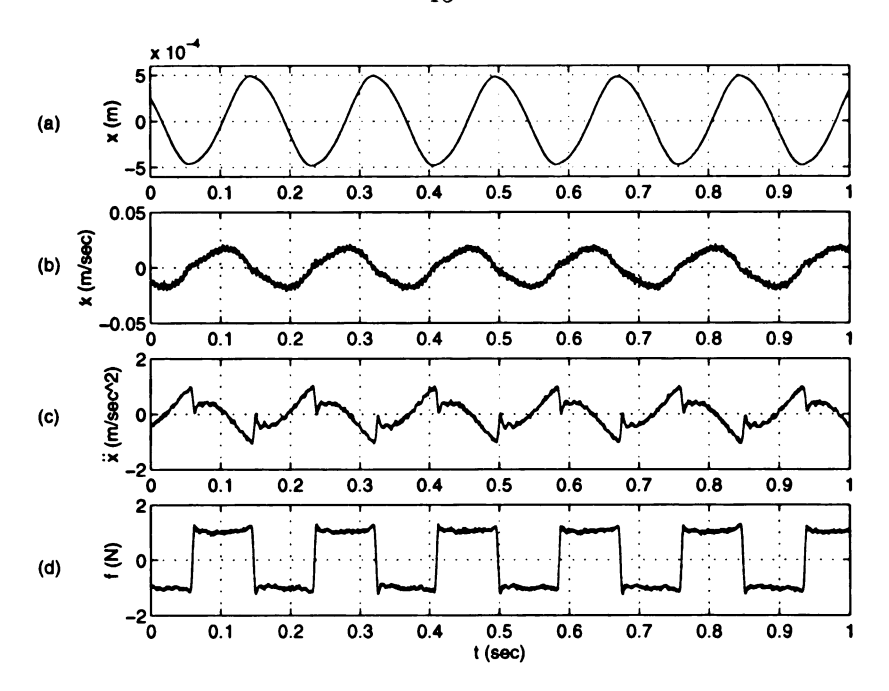


Figure 3.8: Experimental sliding motion with 5.61Hz excitation: time-domain responses of (a) displacement, (b) velocity, (c) friction force, and (d) acceleration.

Furthermore, $V_s \equiv \dot{x}(t_2)$, which is expressed as

$$V_s = \omega X_m \sin \omega (t_2 - t_1). \tag{3.3}$$

Squaring and adding " ω times equation (3.2)" and "equation(3.3)", and solving for V_s , yields

$$V_{s} = 2\omega \sqrt{\frac{X_{m}f_{k}}{K_{y}} - (\frac{f_{k}}{K_{y}})^{2}}.$$
 (3.4)

This expression shows that the transition speed is proportional to the frequency of the harmonic oscillation. Additionally, since the contact stiffness is typically large, so that the ratio f_k/K_y is small, the transition speed is approximately proportional to $\sqrt{\frac{X_m f_k}{K_y}}$. The qualitative and quantitative features of the expression (3.4) will be investigated experimentally in Section 3.5.

Another specific feature of the idealized model is the horizontal tangency of f-

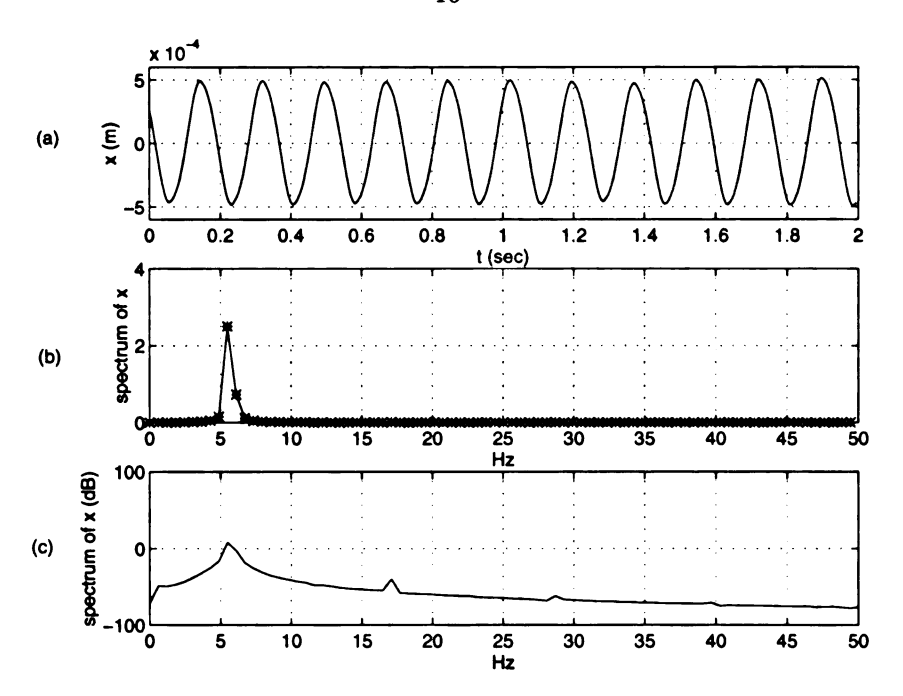


Figure 3.9: Experimental sliding motion with 5.61 Hz excitation: (a) time-domain response of displacement, (b) power spectrum of the displacement response shown in linear scale, and (c) power spectrum shown in logarithmic scale.

 \dot{x} plot in the transition from sliding to microsticking at points "C" and "A" in Figure 3.4. This characteristic is due to the fact that, during a stick, $f(t) = K_y y(t)$. More specially,

$$f(t) = K_y y(t) = K_y \{ Y_m \operatorname{sign}(\dot{x}(t_1^-)) + x - X_s \}, \tag{3.5}$$

where X_s represents the displacement of the mass when microsticking starts and t_1 corresponds to the time instant at which the mass sticks. From the above equation, we can write

$$\frac{df}{d\dot{x}} = \frac{df}{dt}\frac{dt}{d\dot{x}} = K_y \dot{x}\frac{1}{\ddot{x}}.$$
 (3.6)

Differentiating x(t) in Eq. (3.1) and substituting $\dot{x}(t)$ and $\ddot{x}(t)$ into the above equation, we have

$$\frac{df}{d\dot{x}} = \frac{K_y \dot{x}}{\omega \sqrt{X_m^2 \omega^2 - \dot{x}^2}}. (3.7)$$

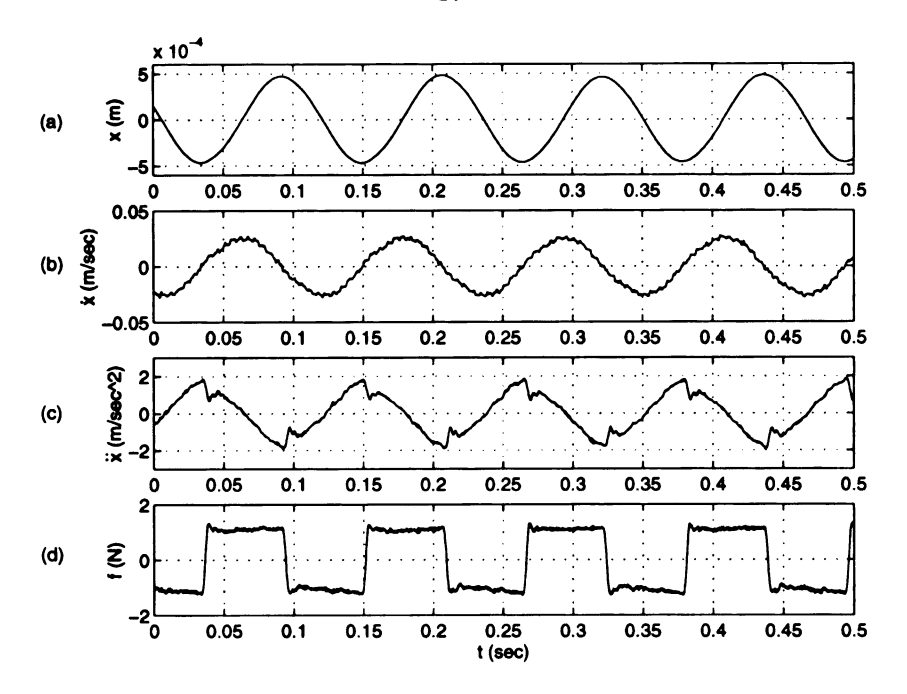


Figure 3.10: Experimental sliding motion with 8.7 Hz excitation: responses of (a) displacement, (b) velocity, (c) acceleration, and (d) friction force.

Thus, there is a horizontal tangency at the onset of microsticking, i.e. $\frac{df}{dx}\Big|_{|\dot{x}|=0^+}=0$.

3.5 Experiments in Macroscopic Sliding Motion

The experiment system was the same as the one applied in Chapter 2. The velocity signal was obtained by differentiating the displacement signal then smoothened out the resulted signal with a five-point moving average. Although we applied the smoothening algorithm to reduce the irregularity associated with differentiation process, considerable noise was still present in the smoothened velocity signal. During the whole experiment process, the nominal normal load was 3.53 N.

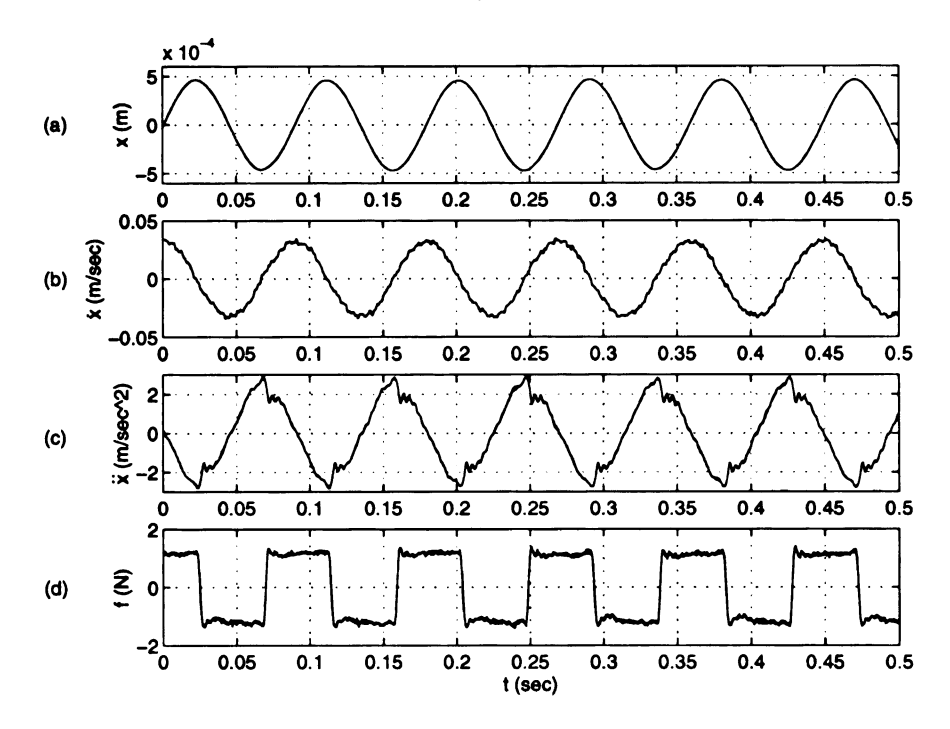


Figure 3.11: Experimental sliding motion with 11.1Hz excitation: responses of (a) displacement, (b) velocity, (c) acceleration, and (d) friction force.

3.5.1 Extraction of the Contact Stiffness

Although we neglect the modeling details of our experimental system, the system can generate both the macroscopic stick-slip and pure sliding motions.

Several experiments were carried out to validate the compliant contact model. These experiments concentrated on the macroscopic sliding motion in response to the harmonic base excitation with different frequencies. To verify that the displacement responses of these pure macroscopic sliding motions were close to harmonic functions, the power spectrum of the displacement signal of the sliding mass corresponding to 5.61 Hz excitation was examined and is presented in Figure 3.9. On a linear scale, the only harmonic present corresponds to the forcing frequency as shown in Figure 3.9(b). However, other high-order harmonics show up on a logarithmic scale (Figure 3.9(c)).

Table 3.1: Extraction of the Effective Contact Stiffness.

sliding frequency	$ ilde{K}_{m{y}}$	σ
ω (Hz)	$(\times 10^4 N/m)$	$(\times 10^4 N/m)$
5.61	20.1	2.63
8.7	18.1	2.51
11.1	19.4	2.72

The amplitude associated with the fundamental frequency is almost 100 times larger than that of the second harmonic. Therefore, it is reasonable to approximate the macroscopic sliding motion as a pure harmonic so that results in section 3.3 and 3.4 can be applied.

The first task is the extraction of the effective contact stiffness, K_y , from the experimental f-x plots. Plots from various excitation frequencies demonstrate similar microsticking characteristics; the slopes of sticking straight lines are almost indistinguishable. This implies that, during the microsticking, the contact deforms in a nearly linearly elastic manner.

Table 3.1 includes the effective contact stiffness, \tilde{K}_y , and its associated standard deviation σ .

The estimated effective contact stiffnesses are taken as the average slope of the nearly vertical portion of the f-x plots. A least-squares, linear fit was used to determine the slope. At each sliding frequency, more than 10 sliding cycles were applied to this averaging process to obtain the averaged slope and standard deviation, which are listed in Table 3.1. The overall contact stiffness, \bar{K}_y , from Table 3.1, is 192000

N/m which is taken as the mean value of \tilde{K}_y for different cases.

3.5.2 The Estimations of the Transition Speeds

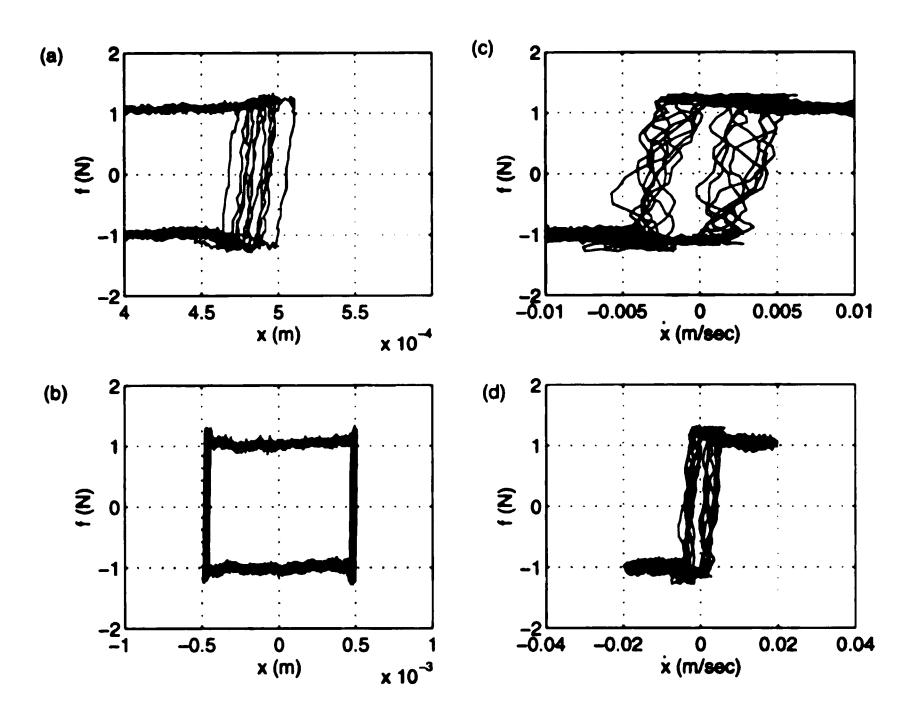


Figure 3.12: Experimental f-x and f- \dot{x} characteristics for 5.61Hz excitation: (a) detail of sticking in f-x plot, (b) f-x characteristics, (c) detail of sticking in f- \dot{x} plot, and (d) f- \dot{x} characteristics.

Given the experimental effective stiffness, we proceed in the investigations of the transition speed, V_s . Recalling from Section 3.4, the transition speed depends on the oscillation frequency, amplitude, the friction level, and the effective contact stiffness. This relationship (Eq. (3.4)) is based on the assumption of perfect harmonic sliding. The computation required in expression (3.4) calls for an estimate of the average friction level, \hat{f}_k , over the whole sliding period.

Based on the f- \dot{x} plots from each case, the parameters for the computation process in the expression (3.4) are shown in Table 3.2. In this table, the effective contact

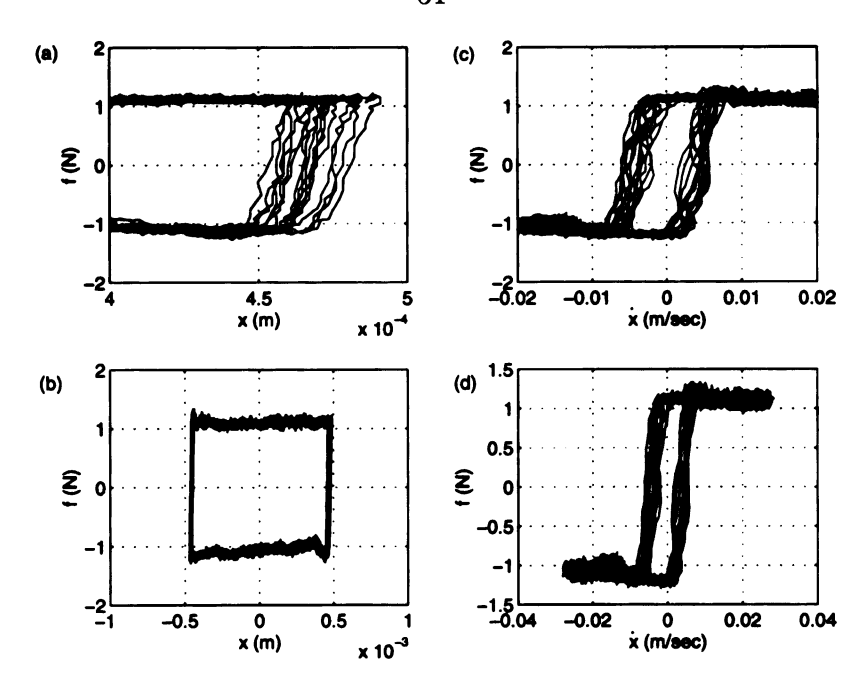


Figure 3.13: Experimental f-x and f- \dot{x} characteristics for 8.7 Hz excitation: (a) detail of sticking in f-x plot, (b) f-x characteristics, (c) detail of sticking in f- \dot{x} plot, and (d) f- \dot{x} characteristics.

stiffnesses are taken to be the same as the estimated values listed in Table 3.1. The amplitudes of sliding motion were made similar in each case for demonstration purposes. The estimates of the transition speeds, \hat{V}_s , were obtained by directly applying the estimated parameters such as ω , \hat{f}_k , \tilde{K}_y , and \tilde{X}_m , to equation (3.4). Thus, these transition speed estimates are based on analysis of the ideal model. We would like to compare these values with the experimentally observed transition speeds in Figure 3.12(c), 3.13(c), and 3.14 (c). In these figures, the band of slanted trajectories, that denote the microsticking, correspond to the curves AB and CD of the ideal model (Figure 3.4). The degree of slanting increases with the excitation frequency. This trend is consistent with the results in equation (3.4) and the simulation results in Harnoy (1994). The microstick—slip transitions (corresponding to points B and D) are approximately centered at the estimated transition speeds from Table 3.2.

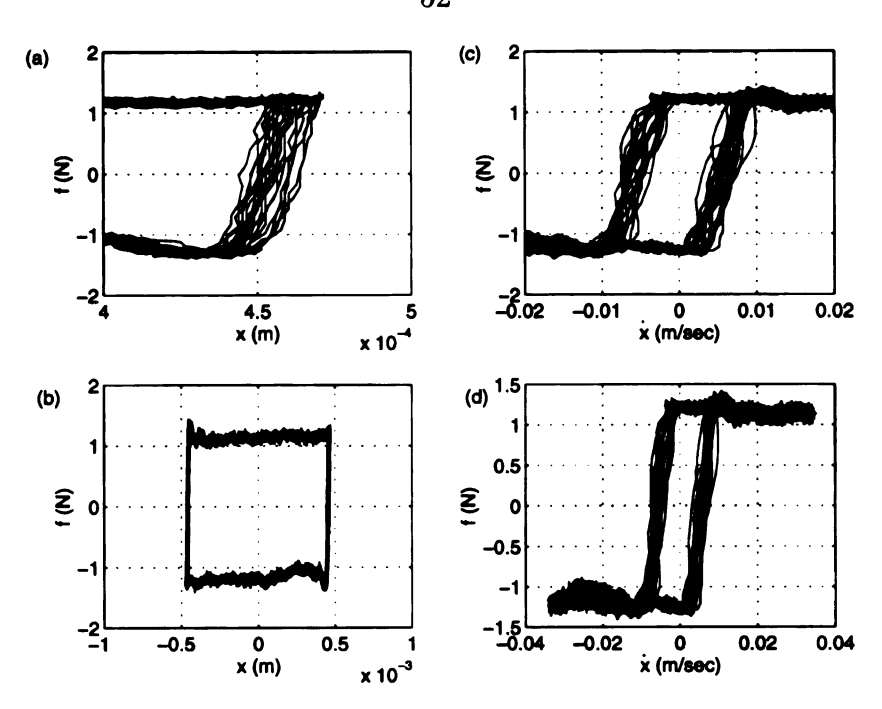


Figure 3.14: Experimental f-x and f- \dot{x} characteristics for 11.1 Hz excitation: (a) detail of sticking in f-x plot, (b) f-x characteristics, (c) detail of sticking in f- \dot{x} plot, and (d) f- \dot{x} characteristics.

These results are consistent in different excitation cases. The randomness surrounding these trends is likely caused by surface roughness or the differentiation noise of the velocity signal. Nevertheless, the main trends of the experimental data show some consistency with the ideal model.

In order to have a closer comparison, data in Figures 3.12(c), 3.13(c), and 3.14(c) was averaged. In each case, many forcing cycles were averaged so that a single-curve f- \dot{x} relationship was obtained. The result is presented in Figure 3.15. From this figure, transition speeds, corresponding to different sliding frequencies, were measured which were treated as the "measured transition speeds" and denoted as " \hat{V}_{sm} " (in Table 6.2). They are 0.0035 m/sec (ω =5.61 Hz), 0.0058 m/sec (ω =8.7 Hz), and 0.0080 m/sec (ω =11.1Hz). Associated with these values, standard deviations are 0.0021, 0.0018, and 0.0014 (m/sec) respectively. These measured transition speeds

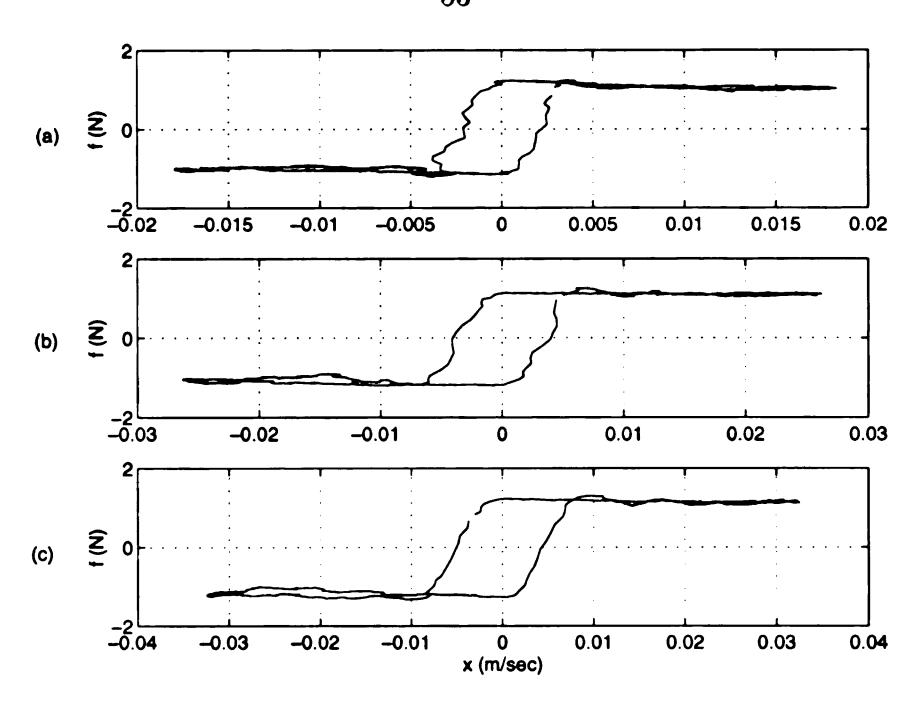


Figure 3.15: Experimental f-x and f- \dot{x} characteristics for 11.1 Hz excitation: (a) detail of sticking in f-x plot, (b) f-x characteristics, (c) detail of sticking in f- \dot{x} plot, and (d) f- \dot{x} characteristics.

are consistent with the estimations (\hat{V}_s) based on the analysis.

The tangency during the transition from sliding to microsticking is not clear in the experimental f- \dot{x} plots. Again, the randomness in the velocity signal and surface properties distorts this transition behavior.

In summary, we have shown that the ideal compliant contact model can effectively describe the experimental characteristics for the macroscopic sliding motion. In the following section, numerical studies are included to validate the contact model.

3.6 Numerical Studies

From the investigations above, we recognize that the tangential contact stiffness can induce a microsticking event. This spring-like event demonstrates itself as a slanted hysteretic structure in the f- \dot{x} plot. The following illustrates some numerical

Table 3.2: Estimation of the transition speed based on the analysis in Section 3.4

sliding freq.	\hat{f}_k	$ ilde{K}_y$	X_m	\hat{V}_s	\hat{V}_{sm}
ω (Hz)	(N)	$(\times 10^4 N/m)$	$(\times 10^{-3}m)$	(m/sec)	(m/sec)
5.61	1.06	20.1	0.49	0.0036	0.0035
8.7	1.10	18.1	0.485	0.0060	0.0058
11.1	1.28	19.4	0.48	0.0079	0.0080

investigations based on the proposed tangential contact model. The system parameters in simulations correspond to the experiment data such that the results between numerical and experimental studies can be compared.

According to the idealized tangential contact model, the system in Figure 3.1 can be represented as

$$m\ddot{x} + kx(t) + f(t) = kZ_e \cos(\omega t) \tag{3.8}$$

where Z_e is the amplitude of the harmonic base motion. Based on the modeling details in Section 3.3, $f(t) \equiv f(\dot{x}) = f_k \mathrm{sign}(\dot{x})$ in the sliding regime, and $f(t) = K_y y(t)$ during the microsticking event. The system moves from microsticking into sliding when the magnitude of $K_y y(t)$ is greater than the static friction, f_k . Furthermore, it is reasonable to incorporate damping into the contact structure. The appearance of damping will be further verified in the observations made from the experimental stick-slip signal which is presented in Chapter 4. The magnitude of the viscous damping coefficient was determined so that the simulation of stick-slip is similar to the experimental stick-slip signal. Different degrees of damping will be chosen in Chapter 4 in order to illustrate its effect on the response. However, in this section,

we will use a damping coefficient that has a nondimensional viscous damping factor equal to 0.0174. This damping effect will only be added to the contact model, i.e. $f(t) = K_y y(t) + c\dot{y}(t)$. In addition, from Section 3.3, we know that $\dot{y}(t) = \dot{x}(t)$ during the microsticking interval, thus the model becomes

• during sliding

$$m\ddot{x} + kx(t) + f_k \operatorname{sign}(\dot{x}) = kZ_e \cos(\omega t)$$
 (3.9)

during microsticking

$$m\ddot{x} + kx(t) + c\dot{x} + K_y y(t) = kZ_e \cos(\omega t)$$
(3.10)

$$y(t) = Y_m \operatorname{sign}(\dot{x}(t_1^-)) + x(t) - X_s \tag{3.11}$$

where Y_m (positive number) is the maximum deflection of the contact and X_s (number with a sign) is the displacement of the mass before microsticking begins. t_1 represents the time instant at which the mass sticks. The switching between microsticking and sliding motion occurs when the magnitude of $f(t) = K_y y(t) + c\dot{y}(t)$ is greater than f_k . Based on this model, the numerical simulations can be carried out.

System parameters in the numerical studies are tuned such that both experimental and simulated results possess same macroscopic motion features. Nevertheless, there are small discrepancies between the amplitudes of excitation, i.e. Z_e , and consequently the amplitude of response, X_m , particularly for the case of 5.61 Hz excitation frequency and the stick-slip case. These discrepancies may be due to flaws in the friction modeling or the imperfection of the excitation force provided by the electromagnetic shaker. They can also be the result of other experimental errors.

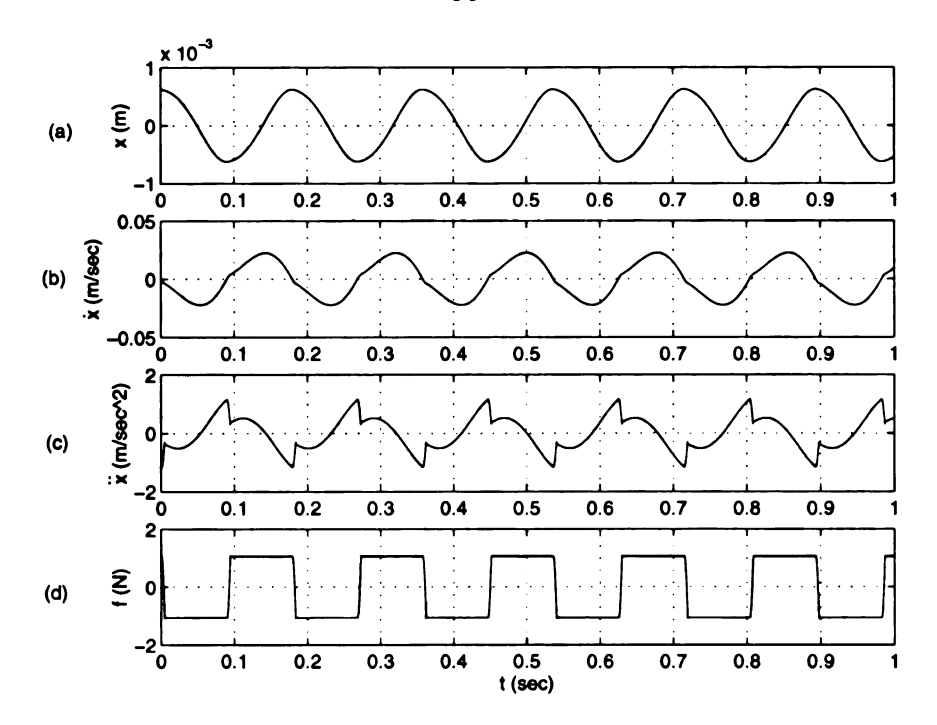


Figure 3.16: Numerical simulations of the pure sliding motion (ω =5.61 Hz) with the tangential contact model, responses of: (a) displacement, (b) velocity, (c) acceleration, and (d) friction force.

Except for the excitation amplitude Z_e , parameters such as K_y, m, k, f_k are the same as those estimated from experimental studies. Table 3.3 shows the excitation amplitudes of different cases in both experimental and numerical studies. It also contains the parameter values for the simulations of stick-slip process and the state-variable friction model that will be addressed later in Chapter 4.

Shown in Figures 3.16-3.18 are the time-domain simulated responses for different excitation frequencies. These plots correspond to the experimental results illustrated in Figures 3.8, 3.10 and 3.11. The simulated results are very consistent with the experimental results. The consistencies exist not only in the macroscopic motion features but also in the response magnitudes. In Figures 3.19-3.21, the slanted hysteretic structure is seen in the numerical versions of f- \dot{x} plots. These figures can be

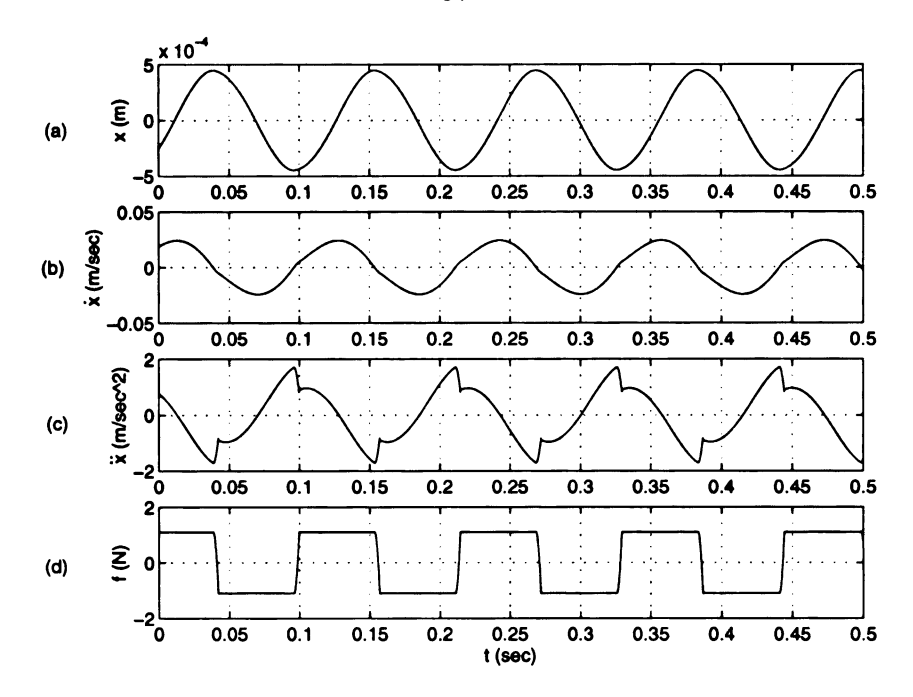


Figure 3.17: Numerical simulations of the pure sliding motion (ω =8.7 Hz) with the tangential contact model, responses of: (a) displacement, (b) velocity, (c) acceleration, and (d) friction force.

compared to Figures 3.12-3.14. Because the idealized model does not account for the randomness of the surface roughness as well as the differentiation noise of velocity signal, the slanted structure appears as a single curve instead of banded structure as in the experimental f- \dot{x} plots. Nevertheless, the slanted structure in numerical studies matches experimental results closely, particularly in the trend of frequency dependence of the transition speed, V_s . Furthermore, the magnitude of V_s agrees with the prediction given in the expression (3.4) very well. There may be a small deviation caused by the presence of viscous damping which was absent in the derivations of expression (3.4). Since V_s is defined as the velocity at which $K_y y(t) + c\dot{y}(t) = f_k$, the presence of viscous damping will affect the evolution of y(t), and consequently, V_s . Moreover, the horizontal tangency exists in the numerical versions of the f- \dot{x} plots during the transition from sliding to microsticking.

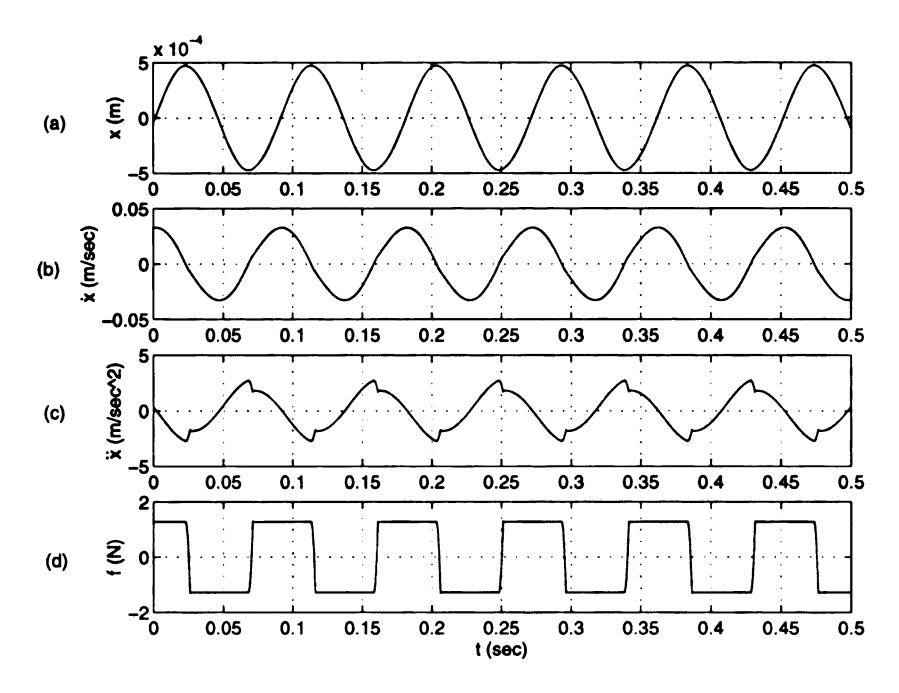


Figure 3.18: Numerical simulations of the pure sliding motion ($\omega=11.1$ Hz) with the tangential contact model, responses of: (a) displacement, (b) velocity, (c) acceleration, and (d) friction force.

According to the above observations, the tangential contact model can indeed describe the experimental system qualitatively and quantitatively well when the motion is a macroscopic pure sliding. In the next section conclusions regarding the study on the pure sliding motion are given.

3.7 Summary

An idealized tangential contact model was used to interpret the hysteretic behavior in the f- \dot{x} measurements. A geometric analysis led to the qualitative and quantitative elasto-frictional characteristics in the f-x and f- \dot{x} plots. These characteristics include a transition speed between microsticking and sliding motion and a method for estimating the effective tangential contact stiffness.

Table 3.3: Amplitudes of harmonic base excitation (Z_{e1} and Z_{e2} representing the simulation values of the tangential contact model and the state-variable model, whereas \hat{Z}_{e} denoting the experimental values)

sliding freq.	Z_{e1}	Z_{e2}	\hat{Z}_e
$\omega(\mathrm{Hz})$	$(\times 10^{-3}m)$	$(\times 10^{-3}m)$	$(\times 10^{-3}m)$
2.5 (stick-slip motion)	0.65	0.6	0.6
5.61 (pure sliding motion)	0.6	0.6	0.51
8.7 (pure sliding motion)	1.1	1.1	1.1
11.1 (pure sliding motion)	2.0	*	2.0

Experimental studies were carried out to demonstrate that this idealized model can reasonably describe elasto-frictional behaviors in a real system. Consistencies between the analytical predictions and experimental observations of the microsticking characteristics were illustrated through macroscopic sliding experiments. Numerical simulations of the tangential contact model reproduced the hysteresis in the f- \dot{x} plot. Qualitative and quantitative consistencies were shown between numerical and experimental results.

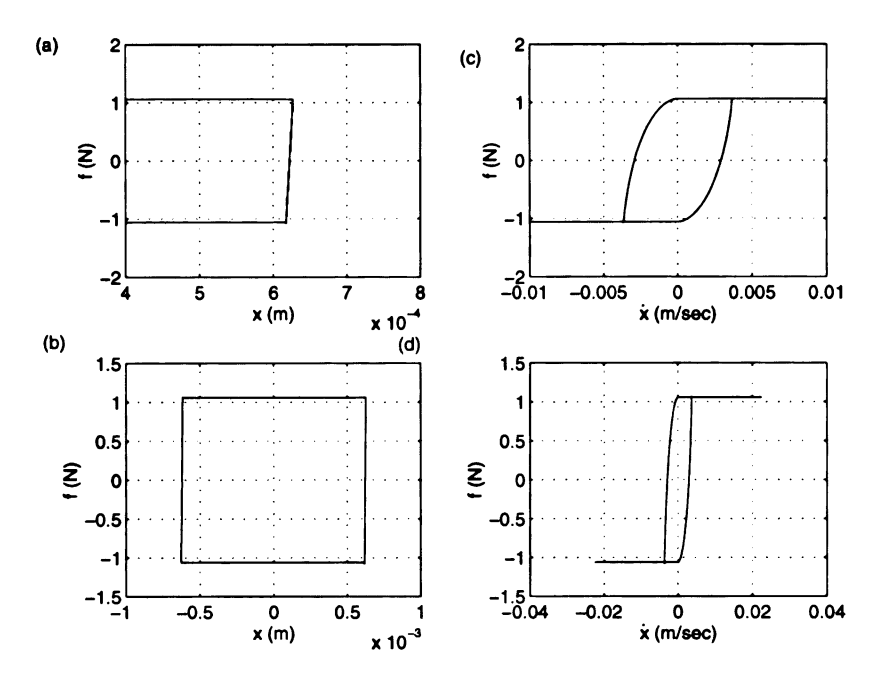


Figure 3.19: Simulation of tangential contact model (ω =5.61 Hz), numerical versions of: (a) zoom-in detail of sticking in f-x characteristic, (b) f-x plot, (c) zoom-in detail of sticking in f- \dot{x} plot, and (d) f- \dot{x} characteristic.

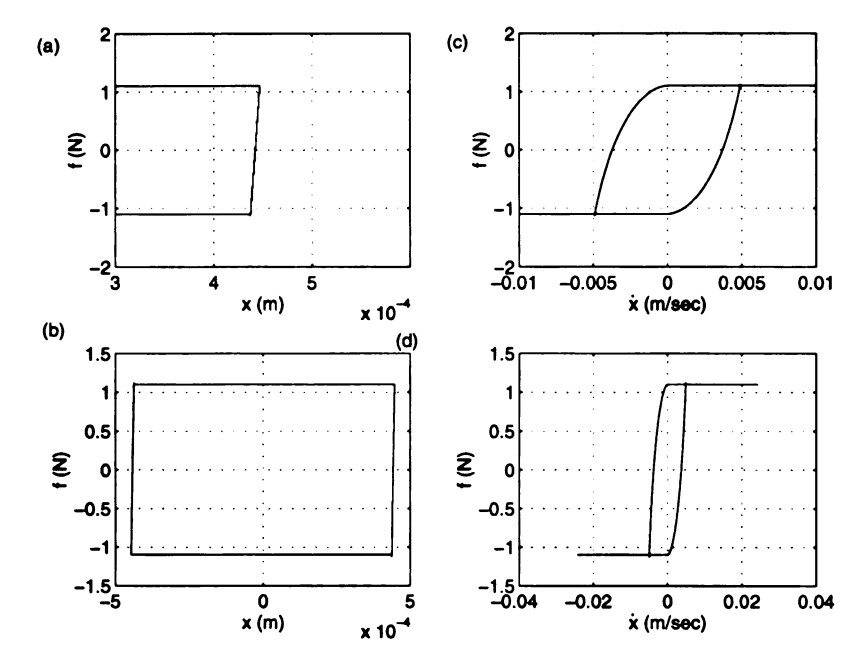


Figure 3.20: Simulation of tangential contact model (ω =8.7 Hz), numerical versions of: (a) zoom-in detail of sticking in f-x characteristic, (b) f-x plot, (c) zoom-in detail of sticking in f- \dot{x} plot, and (d) f- \dot{x} characteristic.

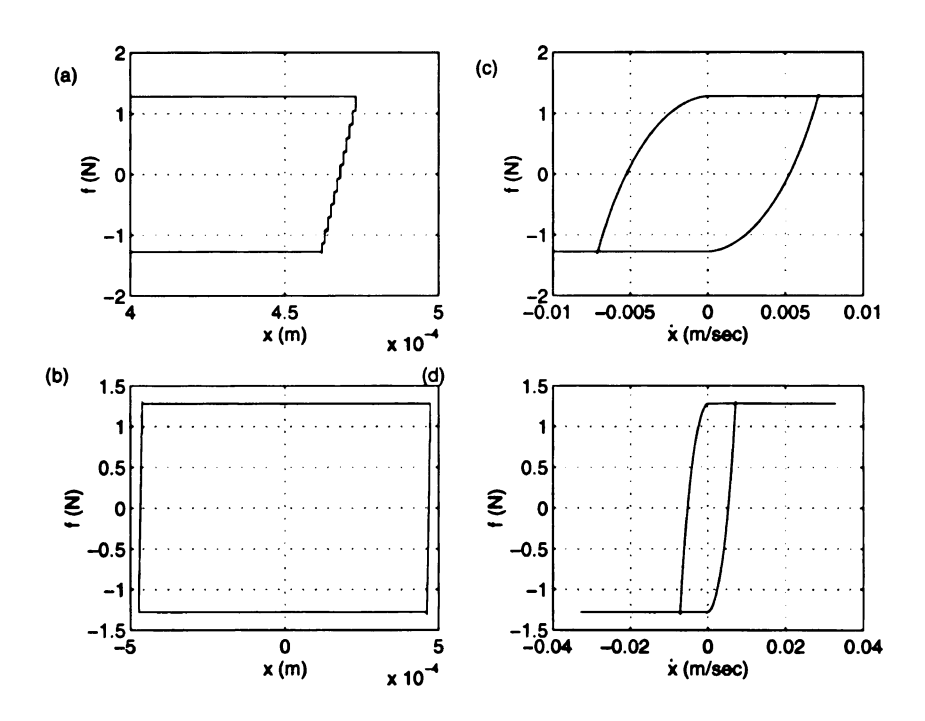


Figure 3.21: Simulation of tangential contact model (ω =11.1 Hz), numerical versions of: (a) zoom-in detail of sticking in f-x characteristic, (b) f-x plot, (c) zoom-in detail of sticking in f- \dot{x} plot, and (d) f- \dot{x} characteristic.

CHAPTER 4

THE EFFECTS OF TANGENTIAL CONTACT STIFFNESS ON A HARMONICALLY FORCED OSCILLATOR: STICK-SLIP MOTION

4.1 Introduction

This chapter gives detailed investigations of the transition oscillation. Although there has been considerable progress in the study of the dynamical friction problems, detailed discussion of the transition oscillations in a stick-slip process has not been offered. During the transition from slip to stick, oscillations have often been observed (Marui and Kato [44], Polycarpou and Soom [56], Ko and Brockley [38], Rorrer [65]). These transition oscillations are believed to result from the coupling between the contact subsystems and main system. Here, the contact subsystem refers to the contact point as well as the surrounding structure. The main system, in contrast, consists of a mass-spring system with known parameters. Polycarpou and Soom [56] investigated a boundary lubricated system. The transition oscillations occurred in their friction force and acceleration signals and were interpreted as the natural response of the combined system which was composed of rider subsystem and rotating disk. Ko and Brockley [38] focused on dry friction measurements in a pin-on-disk apparatus. The velocity signal during a unidirectional stick-slip motion possessed a similar transition. According to their investigation, this oscillation

was caused by the coupling between disk and pin dynamics. More recently, Rorrer [65] used multi-DOF systems to model the high-frequency transition oscillations observed experimentally in a specific system. By matching up frequency-domain information between the simulated and measured friction responses, the appropriate system order was determined and the transition oscillation was observed in the simulated responses. Nevertheless, these studies, concentrating on the unidirectional pin-on-disk problems, did not include detailed discussions of how system coupling effects relate to the transition oscillations.

In this study, we show that the averaged tangential contact stiffness, \bar{K}_y , estimated in Chapter 3, when coupled with the main system parameters, can produce the high-frequency transition oscillations. The frequency content of the transition oscillation is first experimentally observed. This observed frequency is found to be similar to the one predicted using the characteristic of the idealized tangential contact model and the average contact stiffness \bar{K}_y . In the numerical simulations of the tangential contact model, a "microscale" stick-slip event was shown to occur during the transition of the numerical stick-slip process. The friction-force response confirms this event in the experiment system. This phenomenon is termed "microscale" stick-slip since many short-period slipping events take place during a high-frequency sticking oscillation. As a result, the response contains two different scales of stickslip, i.e. macroscopic and microscale stick-slip. Therefore, this process will be called a double stick-slip event. The presence of microscale stick-slip event during a macroscopic sticking interval indicates that the transition oscillation can be more general than a purely harmonic oscillation.

The organization of this chapter is as follows. An experimental stick-slip process is presented in the next section so are the results of a free-vibration test. The frequency contents of the transition oscillation is explored in this section. Section 4.3 describes the numerical studies of stick-slip phenomenon focusing on the tangential contact model. During the investigations, a double stick-slip event is revealed. The frictionforce response confirms this event in the experiment system. The mechanism of this event is also discussed. In Section 4.4, we focus on the numerical studies of the statevariable friction model. Over some parameter ranges, the state-variable model can depict the transition oscillation during a stick-slip process. Examined cases including macroscopic stick-slip and pure-sliding motions. Features in both the time-domain responses and the f-x and f- \dot{x} plots are compared to those of the experimental results and the simulations of tangential contact model. Section 4.5 investigates a compliant contact model which includes the effect of inertia. Under the harmonically imposed motion, this model demonstrates microscale stick-slip motion. Numerical simulations are conducted in order to show features of microscale stick-slip in both time-domain histories and phase portraits. Section 4.6 summarizes the study of the transition oscillation and double scale stick-slip motion. It also gives a brief conclusion of the investigations in Chapters 3 and 4.

4.2 The Transition Oscillations in a Experimental Stick-Slip Process

As mentioned in Section 4.1, many previous works have reported the occurrence of high-frequency oscillations in experimental acceleration and friction signals. To demonstrate this phenomenon, we conducted an experiment with a macroscopic

stick-slip process as shown in Figure 4.1. The experimental setup was the same as that used in Chapter 3. The frequency of the base-excitation motion in this test was 2.5 Hz.

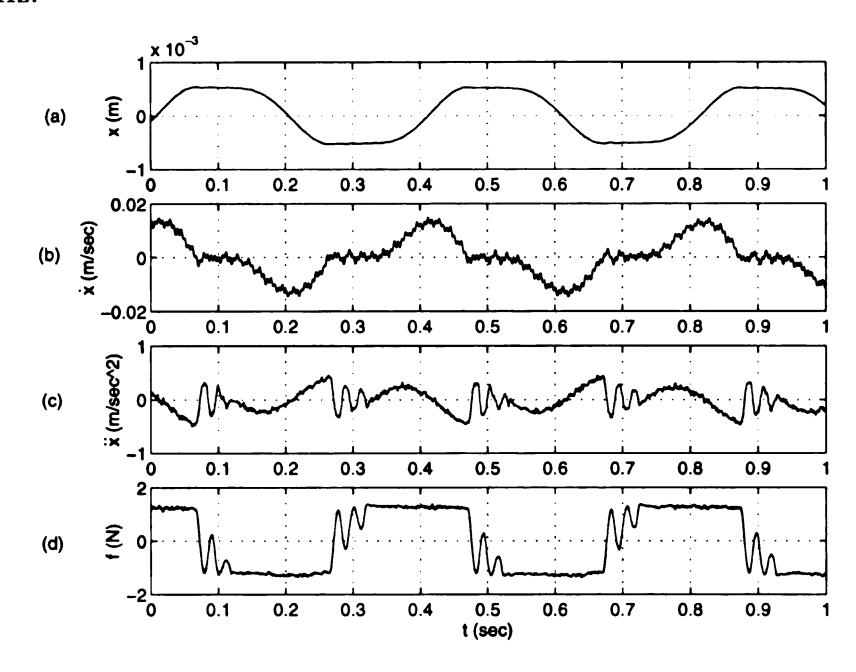


Figure 4.1: Experimental stick-slip motion with 2.5 Hz excitation: time-domain responses of (a) displacement, (b) velocity, (c) acceleration, and (d) friction force.

In Figure 4.1, transition oscillations are evident in the acceleration and friction signals. Small amplitude ripples also occurred during the macroscopic sticking interval of the velocity and displacement time histories, although they can barely be seen. In this investigation, the frequency of the transition oscillation is studied first. To examine the frequency of the transition oscillation, a free-vibration test was carried out on the mass when stuck to the friction contact (Figure 4.2). This experiment was performed by releasing the sliding mass from an initial position. The presence of dry friction stopped the mass after some motion.

Figure 4.2(a) demonstrates the friction force trace in response to the initial dis-

.

(

to

ce]e

Enry

the qu

10

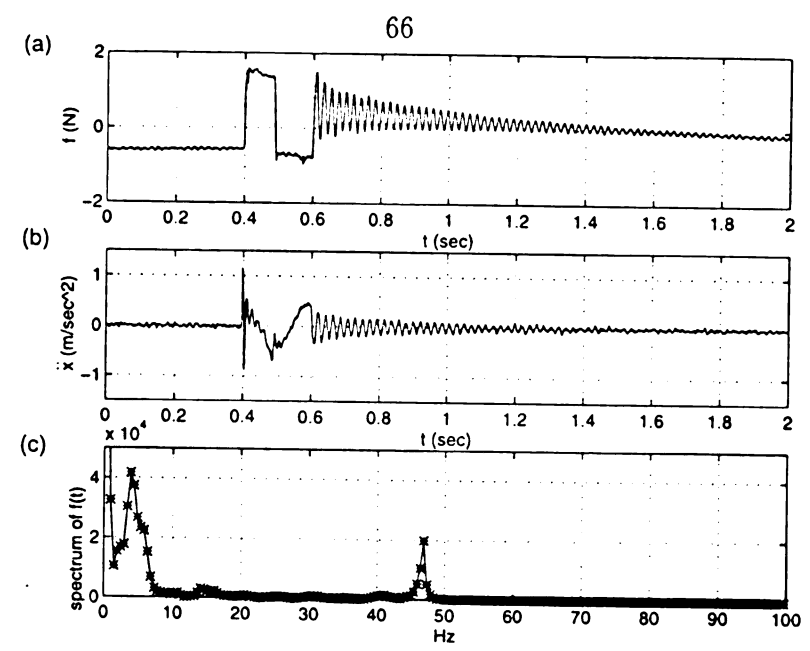


Figure 4.2: Results of free-vibration test: (a) friction force time-domain response, (b) acceleration time-domain response, and (c) power spectrum of friction force signal.

placement. In this case, the motion of the sliding mass changed its direction twice before it stuck. Moreover, at the onset of sticking, a high-frequency oscillation occurred. Due to the discharge characteristic associated with the load cell, the DC level of the friction signal slowly drifted. A similar transition oscillation occurred in the acceleration signal which is presented in Figure 4.2(b). In order to get rid of air noise, the acceleration signal has been smoothened by the moving-average algorithm. An FFT of the friction signal is illustrated in Figure 4.2(c). The frequency of this transition oscillation is 47.0 Hz. The low-frequency components correspond to the nonperiodic transients of the friction signal. Both the friction force and acceleration signals contain the same frequency content in the transition oscillations. Furthermore, frequency estimations can also be accomplished by directly measuring the periods of oscillations in the acceleration/friction signals shown in Figure 4.1(c) and (d). These frequency estimations are consistent with the results from the FFT.

,

F.

 ρ_{oth}

trâ

ēρ^{OΛ}

12/

Thus, we have experimentally evaluated the frequency of the transition oscillation. In order to investigate the relationship between this oscillation frequency with the coupling effects, the main system parameters are required. These parameters are $m=2.42~{\rm kg}$ and $k=2310~{\rm N/m}$. According to the sticking condition and the structure of the experimental apparatus, during sticking, the sliding mass is supported by the spring of the main system and an equivalent spring provided by the contact point. Therefore, a simple model for calculating the fundamental frequency during a stick will be a one-DOF system connected to two springs. Based on the averaged contact stiffness, \bar{K}_y , which has been determined to be 192000 N/m in Section 3.5, and main system parameters, the coupled fundamental frequency is equal to 45.1 Hz. This value is very close to the result from the free-vibration test. It seems that the transition oscillation is a high-frequency, nearly harmonic oscillation. Nevertheless, the numerical simulations carried out in the next section dictate that more dynamics can take place during a macroscopic sticking interval.

Next, we explore the f-x and f- \dot{x} characteristics associated with the macroscopic stick-slip process. The key point is to check whether the features in these plots, with the stick-slip event, are consistent with those in the macroscopic sliding cases. The f-x and f- \dot{x} characteristics of experimental stick-slip process are illustrated in Figure 4.3. It is evident that sticking features are different. The occurance of the transition oscillation gives rise to the tangle structures during the sticking regions in both f-x and f- \dot{x} plots. A more careful observation in the f-x plot (Figure 4.3(a)) shows that friction actually fluctuates before it moves from one extreme value to the other. This is again caused by the transition oscillation. Thus, the transition

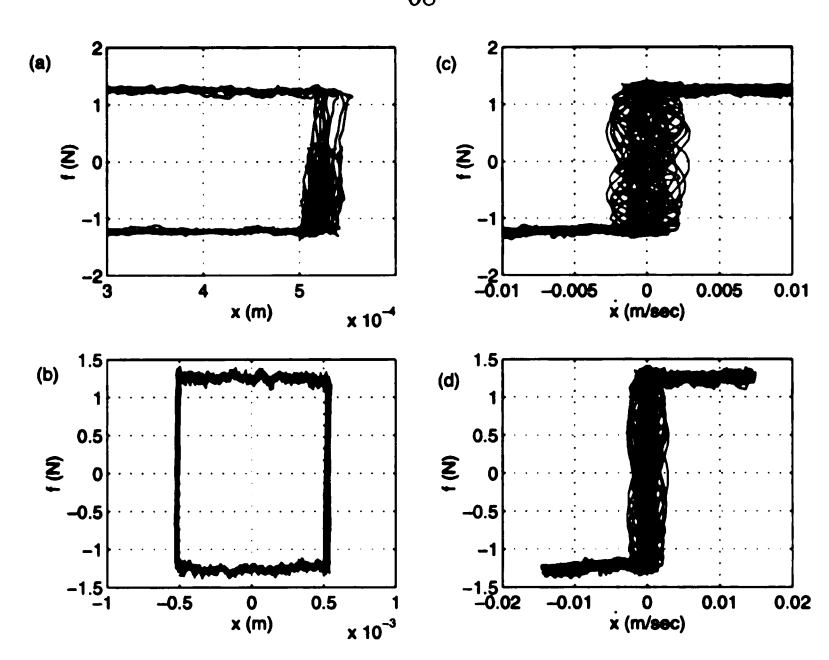


Figure 4.3: Experimental f-x and f- \dot{x} characteristics with stick-slip process: (a) zoom-in detail of sticking in f-x plot (b) f-x characteristics (c) zoom-in detail of sticking in f- \dot{x} plot (d) f- \dot{x} characteristics.

features in the f-x characteristic are different from the linearly elastic nature shown in the pure sliding case. This specific observation will be further discussed in the next section. Conversely, the randomness of surface roughness, differentiation noise of velocity signal, and tangled structure completely conceal the transition behaviors in the f- \dot{x} plot.

The following section addresses the numerical investigations of the stick-slip process. In the simulations, parameter values are chosen to match the experimentally observed stick-slip process. Friction models include the compliant tangential-contact model with different viscous damping effects. In addition to macroscopic stick-slip process, over some system parameter range, the compliant tangential-contact model can produce a microscale stick-slip process. This phenomenon possessing two different scales of stick-slip is termed a double stick-slip process.

4.3 Numerical Investigations of Stick-Slip Phenomenon

The numerical model for stick-slip simulation is the same as that addressed in Section 3.6. The excitation amplitudes input to the numerical model is listed in Table 3.3, Chapter 3. From the experimental stick-slip data shown in Figure 4.1, the appearance of viscous damping can be justified since the amplitudes of transition oscillation decay. Thus, it is reasonable to add damping to the contact model. The amount of damping added is chosen so that the simulation and experimental results are comparable.

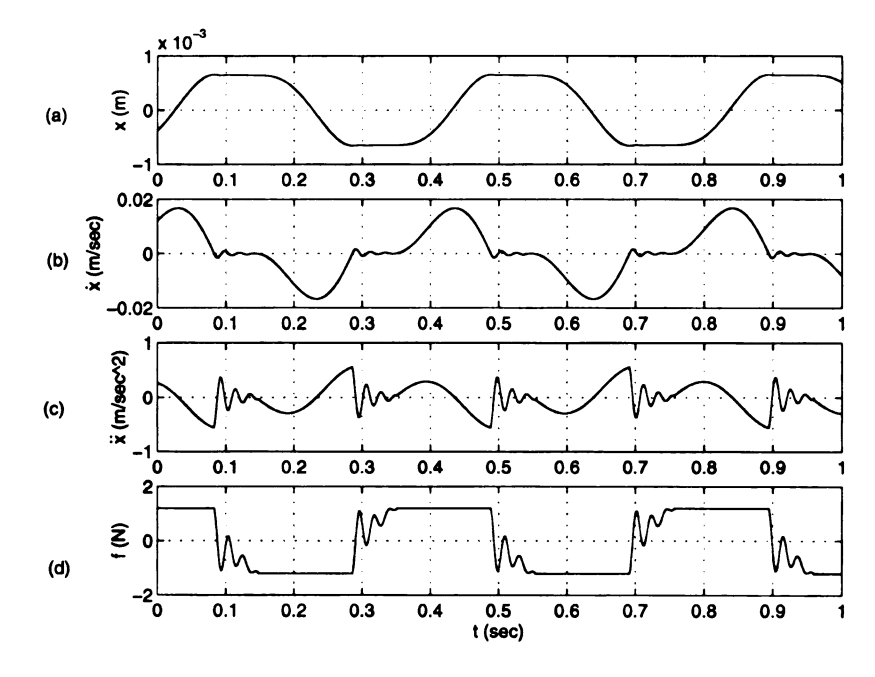


Figure 4.4: Numerical simulations of stick-slip phenomenon with tangential contact model, case 1, responses of: (a) displacement, (b) velocity, (c) acceleration, and (d) friction force.

The simulation results corresponding to a viscous-damping factor of 0.0558 are shown in Figure 4.4 and 4.5. This simulation example is denoted as case 1. Comparing these plots with the equivalent experimental results shown in Figures 4.1 and 4.3,

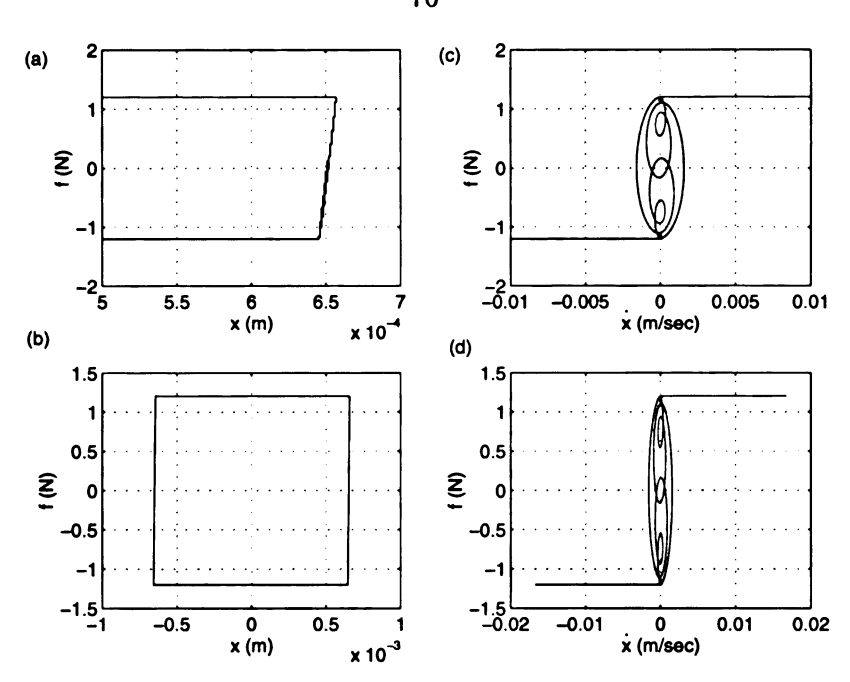


Figure 4.5: Simulation of tangential contact model, case 1, numerical versions of: (a) zoom-in detail of sticking in f-x characteristic, (b) f-x plot, (c) zoom-in detail of sticking in f- \dot{x} plot, and (d) f- \dot{x} characteristic.

the following observations can be made. (1) The numerical model seems to match the experiment system well, particularly in the macroscopic motion features of the friction and acceleration histories. For example, macroscopic stick-slip occurs with the the transition oscillation. However, a faster decaying speed appears in the simulated transition signal. This implies that a lower viscous damping is required for properly describing the contact dynamics. (2) Numerical results in the f-x characteristics depict the transition features observed in experimental data. This includes the fluctuations of friction force during the sticking interval, which can be observed in Figure 4.5(a) as a darker portion in the lower part of the transition line. On the other hand, a multiple-loop structure present in the f- \dot{x} characteristic manifests the transition oscillation. The presence of this multiple-loop structure replaces the slanted hysteretic structure occurring in the pure sliding case. This loop structure

also states the existence of the oscillation ripple in the velocity response. In the experimental case, these loops may be complicated by noise in the \dot{x} signal.

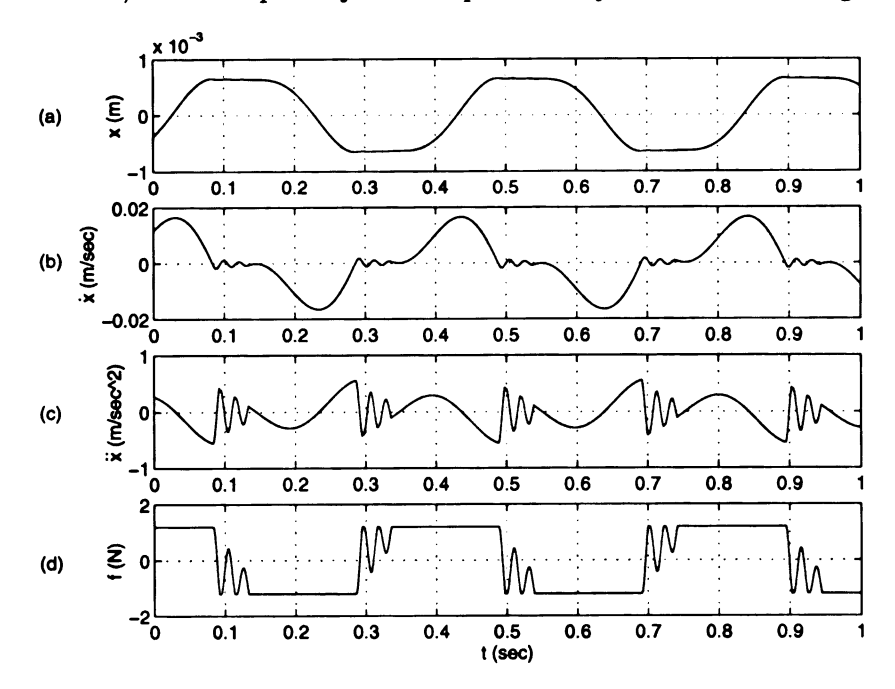


Figure 4.6: Numerical simulations of stick-slip phenomenon with tangential contact model, case 2, responses of: (a) displacement, (b) velocity, (c) acceleration, and (d) friction force.

Since the simulation of case 1 does not capture the complete transition characteristic of the experimental stick-slip process, i.e. the "double stick-slip" event, we performed another simulation with lower viscous-damping coefficient. This simulation has a damping factor equal to 0.0174 and will be referred to as case 2. The numerical simulations are shown in Figures 4.6 and 4.7. Responses in acceleration and friction force illustrated in Figure 4.6 match the experimental data very well. The amplitudes of the transition oscillation registered in the acceleration signal are especially comparable to those in Figure 4.1(c). Furthermore, the simulation demonstrates that instead of the purely decaying motion as in case 1, a microscale stick-slip occurs in this lower-damping case. This event is evident because the friction force,

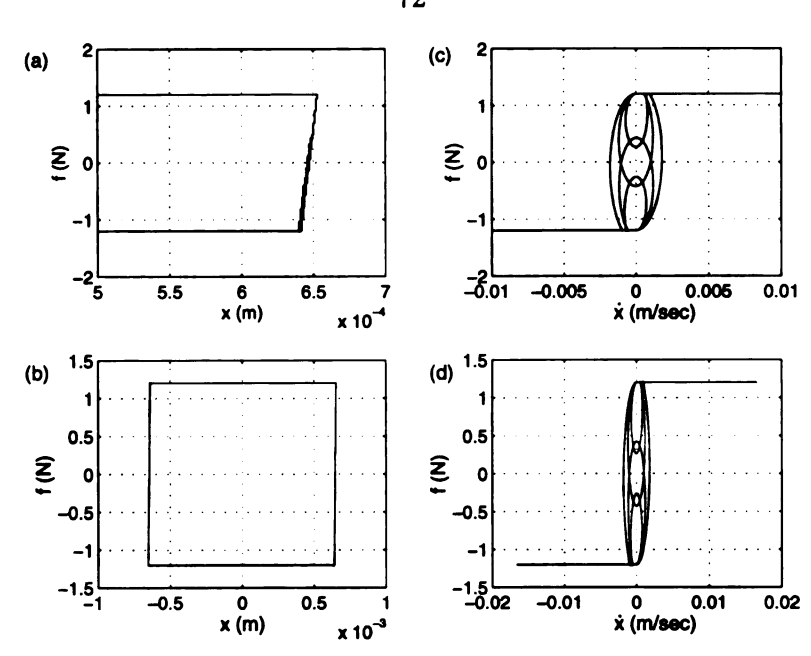


Figure 4.7: Simulation of tangential contact model, case 2, numerical versions of: (a) zoom-in detail of sticking in f-x characteristic, (b) f-x plot, (c) zoom-in detail of sticking in f- \dot{x} plot, and (d) f- \dot{x} characteristic.

during the transition, temporarily reaches its maximum value couple times before it finally stays at that value for a macroscopic sliding phase. Similarly, the acceleration signal demonstrates some distortions corresponding to these "friction-bouncing" events.

Compared to the numerical results, it seems that randomness of the friction process and velocity signal conceal part of the experimental transition features. However, the friction signal in Figure 4.1(d), particularly in the transition regions, actually reached its static friction level during the transition region, which indicates that microscale stick-slip did occur in the experiment. Therefore, the sticking dynamics during a macroscopic sticking period is more general than a purely harmonic oscillation since microscale stick-slip event is involved.

The mechanism of this event can be roughly described as follows. At the onset of

the macroscopic sticking, the contact point (y(t)) is at its maximum deflection, i.e. $y(t_1) = Y_m$, if t_1 corresponds to the instant that the mass gets stuck and $\dot{x}(t_1^-) > 0$. Then, the contact starts to recoil from this extreme deflection and experiences the high-frequency transition oscillation as a mass/spring main system with an extra spring/damper system, $K_y y + c\dot{y}$. This transition oscillation is also influenced by the low-frequency excitation of the base. When the overall force exerted by the contact point, $K_y y(t) + c\dot{y}(t)$, during this transition oscillation, exceeds the static friction force, the mass will temporarily undergo a "micro slip". This micro slip takes place for a very short duration because during a micro slip, the behavior reverts from that of the sticking equation (3.10) to the slip equation (3.9), which is independent of the compliance and damping of the contact. An important property of equation (3.9) is that it has sticking regions in the zero-velocity plane (Shaw [69]). An interpretation of this sticking region is that, both below and above the $\dot{x}=0$ plane, the vector field points toward the $\dot{x} = 0$ plane (Feeny [23]). Thus, during a micro slip in the vicinity of the sticking region, the velocity is small and the vector field quickly pushes the oscillator back to zero velocity, where it may stick again. When x and \dot{x} are no longer near the sticking region, a tiny slip leads to a macro slip.

Next, we examine the features present in the f-x and f- \dot{x} plots with the double stick-slip process. The corresponding f-x and f- \dot{x} plots are shown in Figure 4.7. There is no more detail in the f-x plots compared to Figure 4.5. Although conceptually, when micro slip occurs the mass should gain some cumulative displacement (i.e. x(t) should evolve), the numerical resolution limits the registration of this event. Similarly, the friction fluctuation during the transition should have different level (in

Figure 4.7(a)) from those of case 1. However, this can hardly be detected in Figure 4.7 for the same reason. In addition, as can be expected, the f- \dot{x} plot in Figure 4.7 contains the multiple-loop structure depicting the transition oscillation. Unlike the f- \dot{x} plot in case 1, more loops have connected themselves with the sliding-friction levels in both signs. This again illustrates the feature of micro stick-slip event.

We have shown the occurance of a double stick-slip event in both the simulation of case 2 and the experimental test. In the next section, we focus on the numerical study of the state-variable friction model which, over some parameter ranges, can depict the transition oscillation that takes place during a macroscopic stick-slip process. The goal is to understand if this friction model is able to describe both the transition oscillation and spring-like behaviors of the experimental system.

4.4 Numerical Investigations of the State-Variable Friction Model

Many state-variable friction models exist in the literature for describing the frictional memory effect (e.g. Ruina [66], Rice and Ruina [63], Dieterich [17]). These state-variable friction models were based on the observations of friction measurements of sliding rocks. While these friction models have been developed from friction experiments of rocks, their properties have recently been observed for a range of materials (Dieterich [17], [16], Dupont and Dunlap [19]). Moreover, Feeny and Moon [25] proposed their state-variable friction model to accommodate the friction behaviors observed in a dry-friction test. The general idea of state-variable friction model states that there exists an additional friction state which evolves dynamically about some backbone friction characteristics. Therefore, additional dynamics can

C

be addressed by this friction state. The backbone friction characteristics can be, for instance, Stribeck effect, Coulomb model or others. The Stribeck backbone friction characteristic, incorporated with state-variable law, is often used in the modeling of boundary-lubricated systems (Armstrong-Hélouvery et al. [3]). In this study, we adopt Coulomb law as the backbone friction characteristic. This choice was based on the preliminary experimental observations which indicated that no obvious velocity dependency was involved in the experimental friction behaviors. Similar choice has been made by Dahl in his state-variable model [14].

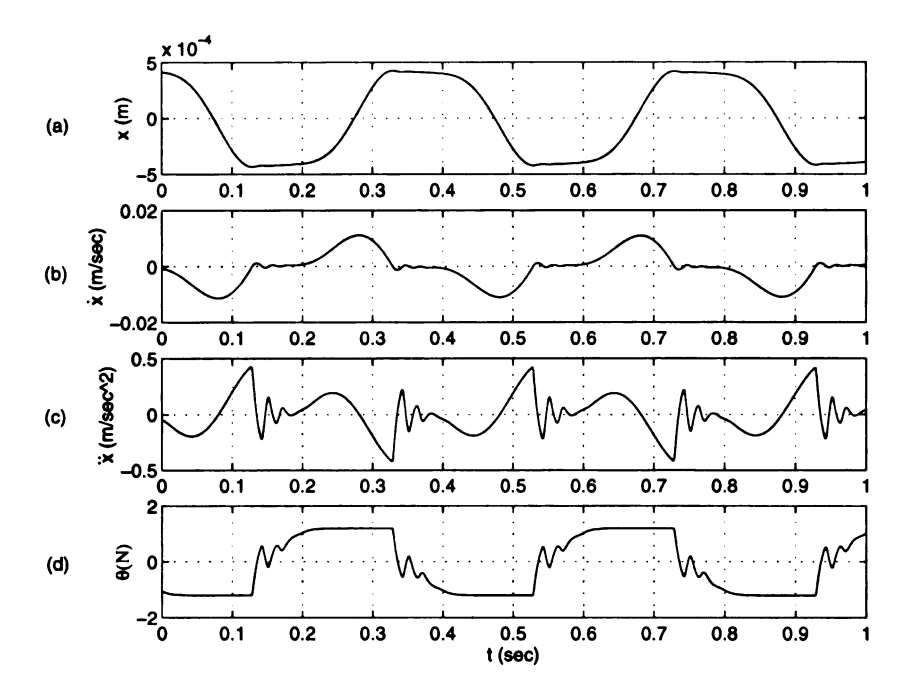


Figure 4.8: Numerical simulations of stick-slip phenomenon with the state-variable friction model, responses of: (a) displacement, (b) velocity, (c) acceleration, and (d) friction force.

According to our simulation experiences, the state-variable friction model chosen in this study, when incorporated with the system's ODE, can generate transition oscillations during the stick-slip process. This model draws our attention since it might be able to not only describe transition oscillations but also the spring-like behavior



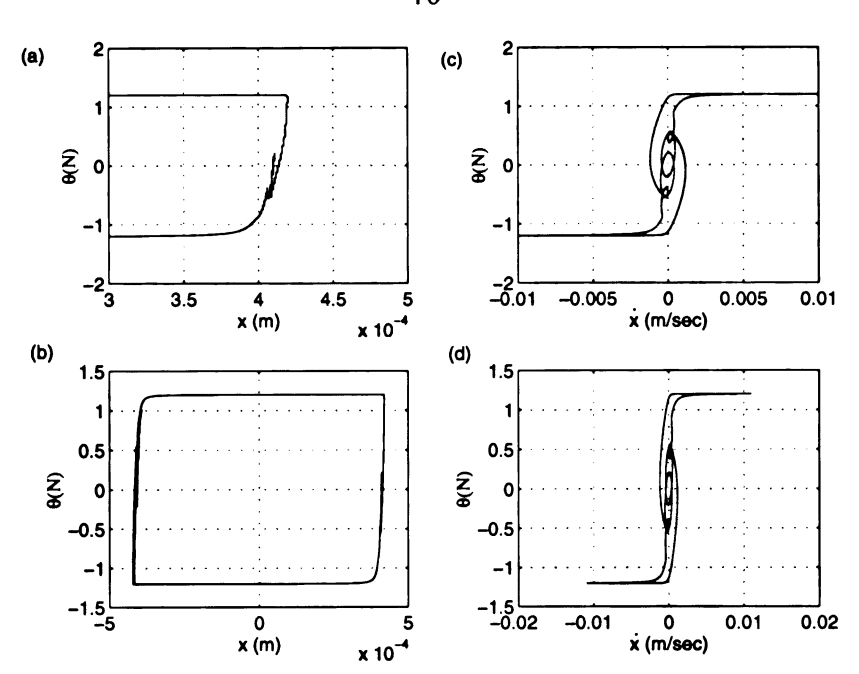


Figure 4.9: Numerical simulations of stick-slip phenomenon with the state-variable friction model, numerical versions of: (a) zoom-in detail of sticking in f-x characteristic, (b) f-x plot, (c) zoom-in detail of sticking in f- \dot{x} plot, and (d) f- \dot{x} characteristic.

of the experimental system. Therefore, we conduct several numerical simulations focusing on this friction model.

In simulation, we first tuned the parameters so that the transition oscillation in the stick-slip process can be observed, then simulations of pure-sliding motion were carried out. The state-variable friction model with the system's ODE can be written as

$$m\ddot{x} + kx(t) + \theta(t) = kZ_e \cos \omega t \tag{4.1}$$

and

$$\dot{\theta}(t) = -f_k \gamma \{ \theta(t) - f(\dot{x}) \} \tag{4.2}$$

where $\theta(t)$ denotes the friction state that tracks the backbone, steady-state friction characteristic $f(\dot{x})$. This friction state, $\theta(t)$, will be treated as friction force in this

section. Therefore, the friction responses will be labeled with $\theta(t)$ rather than f(t). The backbone friction characteristic, describing the steady-state friction-velocity relationship, is further chosen to be a smoothened Coulomb friction model, namely $f(\dot{x}) = \tanh(\alpha \dot{x})$. Although the discontinuous Coulomb friction model can be a proper candidate, the smooth version of Coulomb model, $\tanh(\alpha \dot{x})$, with a large α can catch most of the features of the discontinuous Coulomb model and is convenient for implementing the simulation.

In simulation, the value of α was chosen as 3000. Additionally, the parameter γ that dictates the speed at which $\theta(t)$ follows $f(\dot{x})$ asymptotically was tuned so that, in a macroscopic stick-slip motion, the transition oscillation emerges. The value of γ was determined to be 100. The other system parameters such as m, k, ω and f_k were the same as those in the experimental results and previous simulations of tangential contact model. Values of the excitation amplitude, X_e , were listed in Table 3.3.

Figure 4.8 and 4.9 show the simulations of a macroscopic stick-slip process. In Figure 4.8(c) and (d), the transition oscillation can be observed. However, subtle details are different from the experimental data. For example, the frequency content of the transition oscillation seems to be different from the previous study. The oscillation in Figure 4.8 actually tends to be different from a harmonic one. Because there is no physical mechanism involved in this friction model, it is difficult to conclude the cause of this transition oscillation. For different model parameters (α and γ), this transition oscillation may not occur. Thus, this transition phenomenon does not necessarily involve a definite relationship with the apparent frequency. Furthermore, there is no evidence in Figure 4.8 that points to the occurrence of macroscopic

sticking event. The motion is only a near stick-slip process in the macroscopic sense.

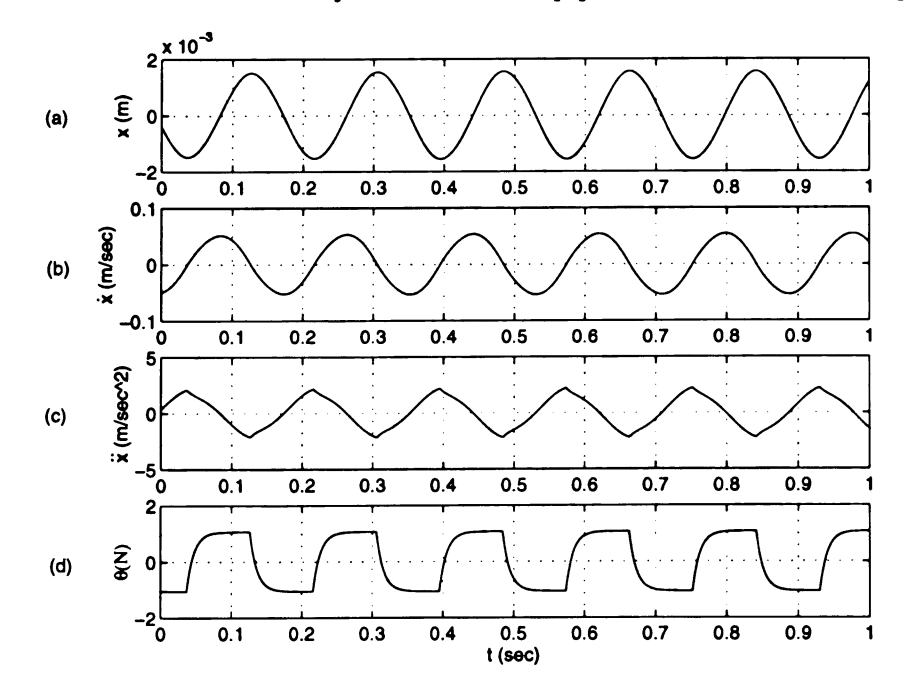


Figure 4.10: Numerical simulations of pure-sliding motion with the state-variable friction model, $\omega = 5.61$ Hz, responses of: (a) displacement, (b) velocity, (c) acceleration, and (d) friction force.

Next, Figure 4.9 illustrates the f-x and f- \dot{x} characteristics of the state-variable law. It can be seen in Figure 4.9(a) that during the direction-reversal process, the evolution of displacement is nonlinear and larger than the previous results, i.e. the results in both experiment and simulations of the tangential contact model. The f- \dot{x} plot shows the loop structure in the transition between near stick and slip. It seems that this model is not able to completely describe the macroscopic stick-slip process of the experimental system.

To further demonstrate features associated with this friction model, two macroscopic pure-sliding cases are examined in numerical simulations and the results are shown in Figures 4.10-4.13. These simulations have excitation frequencies equal to 5.61 Hz and 8.7 Hz.

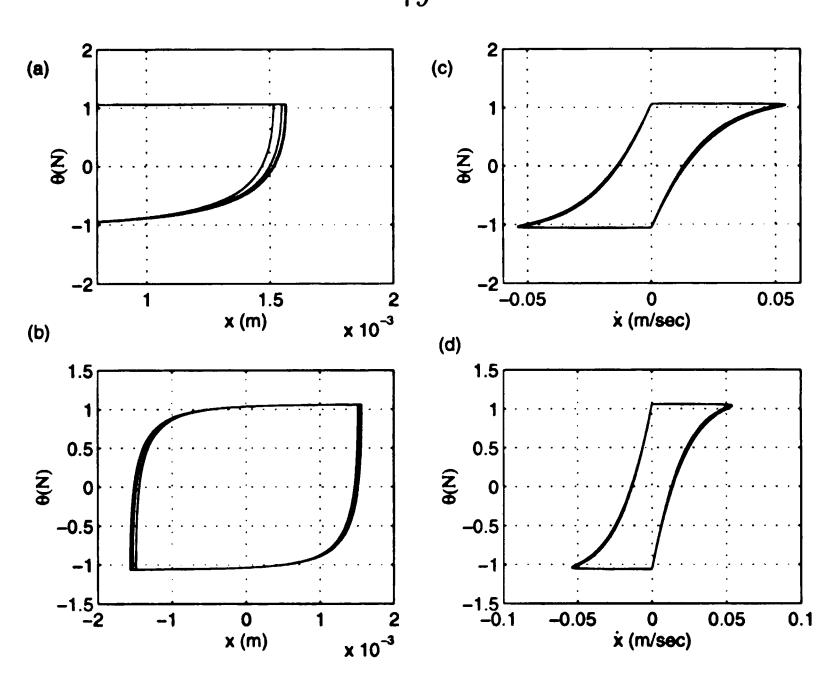


Figure 4.11: Simulation of the state-variable friction model, puresliding motion, $\omega = 5.61$ Hz, numerical versions of: (a) zoom-in detail of sticking in f-x characteristic, (b) f-xplot, (c) zoom-in detail of sticking in f- \dot{x} plot, and (d) f- \dot{x} characteristic.

Comparing these plots to their corresponding experimental result, the following observations arise. (1) While the model can describe the macroscopic feature of sliding motion, details are missing in the simulations. For instance, due to the characteristic of the state-variable friction model, the friction state, $\theta(t)$, will lag, but exponentially follow the instantaneous friction change (such friction change is depicted by the steady-state friction characteristic). Therefore, no abrupt friction or acceleration jumps can be observed in the simulated response shown in Figures 4.10 and 4.12. Instead, the friction response tends to follow the Coulomb friction behaviors asymptotically and exponentially. This feature can be seen in Figures 4.10(d) and 4.12(d). (2) In numerical versions of f-x plots which are presented in Figures 4.11(a) and 4.13(a), transition features are different from experimental data and numerical

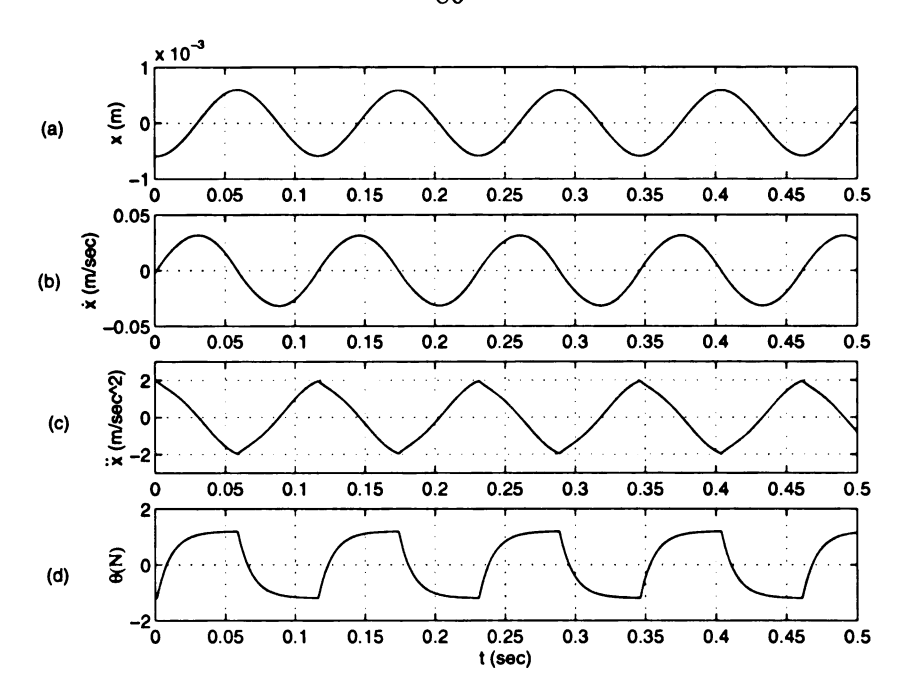


Figure 4.12: Numerical simulations of pure-sliding motion with the state-variable friction model, $\omega = 8.7$ Hz, responses of: (a) displacement, (b) velocity, (c) acceleration, and (d) friction force.

results of the tangential contact model. Much larger cumulative displacements (compared to the experimental investigations or the simulations of the tangential contact model) are involved in the direction reversal events. This indicates that the microsticking event is not responsible for the features of the state-variable friction model. Moreover, the evolution of the displacement during the direction change tends to be nonlinear. (3) While the slanted hysteretic structure appears in Figures 4.11(c) and 4.13(c), there is no horizontal tangency at the onset of stick. This feature is different from the simulation of the tangential contact model in which horizontal tangency shows up in the slip-stick transition of the f- \dot{x} plots. This different feature is again caused by the "lag" feature of the state-variable law. Since there is no microsticking event, the transition of direction reversal in backbone friction-velocity characteristic (the smooth Coulomb model) is abrupt.

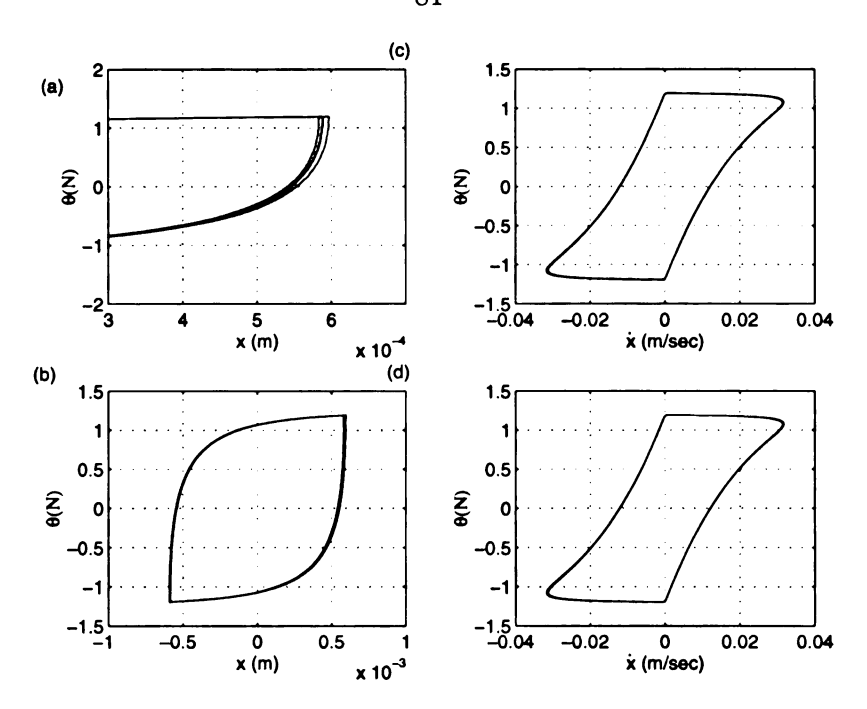


Figure 4.13: Simulation of the state-variable friction model, puresliding motion, $\omega = 8.7$ Hz, numerical versions of: (a) zoom-in detail of sticking in f-x characteristic, (b) f-xplot, (c) zoom-in detail of sticking in f- \dot{x} plot, and (d) f- \dot{x} characteristic.

The slanted hysteretic structure in f- \dot{x} plot is a typical characteristic in this state-variable friction model since it follows the stationary friction-velocity relationship. Based on this tracking feature, it is reasonable to speculate that for a constant γ , the friction state, $\theta(t)$ will deviate more from the backbone function as the excitation frequency increases. The speculation is based on the fact that the instantaneous friction changes more rapidly during a higher oscillation frequency while the tracking rate is kept the same. This can be verified by comparing the f- \dot{x} plots in Figures 4.11(c) and 4.13(c), where the latter has higher oscillation frequency, and consequently possesses a larger deviation between the backbone function and the trace of friction state, $\theta(t)$. This result also implies that in Figure 4.13(c), a longer lag occurs between the instantaneous friction change and friction state $\theta(t)$.

In accordance with the numerical investigations of the state-variable friction model, we realize that although this model somehow can depict the transition oscillation during the stick-slip process, the model cannot completely capture micro elasto-frictional behaviors that occurs in the direction reversal of pure sliding motion and in the transition of macroscopic stick-slip process. This is likely due to the fact that there is no physical mechanism involved in this friction model, which however is required to describe the sticking characteristics in a elasto-frictional system.

In what follows, we investigate a simple compliant-contact model with an inertial effect. The study starts from the description of a hypothetical compliant-contact model with imposed motion. After a coordinate transformation, the system becomes a regular forced oscillator with dry friction which is solvable and has been studied by many researchers. In the transformed problem, sticking conditions and system behaviors can be found in literature. Numerical simulations are performed to show the occurrence of microscale stick-slip phenomenon. Features in phase portraits are also discussed.

4.5 Micro Stick-Slip in a Compliant Contact with Inertia

4.5.1 Modeling of the Compliant-Inertial Contact Problem

In this section, a contact model with both compliance and inertial effects is considered. A schematic diagram is shown in Figure 4.14 where x(t) represents the imposed displacement at the contact and m and k denote the stiffness and inertia of the contact point. The friction at the interface will be modeled as Coulomb friction

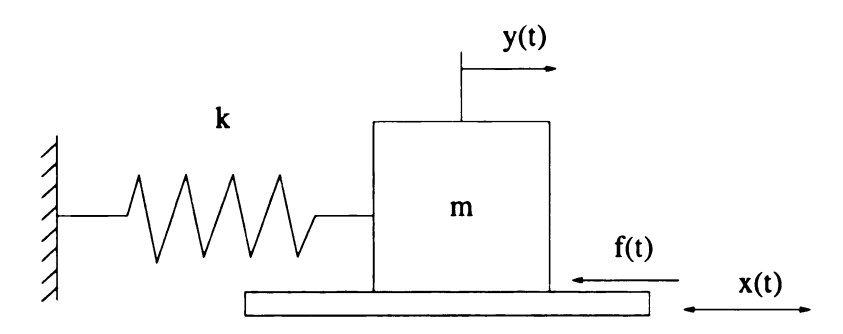


Figure 4.14: A schematic diagram showing a contact with both compliance and inertia effects.

without a difference between static and kinetic friction. Therefore, $f(t) \equiv f_k(v_r(t)) = f_k \operatorname{sign}(v_r(t)), \forall v_r(t) \neq 0$, and $-f_k < f(0) < f_k$, where $v_r(t)$ represents the relative velocity in the friction interface, so that $v_r(t) = \dot{y}(t) - \dot{x}(t)$. Next, we assume that the contact is subjected to a harmonically imposed motion, namely $x(t) = X_m \cos \omega t$. Based on this assumption, the system in Figure 4.14 can be modeled as

$$m\ddot{y} + ky(t) + f_k(v_r(t)) = 0$$
 (4.3)

Letting

$$\dot{\xi}(t) \equiv v_r(t) = \dot{y}(t) - \dot{x}(t) = \dot{y}(t) + X_m \omega \sin \omega t, \tag{4.4}$$

equation (4.3) can then be recast, using the relative coordinate $\xi(t)$, into

$$m\ddot{\xi} + k\xi(t) + f_k(\dot{\xi}(t)) = X_m(m\omega^2 - k)\cos\omega t \tag{4.5}$$

Considering $\tau = \omega_n t$, so that $\dot{\xi} = \omega_n \xi', \ddot{\xi} = \omega_n^2 \xi''$ in which $\xi' = d\xi/d\tau, \xi'' = d^2/d\tau^2$, and $\omega_n^2 = k/m$ and substituting these relationships into equation (4.5), we have

$$\xi'' + \xi(\tau) + \frac{f_k(\xi'(\tau))}{k} = X_m(\Omega^2 - 1)\cos\Omega\tau,$$
 (4.6)

where Ω is the ratio between the frequency of harmonic-input motion and the natural frequency of the contact (note that unlike the previous compliant contact model, this

model has both inertia and stiffness effects and consequently, a natural frequency), i.e. $\Omega = \omega/\omega_n$. We then normalize the above equation with $z(\tau) = k\xi(\tau)/f_k$, yielding

$$z'' + z(\tau) + \bar{f}(z'(\tau)) = \frac{X_m k}{f_k} (\Omega^2 - 1) \cos \Omega \tau, \tag{4.7}$$

where $\bar{f}(z'(\tau)) = \text{sign}(z'(\tau), \forall z'(\tau) \neq 0, \text{ and } -1 < \bar{f}(0) < 1, \text{ for } z'(\tau) = 0, \text{ denoting}$ a normalized Coulomb friction model. Thus in the relative coordinate, this contact problem becomes a regular Coulomb oscillator. Many investigations focusing on this oscillator have been put forth including stability analysis of the steady-state solutions and a criterion for sticking (Den Hartog [15], Shaw [69], and Hundal [30]). According to the above equation, the sticking region of this problem can be represented as

$$-1 + \alpha \cos \Omega \tau < z(\tau) < 1 + \alpha \cos \Omega \tau, \tag{4.8}$$

where $\alpha = X_m k/f_k(\Omega^2 - 1)$ represents the excitation amplitude in the normalized coordinate. Sticking occurs when the inequality is satisfied by some $z(\tau)$, and $z'(\tau) = 0$.

Depending on values of system parameters, the steady-state solution of this system can exhibit either continuous motion (or called macroscopic pure-sliding motion), stick-slip motion, or a permanent stop (see e.g. Shaw [69]). However, in this section, we will concentrate on the stick-slip case with many stops per forcing cycle. According to the literature, this corresponds to a case that has small frequency ratio Ω (Shaw [69], Den Hartog [15], Hundal [30]). The physical interpretation of this condition depicts a contact with high stiffness and small inertial effect subjected to a low-frequency imposed motion. Because $z(\tau)$ represents the normalized relative motion between $y(\tau)$ and $x(\tau)$, $y(\tau)$ can exhibit microscale stick-slip motion when the motion feature of $z(\tau)$ is a stick-slip process with multiple stops.

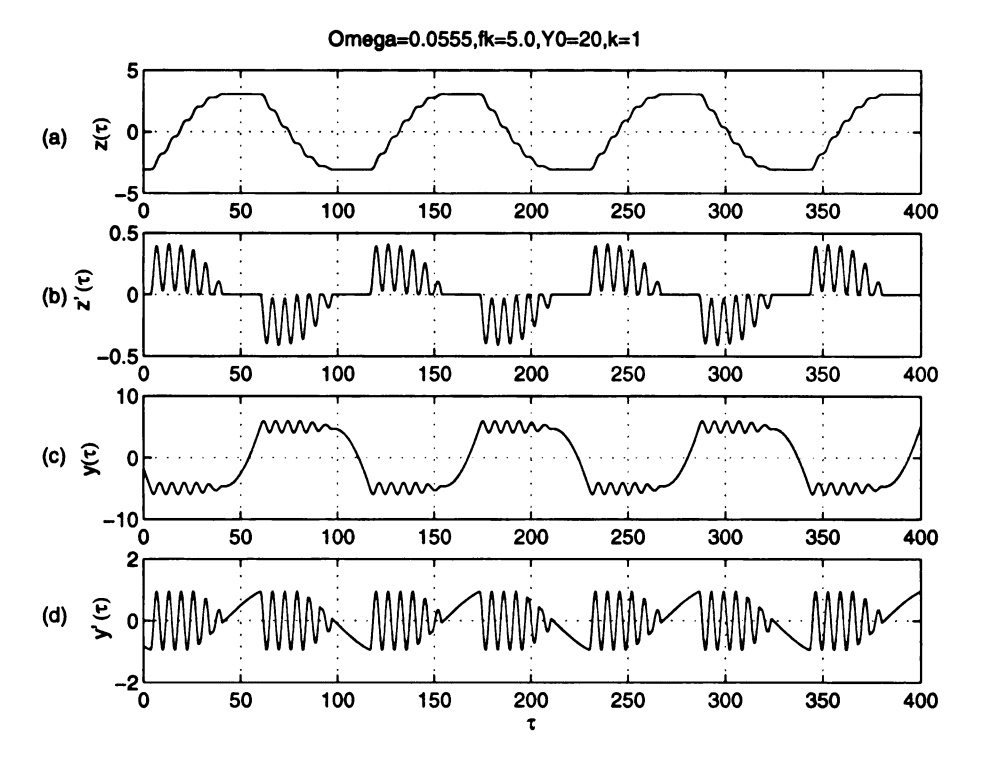


Figure 4.15: Numerical simulations of micro-scale stick-slip phenomenon, responses of the normalized: (a) relative displacement, (b) relative velocity, (c) displacement of the contact, and (d) velocity of the contact; case 1

In the next section, numerical simulations are presented to illustrate microscale stick-slip features in this compliant contact problem.

4.5.2 Numerical Simulations of Microscale Stick-Slip Motion

The values of system parameters in this section are nondimensional and normalized. Parameter values are determined so that the microscale stick-slip will occur in the response of $y(\tau)$. For simplicity of numerical simulation, the smooth version of Coulomb friction is adopted, i.e. $\bar{f}(z'(\tau)) = \tanh(\alpha z'(\tau))$, where α is chosen to be 5550 and the common parameters are $\Omega = 0.0555$, $f_k = 5.0$, and k = 1.0. Moreover, X_m is equal to 20 in case 1 and 10 for case 2. Results are presented in the

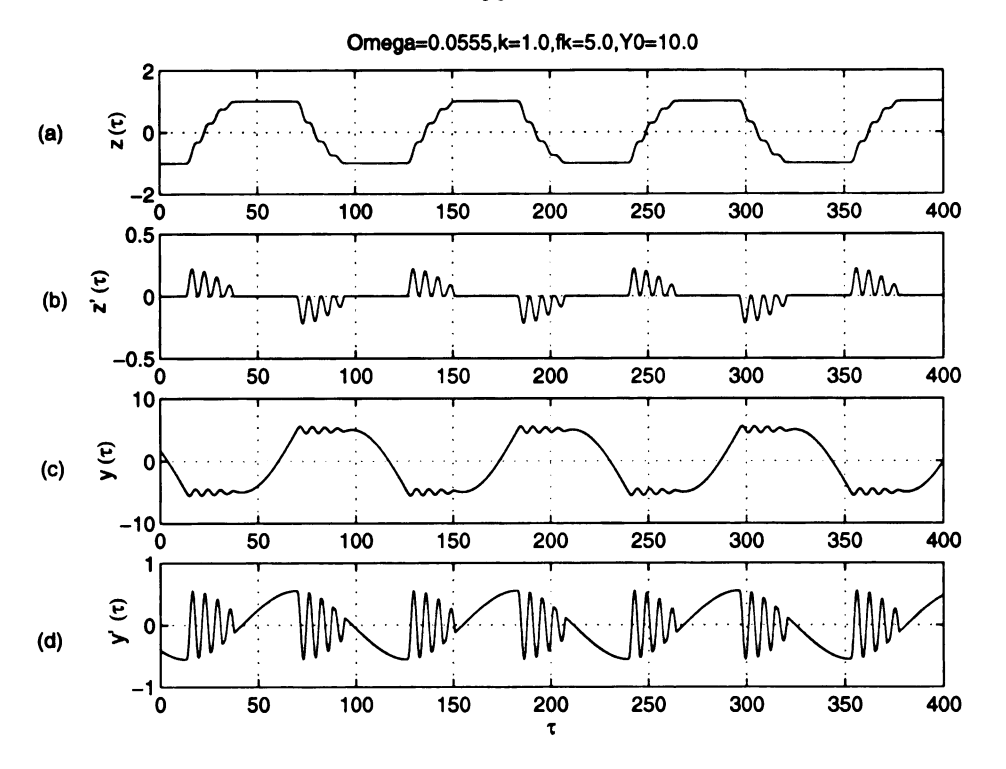


Figure 4.16: Numerical simulations of micro-scale stick-slip phenomenon, responses of the normalized: (a) relative displacement, (b) relative velocity, (c) displacement of the contact, and (d) velocity of the contact; case 2

nondimensional time coordinate " τ ".

Figures 4.15 and 4.16 present the simulation results for this compliant contact problem corresponding to different excitation amplitudes. In each plot, (a) and (b) show the multiple-stop, stick-slip motion in the normalized relative coordinate $z(\tau)$ and $z'(\tau)$. The multiple-stop feature is evident in the displacement and velocity responses of coordinate $z(\tau)$. For instance, if the macroscopic sticking event occurs, the displacement of $z(\tau)$ is a constant which equals to the maximum displacement $(Z_00r - Z_0)$, whereas $z'(\tau)$ is zero. In contrast, during the sliding phase, the relative velocity $z'(\tau)$ is nonzero and undergoes a high-frequency oscillation with a constant sign. Due to the constant sign of this high-frequency oscillation, there will be no direction reversal in this motion. There are some stops in the sliding interval corre-

sponding to $z'(\tau) = 0$. A specific feature of these stops is that the motion will resume in the same direction. The stop occurs during the sticking interval such that the motion resumes in the same direction was called an "abnormal" stop by Makris and Constantinou [42]. In contrast, if the stop involves direction reversal, it was termed "normal" stop. In [42] numerical studies were performed to analyze the motion with multiple stops per forcing cycle.

When the motion in $z(\tau)$ has multiple stops per forcing cycle, microscale stick-slip feature appears in the responses of the contact motion, i.e. $y(\tau)$ and $y'(\tau)$. These responses are illustrated in Figures 4.15 and 4.16(c) and (d). In both cases, $y(\tau)$ has two DC positions (positive and negative) which represent correspond to maximum static deflections of the contact. At these biased positions, the high-frequency sliding motion are occurring. In the same figure, the low-frequency harmonic curves depict the macroscopic sticking motions. The contact moves from one extreme deflection to the other when macroscopic sticking occurs. The high-frequency sliding oscillation starts right after the contact point switches its DC displacements. Similarly, in the time histories of $y'(\tau)$, evident features exist to describe the macroscopic sticking, high-frequency sliding, and microscale sticking events. A striking feature in $y'(\tau)$ response shows that both the macroscopic and microscale sticking events follow the same sticking boundary.

A simple description of the microscale stick-slip mechanism follows. Assuming that the relative motion, $z(\tau)$, undergoes a macroscopic sticking process, which implies that during this sticking interval $z(\tau)$ is a constant represented as $z(\tau) = \pm Z_0$. This macroscopic sticking feature of $z(\tau)$ can be seen in Figure 4.15(a) in which $\pm Z_0$

are positions corresponding to the normal stops. During these sticking intervals, motions in both $x(\tau)$ and $y(\tau)$ are exactly the same such that the normalized relative displacements $\pm Z_0$ are constants. Due to the fact that $x(\tau)$ is a low-frequency harmonic function in this macroscopic sticking motion, $y(\tau)$ depicts part of a low-frequency function as well. This event can be observed in Figure 4.15(a) and (c).

Conversely, when $z(\tau)$ experiences the macroscopic sliding motion, there will be multiple abnormal stop events involved in an otherwise sliding motion as shown in Figure 4.15(a). Hence, motion features of $y(\tau)$ during such interval include a high-frequency oscillation with some distortions. The distortions result from the appearances of the microscale sticking events. Because these microscale sticking trajectories follow a slow harmonic instead of fast harmonic as in the high-frequency oscillation, the apparent motion features are different.

In order to demonstrate the boundaries for the macroscopic and microscale sticking events, the following are considered. According to the literature (Shaw [69], Hundal [30]), during a macroscopic sticking interval, displacement $z(\tau)$ is a constant, i.e. $z(\tau) = \pm Z_0$. The magnitude of Z_0 can be determined numerically if values of system parameters are known (Shaw [69] and Hundal [30]). Based on Z_0 and the definition of the normalized relative coordinate $z(\tau)$, we have

$$\tilde{y}_s(\tau) = \pm Z_0 \frac{f_k}{k} + X_m \cos \Omega \tau \tag{4.9}$$

Here, $\tilde{y}_s(\tau)$ represents the boundary of $y(\tau)$ during a macroscopic sticking event, and the subscript "s" denotes the macroscopic sticking condition. This subscript distinguishes it from the microscale sticking condition in which subscript "ms" is adopted. A plot illustrating this macroscopic sticking boundary, $\tilde{y}_s(\tau)$, as well as the contact

displacement $y(\tau)$ (corresponding to case 2) are shown in Figure 4.17(a). Apparently, during the macroscopic sticking interval, $y(\tau)$ follows the sticking boundary perfectly.

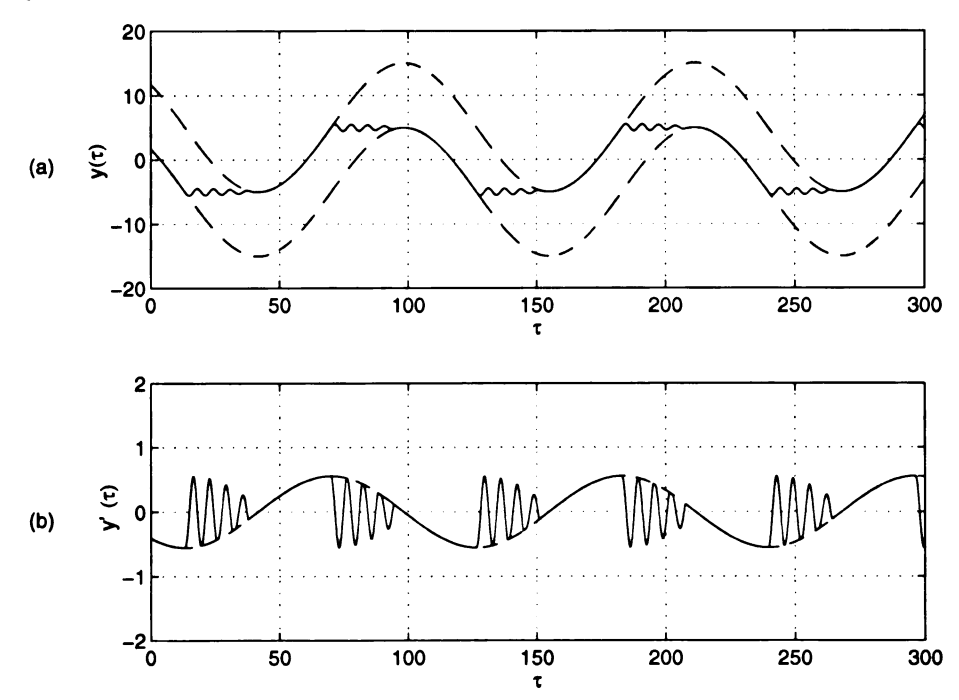


Figure 4.17: Sticking boundaries and double sticking events, (a) macroscopic sticking boundary, $\tilde{y}_s(\tau)$ (dashed line), and $y(\tau)$ (solid line) and (b) microscale sticking boundary $\tilde{y}'_{ms}(\tau)$ (dashed line) and $y'(\tau)$ (solid line); case 2.

To search for microsticking boundary, we realize that when the microsticking process happens, there will be different positions of $z(\tau)$, denoted as Z_{0i} , associated with these microscale events. These definite positions of $z(\tau)$ can be observed in Figures 4.15 and 4.16(a). The subscript "i" indicates the appearance order of these abnormal stick events. As with the idea in the macroscopic sticking case, the boundaries for different microsticking events can be generalized as

$$\tilde{y}_{msi}(\tau) = \pm Z_{0i} \frac{f_k}{k} + X_m \cos \Omega \tau \tag{4.10}$$

Equation (4.10) depicts a family of boundary curves with different parameter values

 Z_{0i} . Although it seems to be difficult to solve for the microsticking displacements Z_{0i} , the velocity of contact $y'(\tau)$ follows the derivative of \tilde{y}_{msi} which is a single curve and denoted as \tilde{y}_{ms} (the subscript "i" has been dropped since there is no difference between different microsticking events for this velocity boundary). Thus, the velocity boundary of microscopic sticking process can be represented as $\tilde{y}'_{ms}(\tau) = -X_m\Omega\sin\Omega\tau$. Features of micro sticking and its velocity boundary are presented in Figure 4.17(b). In this figure, $y'(\tau)$ matches $\tilde{y}'_{ms}(\tau)$ exactly during the occurrence of microsticking events.

In summary, we have shown that the microscale stick-slip event can occur in a compliant contact with inertia effect. The complete response of the contact includes two scales of sticking events and a high-frequency sliding process. Features of this motion resembles the double stick-slip process addressed earlier in this chapter.

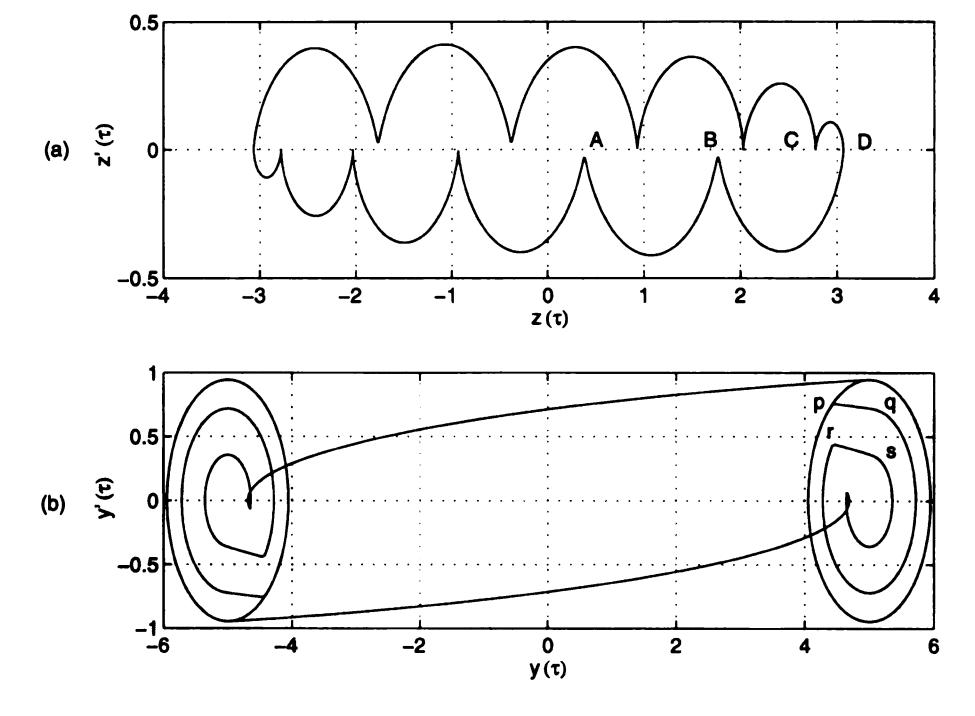


Figure 4.18: Phase portraits of (a) relative coordinate and (b) coordinate of the contact point; case 1.

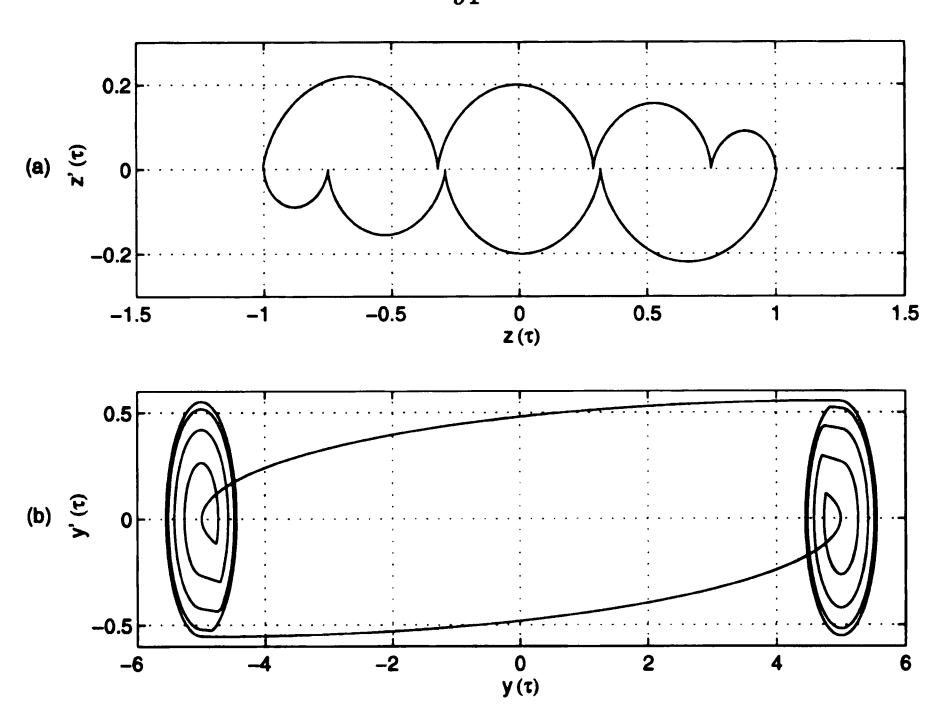


Figure 4.19: Phase portraits of (a) relative coordinate and (b) coordinate of the contact point; case 2.

Next, we show some phase portraits. In figures 4.18 and 4.19, phase portraits are presented. In each figure, (a) demonstrates the phase portrait in z coordinate and (b) shows the phase portrait in y coordinate. Phase portraits in z coordinate provide some useful information. For instance, the number of microscale sticking events can be found in Figure 4.18(a) where points A, B and C correspond to microsticking events and point D represents a macroscopic sticking event. Additionally, the displacement of point D equals $+Z_0$ and displacements of points A, B, and C are equal to $+Z_{0i}$ with i=1,2,3. Therefore, one can justify the occurrence of double sticking event from this phase portrait.

In contrast, the phase portrait in y possesses more physical informations. As can be seen in Figures 4.18 and 4.19(b), two well-like structures emerge with centers at two DC displacements (± 5) which represent the static deflections of the contact.

Centering at the DC displacements, the high-frequency microscale stick-slip process occur. The high-frequency, microscale sliding process depicts itself in a well-like structure, consisting of swirling ellipses, with part of its trajectory involving the microsticking events. These microsticking events, shown as segments pq and rs in Figure 4.18(b), follow a family of large ellipses which are not presented in this figure. There are two curves connecting the well-like structures. These curves represent the macroscopic sticking motion.

In what follows, conclusions are given for the investigations of sticking dynamics as well as different scales of stick-slip processes.

4.6 Conclusions

In this chapter, we experimentally observed a macroscopic stick-slip process. A free-vibration test was conducted for identifying the frequency of oscillation while stuck. This frequency matched the transition-oscillation frequency during the stick-slip process. Furthermore, it agreed with the predicted frequency based on the contact stiffness found in Chapter 3. Thus, oscillations occurring during stick-slip transitions are likely to be caused by contact compliance.

A double stick-slip event has been confirmed to occur in the experimental stick-slip process. Through numerical simulations using the compliant tangential contact model, the double stick-slip event was further demonstrated. It was found that the transition oscillation occurring during a macroscopic stick-slip process is not necessarily a purely harmonic oscillation. It can be more complicated due to the presence of a microscale stick-slip phenomenon.

The investigations of the state-variable friction model indicate that because of lack of a physical mechanism, this model cannot completely describe the transition behaviors in either macroscopic pure-sliding motion or macroscopic sticks-lip process. However, a slanted hysteretic feature was found in the f- \dot{x} plot for the simulation in pure-sliding motion. The slanted degree increases with the excitation frequency if the other system parameters are kept the same.

Numerical studies of a compliant contact with the inertial effect are conducted to illustrate microscale stick-slip process. The microscale stick-slip occurs when the frequency of harmonical-imposed motion is much lower than the natural frequency of the contact. Characteristics in both time-domain response and phase portrait are addressed.

Regarding the investigations of the compliant-contact problem discussed in Chapters 3 and 4, a single, tangential compliant contact model was used to interpret two experimentally observed friction phenomena of a real system. Both the spring-like sticking behavior in a macroscopic sliding motion and the transition oscillation during a macroscopic stick-slip process can be modeled using this compliant contact model.

In the case of pure-sliding motion, a geometric analysis revealed a transition speed which depends on the amplitude/frequency of oscillation, the friction level, and the contact stiffness. It also provided a means of experimentally estimating the contact stiffness. The spring-like sticking behavior manifested itself in a slanted hysteretic structure which was predicted in the analysis, observed in sliding experiments, and reproduced in numerical simulations. The study showed the ability of the complaint

contact model to describe the spring-like friction behavior of a real system.

The same contact model was used to estimate the frequency of the transition oscillation during a macroscopic stick-slip process. It was found that the predicted frequency based on the compliant contact model agreed with the experimental-observed frequency which was confirmed by a free-vibration test. Furthermore, a double stickslip event was illustrated in the experiment system. Numerical simulations, using the idealized compliant contact model incorporated with damping, were used to further illustrate the mechanism of this double stick-slip event.

CHAPTER 5

WAVELET ANALYSIS OF STICK-SLIP IN AN OSCILLATOR WITH DRY FRICTION

5.1 Introduction

In this chapter, we characterize the stick-slip motion which has been shown to exist in a frictional oscillator numerically and experimentally in the previous chapters. Our approach is to apply the wavelet transform for the time-frequency analysis of stick-slip transition behaviors. Numerical and experimental acceleration signals will be analyzed. The goal is to explore the time/frequency transition features associated with different friction models. These wavelet transition features can be used as a tool in analyzing the experimental stick-slip signals.

The wavelet transform has attracted the attention of vibration researchers. For example, Newland [52], [53] developed discrete wavelet transform maps and studied some transient vibration signals. Önsay and Haddow [55] used wavelet transform to analyze the transient wave propagation behavior of beam vibration in dispersive medium in which the Morlet wavelet was adopted. Kishimoto et al. [37] applied wavelet transform to study a similar dispersive wave propagation problem in a flexible beam vibration where the Gabor wavelet was employed. Liang and Feeny [40] used wavelet transform to detect the existence of subsystem dynamics occurring during

the transition of stick-slip friction process. The Morlet wavelet was employed in that study. Applications of wavelet transform are also found in the defect detection of mechanical components or machine tools (Li and Ma [39], Tansel et al. [74] and Pandit et al.). In the longterm the wavelet transform may help in the study of stick-slip, perhaps in understanding the connection between the normal-directional motion and tangential sliding behavior, which was emphasized by Oden and Martins [54]. Evidence shows that the normal-directional motion has frequency contents much higher than the tangential ones, such that it might be possible to distinguish the individual effect in different directional dynamics through the use of the wavelet transform. Moreover, it is known that a controlled dither input can eliminate stick-slip (Armstrong-Hélouvry et al. [3]). Through the identification of frequency contents in transition behaviors, some insight might be obtained for choosing the appropriate dither signals.

There are other modern signal-processing techniques which can deal with the signals containing a wide range of frequency components. For example, the short-time Fourier transform (STFT) uses a translational window in the time domain and expands the frequency contents with respect to signal inside the window (Allen and Rabiner [1], Portnoff [59]). Thus, the STFT can be interpreted as a general Fourier transform with time localization. Due to the uncertainty principle, the resolutions in time and frequency of this approach cannot be arbitrarily small, which limits the application of this method (Vetterli [78]). The wavelet transform is an alternative to the STFT. In contrast to the STFT, which uses complex sinusoids as basis functions and averages the signal over a constant-length time window for obtaining frequency

information, the wavelet transform uses a "mother wavelet" associated with different window sizes and time locations to generate its basis functions. The time-frequency resolution of the wavelet transform involves a different trade-off to the one by the STFT: at high frequencies the wavelet transform is sharper in time, while at low frequencies, the wavelet transform is sharper in frequency. Thus, a particular property of this transform is its ability to identify and isolate the fine temporal, high-frequency structure of a signal.

The high-frequency transition oscillation associated with the low-frequency stick-slip response suggests that a stick-slip signal is a good candidate for applying the wavelet transform. We will compare the simulated stick-slip data with the experimental ones. Three friction models are examined in the numerical study which include the Coulomb law, the state-variable law, and the compliant tangential contact model. For some parameter ranges, the state-variable law used in this study has been shown to cause the transition oscillations in the stick-slip acceleration signal. In contrast, if we consider a forced mass-spring system with dry friction modeled by the Coulomb law, abrupt jumps occur in the friction force and acceleration at the instant that the mass sticks. This jump event dictates the high-frequency components. Furthermore, features of the experimental data as well as the simulations of tangential contact model showed not only the transition oscillations but also the double stick-slip event. Wavelet transition features associated with different friction models are the focus of this study.

The organization of this chapter is as follows. Section 5.2 gives a brief review of the wavelet transform. It includes the numerical algorithm which is validated

with some benchmark examples. In Section 5.3, wavelet transform is applied to the numerical stick-slip acceleration signals to generate wavelet contour plots and corresponding transition features of different friction models. These results are then compared to the experimental ones. This chapter is concluded in the Section 5.4 in which observations made from the wavelet contour plots are addressed with regard to the coupling dynamics and double scale stick-slip process.

5.2 Wavelet Transform

The mathematical definition of continuous wavelet transform is given as an inner product of a signal and a particular set of functions

$$CWT_x(a,b) = \int_{-\infty}^{\infty} x(t)h_{a,b}^*(t)dt.$$
 (5.1)

where $h^*(t)$ represents the conjugate of h(t). Equation (5.1) measures the "similarity" between the signal x(t) and the basis functions

$$h_{a,b}(t) = \frac{1}{\sqrt{|a|}} h(\frac{t-b}{a})$$
 (5.2)

called wavelets, in which $a, b \in \Re$, $a \neq 0$, and the constant $1/\sqrt{|a|}$ is used for energy normalization. The parameters a and b determine the dilation and translation of the mother wavelet which is chosen here as the Morlet wavelet (Morlet and Arens [49], [50], Önsay and Haddow [55]) and is given by

$$h(t) = \pi^{-1/4} (e^{-i\omega_c t} - e^{-\omega_c^2/2}) e^{-t^2/2}, \tag{5.3}$$

$$H(\omega) = \pi^{-1/4} \left[e^{-(\omega - \omega_c)^2/2} - e^{-\omega_c^2/2} e^{-\omega^2/2} \right]$$
 (5.4)

where ω_c is the center frequency of the mother wavelet. $H(\omega)$ represents the Fourier transform of h(t). The wavelet basis functions have no DC component, i.e. $H(\omega)$ evaluated at $\omega = 0$ is zero. The second term in the bracket on the right-hand side of Eq. (5.3) exists for the purpose of reconstructing (or inverse) process. In practice, it can be neglected (Önsay and Haddow [55]). Therefore, it will not be included in our calculations.

The analyzing wavelet function, h(t) $(H(\omega))$, can also be considered as a window function both in time and frequency domain. Equations (5.3)and (5.4) state that the time window h(t) is centered at t=0, whereas the frequency window $H(\omega)$ is centered $\omega=\omega_c$. To show this feature, time and frequency domain representations of the Morlet wavelet are presented in Figure 5.1 in which the parameters are $a=1,b=0,\omega_c=4$. When the translation and dilation actions are switched on, the time window will be centered at t=b and the frequency window at $\omega=\omega_c/a$ as shown in equation (5.2).

In order to implement the calculation of the wavelet transform, a sublattice is constructed by discretizing the values of a and b. Fixing the dilation and translation step sizes to a_0 and b_0 , and defining

$$a = a_0^m; b = nb_0 a_0^m (5.5)$$

with $m, n \in \mathbf{Z}$, results in

$$h_{mn}(t) = a_0^{-m/2} h(a_0^{-m}t - nb_0).$$
 (5.6)

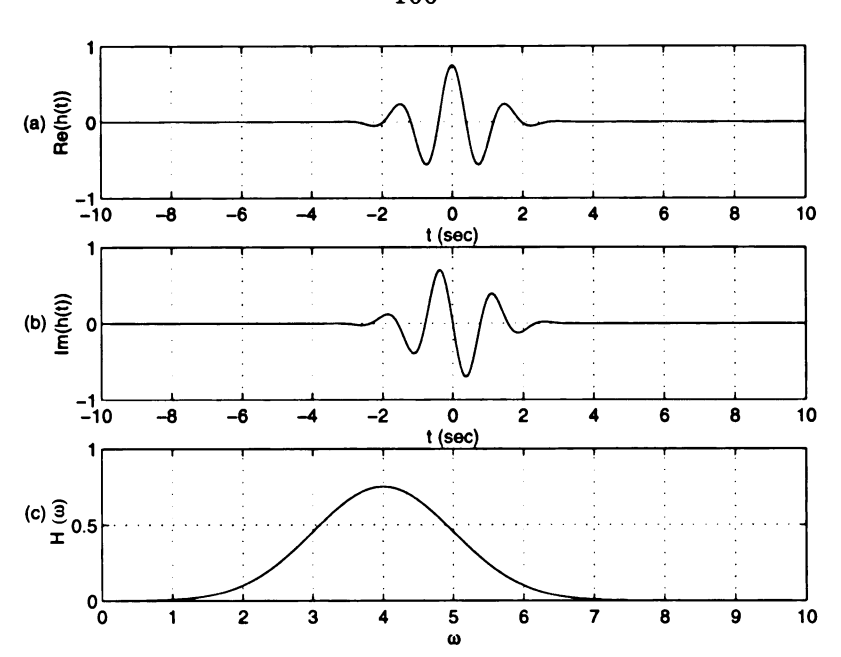


Figure 5.1: Representations of Morlet wavelet function: (a) real part of h(t) (b) imaginary part of h(t) (c) Fourier transform $H(\omega)$.

Based on equation (5.5), the translation step b depends on the dilation step a. This choice is natural, since long wavelets will then advance by large steps and short ones by small steps. On this discrete grid, the wavelet transform is thus

$$WT_x(m,n) = a_0^{-m/2} \int_{-\infty}^{\infty} h^*(a_0^{-m}t - nb_0)x(t)dt.$$
 (5.7)

Of particular interest is the discretization on a dyadic grid which occurs for $a_0 = 2$, $b_0 = 1$ and is used in this study. A schematic diagram illustrating the grid structure on the time-frequency plane for Fourier transform, STFT, and wavelet transform is presented in Figure 5.2. It can be observed from this figure that different window lengths are used in these transform methods. For instance, Fourier transform uses only one long window to capture the frequency contents of the input signal. The STFT translates a fixed-length window into different time locations to measure the

frequency contents of signal inside the window. In contrast to these two approaches, wavelet transform employs various window lengths in accordance with the frequency contents of the signal and also translates windows along the time axis.

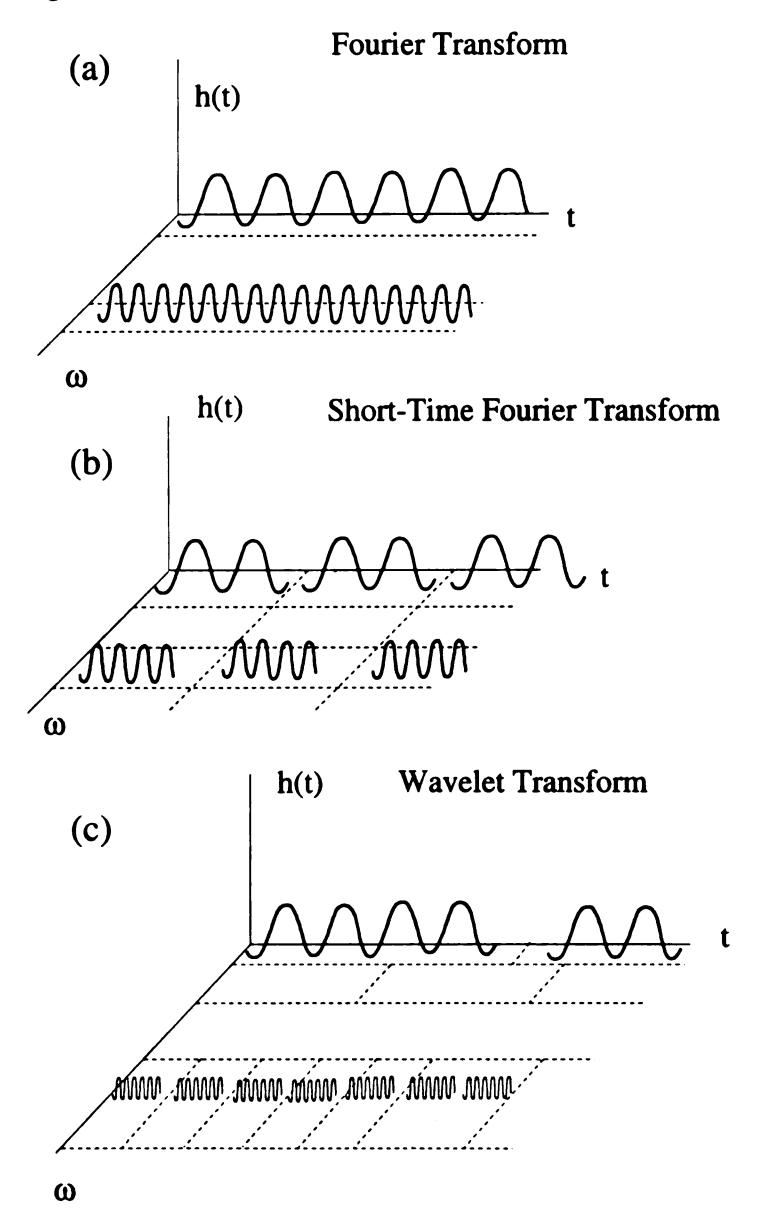


Figure 5.2: Window representations in the time-frequency plane: (a) Fourier transform (b) STFT (c) wavelet transform.

To implement the calculation of wavelet coefficients, $WT_x(m,n)$, the numerical integration scheme is adopted. This algorithm may not be efficient in the compu-

tation sense. However, the number of data points in this study is not huge. Same algorithm was used by Kishimoto et al. [37] successfully in studying a flexible beam vibration problem and by Liang and Feeny [40] for a transient friction vibration investigation. There are other algorithms which can be found in the signal processing literature (Önsay and Haddow [55]; Newland [52], [53]).

If we apply this computation scheme to the benchmark signals such as sinusoids and impulses, it gives reasonable results. For example, in Figure 5.3 an impulse signal was used to conduct the wavelet transform. The results of wavelet transform is presented in Figure 5.3(b) by a contour plot in which 12 contour curves are used to span the distance between the maximum wavelet coefficient and a threshold value. This threshold is a small positive constant, and it was chosen so that any wavelet coefficient less than this number is made to be equal to it. In contour plot, this threshold value corresponds to the blank region. Therefore, the contour plot essentially demonstrates the wavelet coefficient distribution above the threshold plane. Heights of different contour surfaces are showed in the logarithmic scale. Furthermore, while the subtle contour structure might be different when the threshold value is changed, the main contour structure will not change dramatically. This feature will be addressed more later in this chapter. The center frequency ω_c is 4.5 hereafter.

In Figure 5.3, the contour plot captures most of the impulse properties in time and frequency domains. These features include the broad frequency content of the impulse signal which is illustrated by a vertical banded contour crossing the entire frequency range at the middle of the time axis. Additionally, the vertical contour structure points correctly at the occurrence of the impulse in the time axis. This

demonstrates the zooming ability of wavelet transform in isolating the fine temporal event. The spread-out feature in contour plot indicates the trade-off resolution relationship between time and frequency domains, i.e. higher frequency resolution in the low-frequency ranges and higher time resolution in the high-frequency ranges.

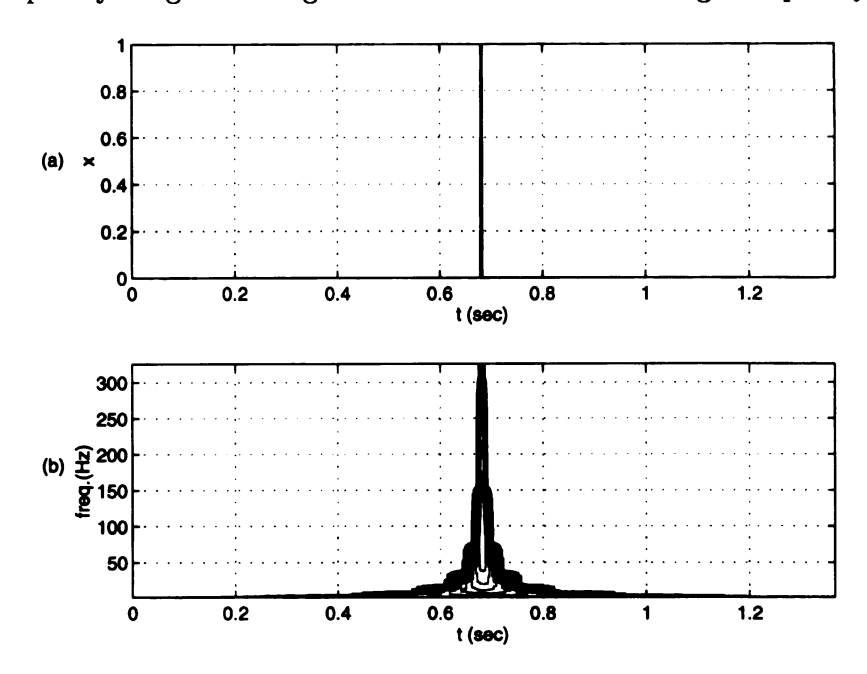


Figure 5.3: Wavelet transform of an impulse signal: (a) input signal (b) wavelet contour plot.

Another example exhibiting a low-frequency sinusoidal function superimposed by an impulse at the middle is shown in Figure 5.4(a). Wavelet transform conducted with respect to this signal is presented in Figure 5.4(b) in which the wavelet contour plot is able to detect different frequency contents of this combined-frequency signal. For instance, a horizontal banded structure, corresponding to the frequency of the input sinusoidal function, occurs over the entire time axis. In contrast, the vertical spike points to the occurrence of impulse signal. The blurred structure at both ends of the time axis are resulted from the zero elements padded outside the time window for the computing process.

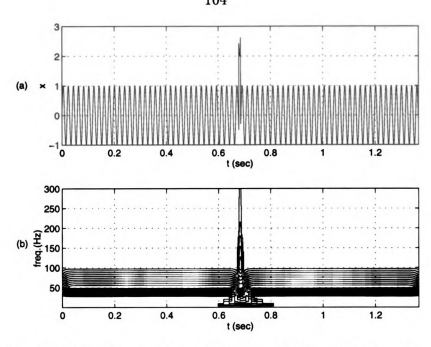


Figure 5.4: Wavelet transform of a sinusoidal function carrying an impulse signal: (a) input signal (b) wavelet contour plot.

Through the tests on benchmark signals, we have shown that wavelet transform can efficiently detect time/frequency informations of a input signal. In the next section, this method will be used to investigate both simulated and experimental acceleration signals that contain stick-slip motion.

5.3 Wavelet Transform of Stick-Slip Signals

This section includes numerical examples of stick-slip accelerations and their corresponding wavelet transforms. Parameter values are the same as those given in Chapter 4. The simulations of the tangential contact model and state-variable model have been conducted in Chapter 4. Hence, signals of these two models will be applied directly in this chapter, whereas the following describes the simulation of the Coulomb law.

Numerical integration of the Coulomb friction model is difficult because of the

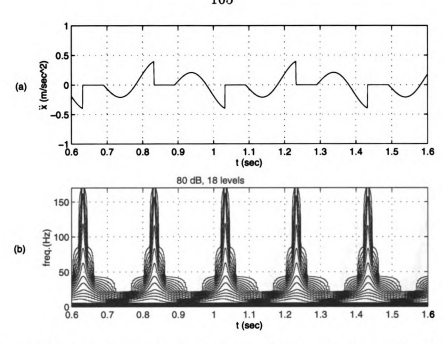


Figure 5.5: Wavelet analysis of the simulated stick-slip acceleration, Coulomb friction model: (a) time-domain response, and (b) wavelet contour plot.

discontinuity feature at zero velocity. Many researchers have proposed different prescriptions for solving this problem (e.g. Shaw [69]; Feeny and Moon [25]; Meijaard [45]). Our approach follows the method used in Shaw [69] and Feeny and Moon [25]. A fifth-order Runge-Kutta algorithm was chosen to implement the integration of system's ODE.

A stick-slip acceleration signal, corresponding to Coulomb friction feature, is presented in Figure 5.5(a) in which jump event occurs at each onset of sticking. This jump is a high-frequency event. Moreover, during the sticking interval, the acceleration is zero. These events will address different characteristics in the wavelet contour plot. For instance, in Figure 5.5(b), the wavelet contour plot shows many spikes which dictate the occurrences of jump events. While it is not clear, the maximum wavelet coefficient occurs at the forcing frequency (2.5 Hz). There are

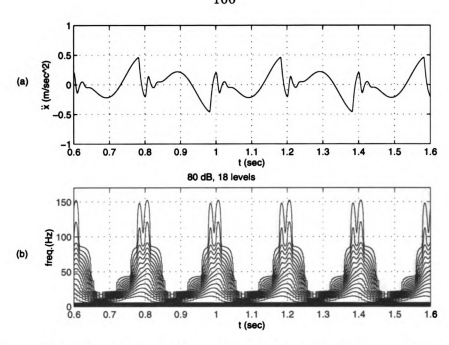


Figure 5.6: Wavelet analysis of the simulated stick-slip acceleration signal, state-variable friction model: (a) time-domain response, and (b) wavelet contour plot.

18 contour curves spanning the distance of 80 dB between the maximum wavelet coefficient and the threshold. In what follows, we will apply a constant span (80 dB) for different simulation cases and the experimental data, so that the global contour structure can be compared.

The simulation and wavelet results focusing on the state-variable friction model are presented in Figure 5.6. Unlike the Coulomb case, no abrupt jump event occurs in the acceleration response. Consequently, the wavelet contour plot does not register the pronounced spike similar to the Coulomb model case. Instead, the transition oscillations occur during the sticking interval which are depicted by the less-pronounced spike structures.

Compared to the Coulomb and state-variable friction models, the simulations of the tangential contact model illustrates more interesting transition features. Fig-

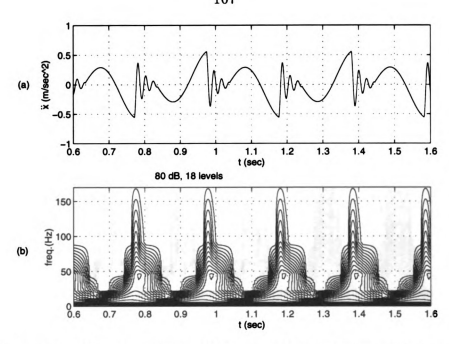


Figure 5.7: Wavelet analysis of the simulated stick-slip acceleration, tangential contact model, case 1: (a) time-domain response, and (b) wavelet contour plot.

ure 5.7 demonstrates the stick-slip acceleration of the tangential contact model corresponding to a higher damping case (case 1) in Chapter 4. According to the investigation performed in Chapter 4, we know that there is no micro slip event involved in this case. Thus, the time-domain transition oscillation (Figure 5.7(a)) is very much like a damped sinusoidal function. Figure 5.7(b) illustrates this transition oscillation by two striking features. First, a local maximum of wavelet coefficients emerges in the transition contour structure. This local maximum manifests itself in a circle-like shape centering about 47 Hz. Secondly, only one major spike appears in every transition from sliding to sticking. These features indicate that the transition oscillation in this case resembles a single harmonic function with 47 Hz oscillation frequency. The wavelet contour plot of this case is different from those of the state-variable and Coulomb cases in which no local maximum exists during the stick-slip transition.

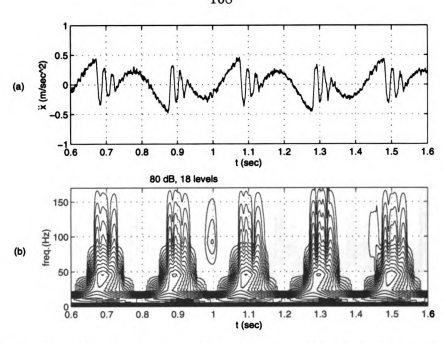


Figure 5.8: Wavelet analysis of the experimental stick-slip acceleration: (a) time-domain response, and (b) wavelet contour plot.

Therefore, we have shown the wavelet transition features of the Coulomb, the state-variable, and the tangential contact model of case 1. It can be summarized that if the transition oscillation is close to a sinusoidal one, there will be a local maximum corresponding to the oscillation frequency. Based on this, the transition oscillation occurring in the state-variable model case is not close to a sinusoidal function. Additionally, the wavelet contour plot in Figure 5.5(b) does reflect the fact that there is no oscillation involved, during the transition phase, of the Coulomb friction case. The samll circle-like structure is called the local maximum because the global maximum is a 2.5 Hz plead existing along the entire time axis which corresponds to the low-frequency forced response.

Next, we show the experimental acceleration and its wavelet contour plot in Figure 5.8. Similar local maximum structure appears in Figure 5.8(b) depicting a nearly



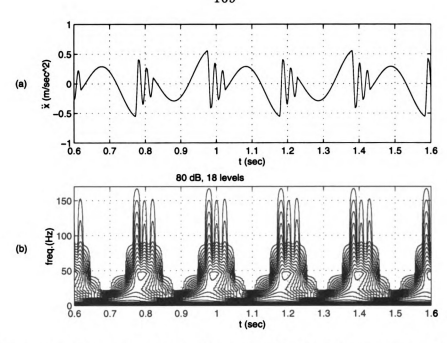


Figure 5.9: Wavelet analysis of the simulated stick-slip acceleration, tangential contact model, case 2: (a) time-domain response, and (b) wavelet contour plot.

sinusoidal oscillation. The ungrouped contour structures, existing around t=1 sec and t=1.45 sec, are the results of the irregularities in response. These are possibly caused by the surface roughness. Furthermore, there are several grouped spike structures occurring during each transition phase. The grouped spikes are resulted from two possible mechanisms including the micro slip event and the irregularity of response. A detail investigations focusing on the spike structure caused by micro slip event is concerned next.

To explore the grouped spike structure associated with the micro slip event, we show the simulation acceleration and its corresponding wavelet plots in Figure 5.9. This simulation case is equivalent to the tangential contact model with light damping which was denoted as case 2 in Chapter 4. Similar to the experimental and simulation of tangential contact model, case 1, there are local maximum structures occurring in

Figure 5.9(b). This local maximum contour describes the nearly sinusoidal feature of the transition oscillation in Figure 5.9(a). In addition, several grouped spikes occur during each transition interval illustrating the micro slip events. Before we further verify this statement, we would like to point out that the grouped spike structures are more-or-less consistent with those of the experimental case. The presence of randomness on the experimental signal conceals its wavelet representation, hence, quantitative comparison between Figures 5.8(b) and 5.9(b) is not a trivial task. Nevertheless, the qualitative characteristics of these two wavelet contour plots definitely show some consistencies.

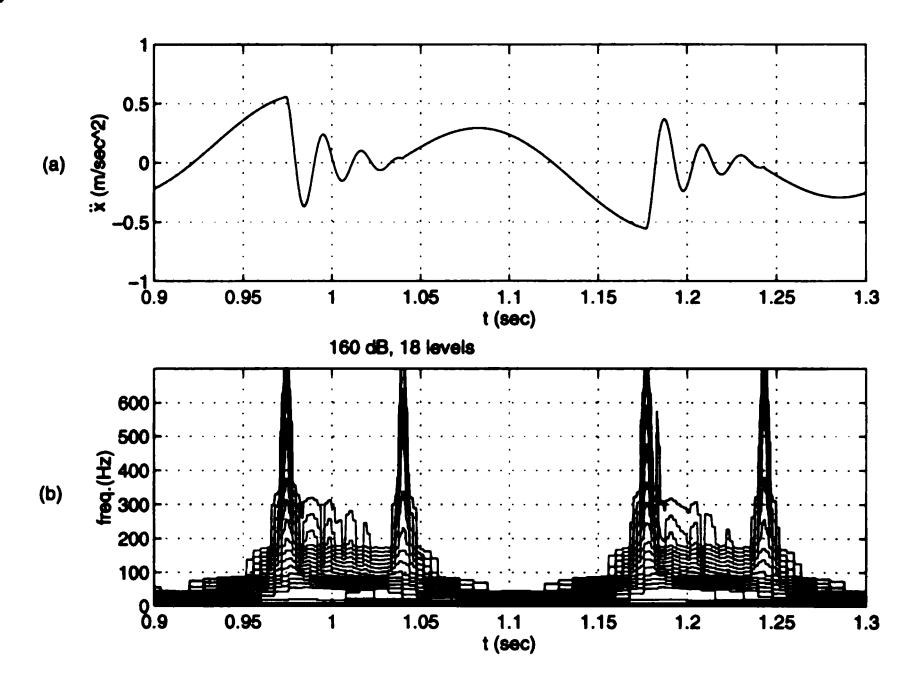


Figure 5.10: Detailed wavelet analysis of micro stick-slip event, tangential contact model, case 1: (a) time-domain response, and (b) wavelet contour plot.

Although we pointed out above that the grouped spike structures in Figures 5.9(b) and 5.8(b), especially in Figure 5.9(b), are resulted from the occurrences of micro slip events, the spikes in these plots actually did not point toward the exact locations of

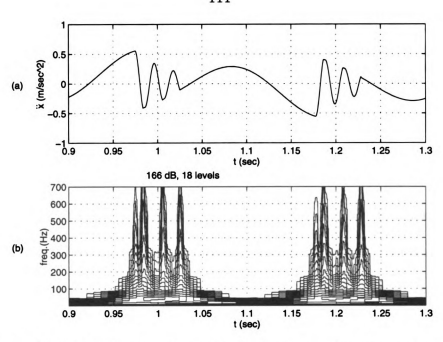


Figure 5.11: Detailed wavelet analysis of micro stick-slip event, tangential contact model, case 2: (a) time-domain response, and (b) wavelet contour plot.

micro slip events. This is due to the fact that a large threshold (or small span) and a low frequency range were used in Figure 5.9(b), which affect the representations of the small wavelet coefficients structure. If we reduce the threshold (increase the span between the maximum and minimum values of wavelet coefficients) and increase the investigated frequency range, the results corresponding to the simulations of tangential contact model, casel and case 2, can be obtained in Figures 5.10 and 5.11.

Recalling from the previous discussions, we know that the acceleration response of the tangential contact model, case 1 does not involve micro-slip event, whereas the case 2 has two short micro-slip durations during each macroscopic sticking interval.

These features are addressed in both Figures 5.10 and 5.11. They are particularly clear in the wavelet contour plots. For example, two large spikes exist during each

transition phase in Figure 5.10(b), representing the time-frequency properties of the macroscopic "sticking" and "sliding" events respectively. Between these two major spikes, there is not much high-frequency contour occurring which again dictates the sinusoidal characteristic of this transition oscillation.

Conversely, while the two spikes corresponding to the macroscopic sticking and sliding events are still observed, two more spikes occur during the sticking interval in Figure 5.11(b). These two extra spikes, occurring between the spikes caused by macroscopic motion features, point exactly to the locations at which the micro slip take place. This verifies that the micro slip event can introduce a spike structure in wavelet contour plot. Furthermore, the micro slip event is responsible for at least some of the spike structure appearing in Figure 5.9. The distortions occurred in Figure 5.9, so that spikes did not point toward the occurrences of micro slip events, were the results of the high threshold and the low investigated frequency range.

Thus, we have shown that the wavelet transition features of the experimental data are in accordance with those of the simulations of tangential contact model, case2. The consistencies include the local maximum contour structure, representing a nearly sinusoidal transition oscillation, and the grouped spike structure which demonstrate the micro stick-slip event. These observations are based on the qualitative comparisons. The presence of randomness in friction process makes the quantitative comparison to be difficult.

In the next section, we give a brief conclusion of this study.

5.4 Conclusions

In this investigation, the wavelet transform was used to explore time-frequency transition features of the numerical and experimental stick-slip signals. Evident wavelet features associated with various friction models were obtained and compared to a real stick-slip data. While many simulations can depict the transition oscillations, only the tangential contact model with light damping captures most of the characteristics of the experimental results. This was further verified by the comparisons between features of corresponding wavelet contours. Representations of the nearly sinusoidal transition oscillation and micro slip event illustrate the similarities of these two stick-slip data. Different wavelet features achieved from mathematical friction models can be applied as a tool for interpreting the real stick-slip behaviors.

CHAPTER 6

ESTIMATING COULOMB AND VISCOUS FRICTION FROM FREE-VIBRATION DECREMENTS

6.1 Introduction

One of the motivations of this thesis is the investigation of friction-induced noise, particularly the study of the automotive "squeak" problem. Squeak is a high-frequency frictional noise caused by unstable sliding motion. To study this problem, a quiet experimental environment is important. The air-track system which we introduced in previous chapters is no longer applicable due to the inherent acoustic noise caused by the air. This air noise is irreducible since some threshold air pressure is necessary for supporting the sliding mass. Hence, we will apply another anti-friction system in the squeak study. Among anti-friction systems, the linear-bearing system has been employed in many friction investigations (see for instance, Dweib and D'Souza [20], [18], Aronov et al. [6], [4], [5]). The linear-bearing system has both viscous damping and dry friction. In order to understand the damping characteristics of the linear-bearing system, an identification is conducted in this chapter.

Methods of estimating damping effects in mechanical systems have long existed. For example, in systems with viscous damping, the logarithmic decrement method is often applied to the displacement trace of a free-vibration test such that viscous damping can be estimated. The idea goes back to Hermann Helmhotz [27],

who used the logarithmic decrement to determine frequency information in musical tones. Rayleigh [62] formulated the idea using the term "logarithmic decrement". This method is accomplished by considering that amplitude decay in a free-vibration test, of a viscously damped system, is exponential in nature. In contrast, if Coulomb friction is the only damping present in the system, the decay of amplitudes tends to be linear. This property was found in Lorenz's work as early as 1924 [41]. Calculating the amplitude decrement for consecutive cycles gives an estimation of the dry-friction effect. The theoretical analysis of both estimation approaches can be found in a modern vibration textbook, e.g., Meirovitch [46]. An analytical prediction method for systems with both viscous and dry friction damping has not yet been seen. However, it is reasonable to presume that multiple damping parameters can be obtained from general nonlinear parametric identification schemes, such as Stry and Mook [72].

An algorithm for estimating viscous damping and dry friction in a combined-damping system is of importance because control applications often require complete information of a frictional system to implement a high-performance controller. Particularly, in the applications of model-referenced control schemes, accurate modeling is critical to the controller's performance [34]. Lack of information in different damping sources certainly increases the difficulty of modeling a frictional system.

This chapter continues the work of Feeny and Liang [24] in which a method for estimating viscous and dry-friction damping was proposed. More thorough investigations, including the application of the method to an industrial system and the analysis of the effects of measurement error on the estimations are included. The

method separates viscous damping from dry friction. Estimation of dry friction effect can then be obtained based on the estimated viscous damping. Systems with solely viscous damping or dry friction can be considered as a special case of this study.

The organization of this chapter is as follows. The next section addresses the solution to the free-vibration of a one-DOF system with dry friction. Decrement equations relating viscous damping to oscillation amplitudes can be derived for the combined-damping system. In Section 6.3, the validation of this approach is illustrated by some numerical studies. Section 6.4 verifies the proposed method experimentally by investigating a fundamental system which has a controllable friction source. It is followed by Section 6.5 in which an industrial system is examined. Damping characteristics of this system are completely unknown before the estimations were performed. Section 6.6 investigates the effects of different types of measurement errors on the estimation results. This chapter is concluded in Section 6.7.

6.2 Free Vibration with Coulomb and Viscous Damping

We consider a mechanical system modeled as a mass-spring-damper with dry friction (MKCF). By Newton's second law, the equation of motion can be written as

$$m\ddot{x} + c\dot{x} + kx + f(\dot{x}) = 0,$$
 (6.1)

where x denotes the displacement of the mass and spring from the unstretched equilibrium position, m, c, k represent the mass, viscous damping coefficient, and the spring stiffness. The dry friction is modeled as $f(\dot{x}) = f_k \text{sign}(\dot{x}), \dot{x} \neq 0$, and $-f_s \leq f(0) \leq f_s$. By assuming the existence of a coefficient of friction, such that $f(\dot{x}) = N\mu(\dot{x})$, where N is the normal load and μ is the coefficient of friction

consisting of a static coefficient, μ_s , and a kinetic coefficient of friction, μ_k , then this friction law corresponds to Coulomb's law. Nevertheless, we loosely refer to $f(\dot{x})$ as Coulomb friction.

The equilibrium solution of this equation of motion can be obtained by letting $\ddot{x} = \dot{x} = 0$. This gives rise to a locus of equilibria, i.e. $-x_s \le x \le x_s$, where $x_s = f_s/k$. Equation (6.1) is piecewise solvable and can be recast as

$$\ddot{x} + 2\zeta\omega_n\dot{x} + \omega_n^2 x = -\omega_n^2 x_k, \quad \dot{x} > 0, \tag{6.2}$$

and

$$\ddot{x} + 2\zeta\omega_n\dot{x} + \omega_n^2 x = +\omega_n^2 x_k \quad \dot{x} < 0, \tag{6.3}$$

where $\omega_n^2 = k/m$, $2\zeta\omega_n = c/m$, and $x_k = f_k/k$.

If we begin with initial conditions $x(t_0) = X_0 > x_s$ and $\dot{x}(t_0) = 0$, then motion starts with $\dot{x} < 0$. The response to equation (6.3) has the form

$$x(t) = (X_0 - x_k)e^{-\zeta \omega_n(t - t_0)}(\cos \omega_d(t - t_0) + \beta \sin \omega_d(t - t_0)) + x_k,$$
(6.4)

where $\omega_d = \omega_n \sqrt{1-\zeta^2}$ and $\beta = \zeta \sqrt{1-\zeta^2}$. This equation is valid until $\dot{x} = 0$ at which time $t = t_1 = t_0 + \pi/\omega_d$ and $X_1 = x(t_1) = -e^{-\beta \pi} X_0 + (e^{-\beta \pi} + 1) x_k$. If $X_1 < -x_s$, then the mass will reverse direction and continue sliding with $\dot{x} > 0$ according to equation (6.2). The solution for this interval of motion is

$$x(t) = (X_1 + x_k)e^{-\zeta \omega_n(t - t_1)}(\cos \omega_d(t - t_1) + \beta \sin \omega_d(t - t_1)) - x_k,$$
(6.5)

which is valid until $\dot{x}=0$, at which time $t=t_2=t_1+\pi/\omega_d$ and $X_2=x(t_2)=-e^{-\beta\pi}X_1-(e^{-\beta\pi}+1)x_k$. If $X_2>x_s$, motion will continue.

This process can be iterated until $-x_s \leq X_n \leq x_s$, at which time the motion stops. This iterated process leads to a recursive relation for the successive peaks and valleys in the oscillatory response:

$$X_{i} = -e^{-\beta\pi}X_{i-1} + (-1)^{i-1}(e^{-\beta\pi} + 1)x_{k}, \quad i = 1, 2, ..., n.$$
(6.6)

From this evolution of decaying peaks and valleys, we can isolate the viscous effect and then extract the Coulomb effect. A sum of consecutive extreme displacement values cancels out the dry-friction contribution. Taking the ratio between successive sums yields

$$\frac{X_i + X_{i+1}}{X_{i-1} + X_i} = -e^{-\beta\pi}. (6.7)$$

Thus, a logarithmic decrement reveals the viscous dependence:

$$\log(-\frac{X_i + X_{i+1}}{X_{i-1} + X_i}) = -\beta\pi. \tag{6.8}$$

Once the quantity β has been estimated, we can estimate ζ , and also the dry-friction parameter x_k from equation (6.6).

A fundamental problem in an experimental system is that, because of the locus of equilibria, it may be difficult to determine the position in which the spring is unstretched. Thus, measurement may have a constant bias with respect to our formulation. There is a simple way to deal with this. If the biased measurement is $y = x + \epsilon$, we remove the bias ϵ by subtracting two measured peaks (or valleys) Y_i . Since $Y_i - Y_j = X_i - X_j$, we can work with the difference between two recursive relations (6.6) such that

$$X_{i+1} - X_i = -e^{-\beta\pi} (X_i - X_{i-1}) + 2(-1)^i (e^{-\beta\pi} + 1) x_k,$$

$$i = 1, 2, ..., n - 1$$
(6.9)

By summing the equation for $X_{i+1} - X_i$ with that of $X_i - X_{i-1}$, we eliminate dry-friction contribution. An alternate decrement equation is thus

$$\frac{X_{i+1} - X_{i-1}}{X_i - X_{i-2}} = -e^{-\beta\pi},\tag{6.10}$$

or

$$\log(-\frac{X_{i+1} - X_{i-1}}{X_i - X_{i-2}}) = -\beta\pi.$$
(6.11)

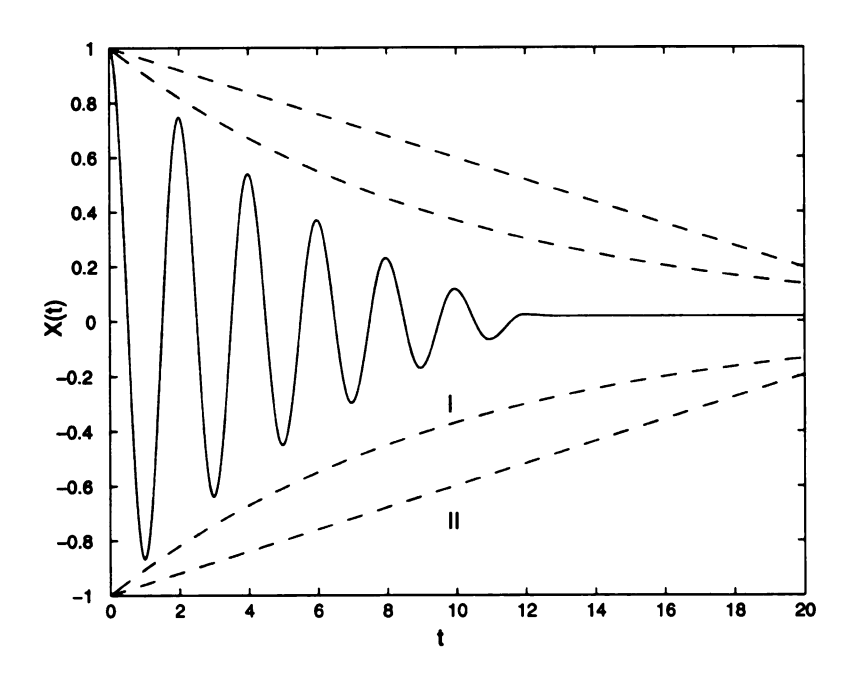


Figure 6.1: Simulated response of MKCF system, solid line: displacement response of MKCF system; dashed line I: amplitude envelopes of the purely viscous system; dashed line II: amplitude envelopes of the purely dry-friction system.

In what follows, we will apply this decrement idea numerically and experimentally to estimate both linear viscous-damping factor and the kinetic friction quantity $x_k = f_k/k$.

6.3 Numerical Solutions

This section illustrates numerical experiments for a MKCF system. The inte-

disp. peaks	X_0	X_1	X_2	X ₃
magnitude	1.00000	-0.86728	0.74711	-0.63832
disp. peaks	X_4	X_5	X_6	X_7
magnitude	0.53981	-0.45063	0.36989	-0.29678
disp. peaks	<i>X</i> ₈	<i>X</i> ₉	X ₁₀	X ₁₁
magnitude	0.23059	-0.17067	0.11641	-0.06729

Table 6.1: Extreme excursions in Figure 6.1

gration algorithm was a fifth order Runge-Kutta method. The discontinuity of dry friction was handled in the same way as in Shaw (1986) and Feeny and Moon (1994). The parameter values are m=1.0, k=10.0, c=0.2, and $f_k=0.2$. The initial conditions are x(0)=1.0 and $\dot{x}(0)=0$. The displacement response subjected to the initial condition for this MKCF system is shown in Figure 6.1. The response of this system resembles neither the purely viscous or dry-friction system. Furthermore, the amplitudes of this combined-damping system decay faster than the systems with a single form of damping.

In order to estimate the nondimensional viscous damping factor, ζ , and the dryfriction parameter, x_k , we measured the displacement peaks of the simulated response in Figure 6.1. These values are listed in Table 6.1.

From these data, the estimated viscous damping factor, $\hat{\zeta}$, can be obtained using equation (6.7). From

$$\frac{\Delta X_{10}}{\Delta X_0} = \frac{X_{10} + X_{11}}{X_0 + X_1} = e^{-10\hat{\beta}\pi},\tag{6.12}$$

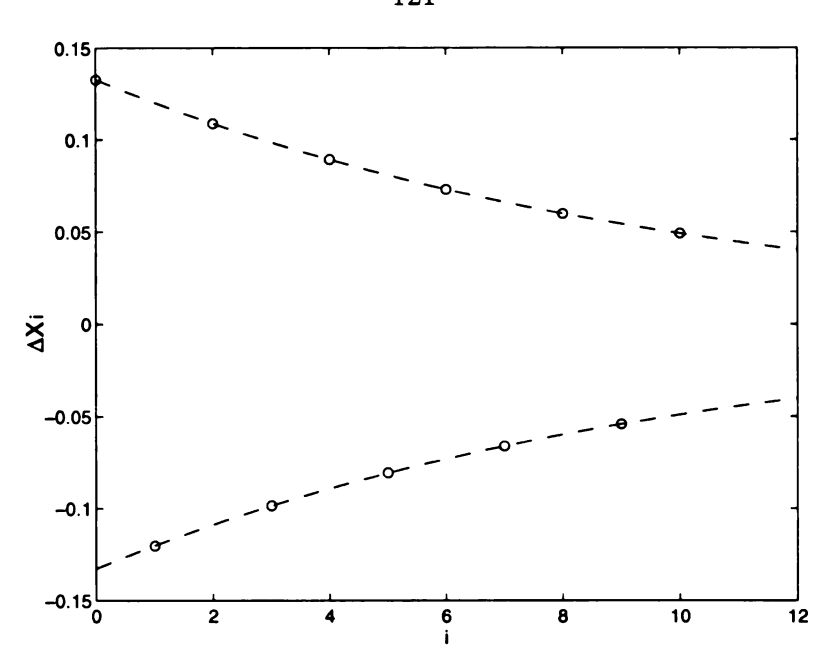
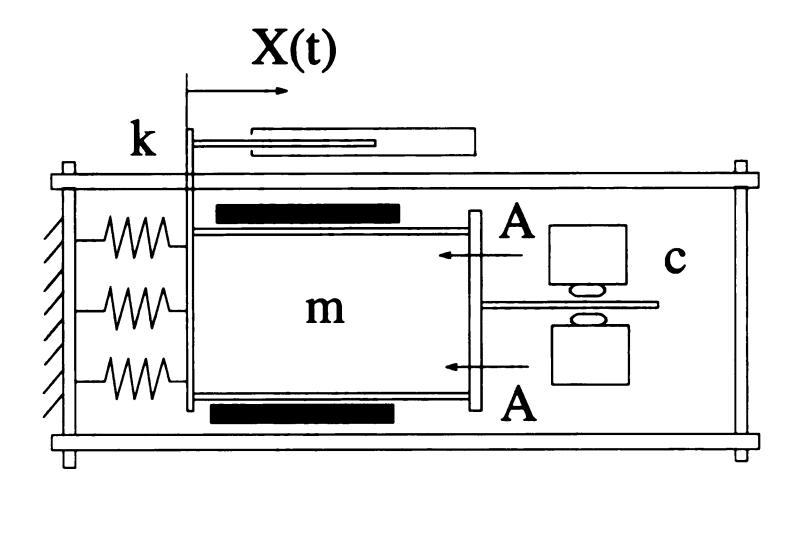
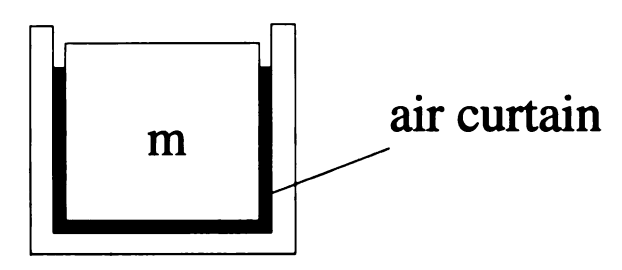


Figure 6.2: Exponential decay of amplitude difference in the simulated MKCF system, dashed lines: exponential envelopes; "o": amplitude differences ΔX_i .

we obtain, $\hat{\beta} = 0.0316$, and $\hat{\zeta} = 0.0316$. These values are consistent with the values calculated directly from system parameters m, k, and c. Estimation of dry-friction parameter, \hat{x}_k , can be accomplished by substituting the values of $\hat{\beta}$ and X_i into equation (6.6). The extracted \hat{x}_k is found to be 0.02, which is identical to the given values of f_k/k . Moreover, if one plots the amplitude differences, $\triangle X_i \equiv X_i + X_{i+1}$, versus index i, the result shows that amplitude differences decay exponentially as shown in Figure 6.2. This result dictates that two types of damping have been successfully separated. Figure 6.2 depicts the pure viscous-damping effect.

Thus, we have shown that this approach works well in a numerical experiment. How applicable will this method be in a real system? This will be answered by investigating two real systems. In what follows, system I has a source of dry friction that can be switched on and off, and the friction characteristic resembles the Coulomb





A-A sectional view

Figure 6.3: Schematic diagram of system I.

friction model. During the investigations of system I, the system configuration having only viscous damping will be termed the MKC system, whereas the configuration that contains only dry-friction effect will be called the MKF system. In contrast with system I, system II has the inherent damping with no modeling information known a priori. Its presence in the system cannot be controlled either.

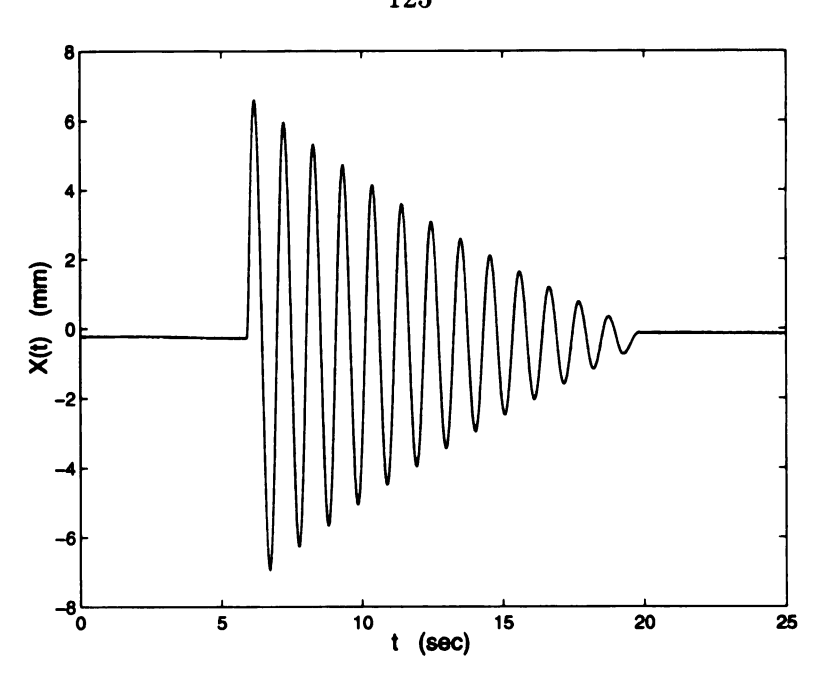


Figure 6.4: Experimental displacement response of system I (the MKF system), case 1.

6.4 Experiments on System I

6.4.1 Experiments on MKC and MKF Systems

Figure 6.3 illustrates a schematic diagram of system I which consists of mass, spring, damper and friction surfaces. The mass slides on a nearly frictionless air track. This air track has very small damping. A free-vibration test was conducted to determine the damping factor due to the air track and spring. The associated viscous damping factor was found to be 0.0008 based on logarithmic decrements with very little dry-friction effect.

An eddy-current viscous damper was used to provide additional viscous damping.

Coiled wires are used to produce a magnetic field, which interacts with a steel flange attached to the mass to provide damping. The dry friction was applied by packing

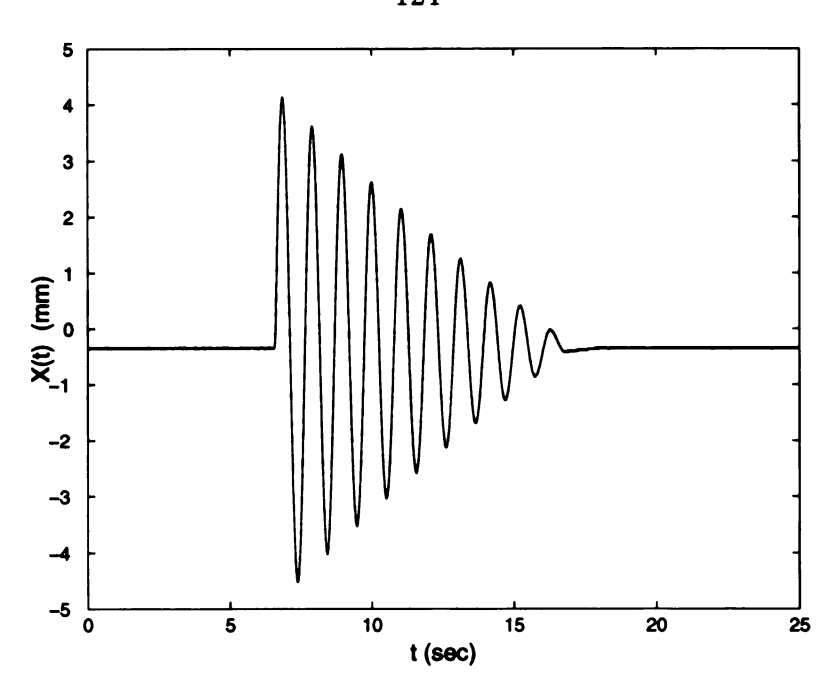


Figure 6.5: Experimental displacement response of system I (the MKF system), case 2.

paper between the electromagnets and the sliding mass. Therefore, the friction contact was paper-on-steel. The displacement response were sensed by linear variable differential transformer (LVDT) which had resolution of 0.01 mm after quantization step in the data-acquisition process.

In order to understand the dry friction properties, two free-vibration tests of MKF system were conducted. The displacement responses of these experiments are shown in Figures 6.4 and 6.5. These displacement traces decay nearly linearly, which suggests that the friction is nearly constant. The dry-friction forces, when converted into the equivalent displacements, are $x_{k1} = 0.1318$ mm and $x_{k2} = 0.1142$ mm respectively, where the subscripts "1" and "2" correspond to different testing conditions that will be addressed later. These values were calculated according to the linear-decay characteristic of dry friction, which basically states that the amplitudes decrease by " $4x_k$ " every cycle of oscillation (Meirovitch, 1986). In the computation of

Table 6.2: Estimations of MKCF systems (σ represents the standard deviation of each estimated and measured values)

	ζ1	σ	$\hat{\zeta}_1$	σ	error%
case 1	0.0276	0.0021	0.0269	0.0033	2.5%
	x_{k1}	σ	\hat{x}_{k1}	σ	error%
	0.1318 (mm)	0.0187 (mm)	0.1309 (mm)	0.0015 (mm)	0.7%
	ζ_2	σ	$\hat{\zeta}_2$	σ	error%
case 2	0.0631	0.0050	0.0632	0.0061	0.2%
	x_{k2}	σ	\hat{x}_{k2}	σ	error%
	0.1142 (mm)	0.0105 (mm)	0.1086 (mm)	0.0046 (mm)	4.9%

 x_k , we calculated x_{kj} (where the subscript "j" represents a calculation trial along the time-domain trace) based on every two consecutive amplitudes with the same sign. This calculation procedure goes through the whole trace. Thus, several calculated x_{kj} were obtained to achieve a mean value, x_k , and a standard deviation σ which are listed in Table 6.2. The dry-friction parameters, x_{k1} and x_{k2} measured in this section will be used as reference values to be compared to values estimated from combined-damping systems that have same system configurations with additional viscous damping effects. Estimations obtained from the combined-damping systems will be denoted as \hat{x}_{k1} and \hat{x}_{k2} in the next section.

Next, we consider the MKC systems. There are two testing conditions, which correspond to different degrees of viscous damping and are called "case 1" and "case 2". Initial conditions were applied by displacing the sliding mass to stretched positions prior to release. Displacement responses of these two viscously damped systems

are presented in Figures 6.6 and 6.7. Also presented in these figures are the exponential decay envelopes. These envelopes are generated according to the estimated damping factors as well as the initial conditions. The damping factors corresponding to these systems are obtained by applying the logarithmic decrement method to the experimental data in Figures 6.6 and 6.7. The computation process is the same as that in the dry-friction case. Thus, there are several calculated ζ_j for each case and the mean value and standard deviation are listed in Table 6.2.

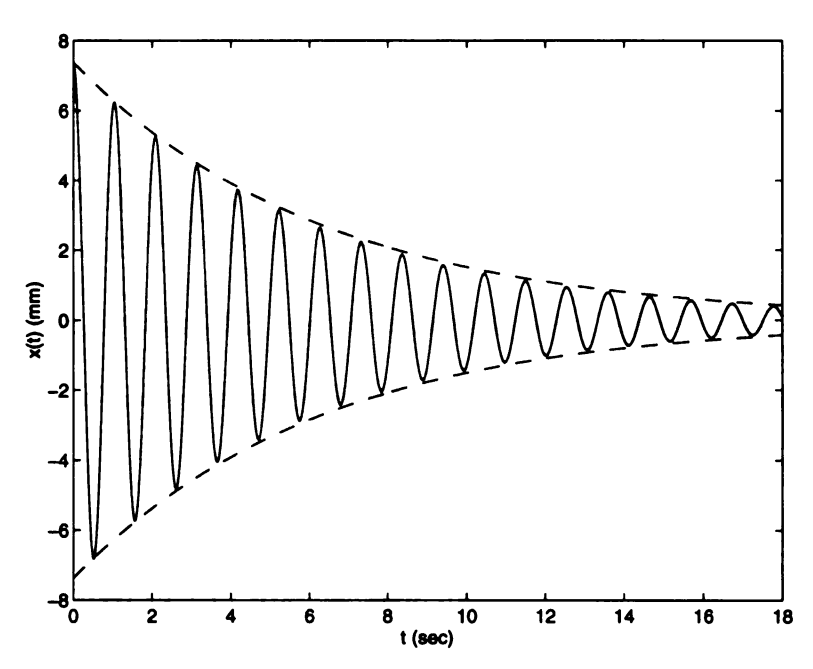


Figure 6.6: Experimental displacement response of system I (the MKC system), case 1.

Figures 6.6 and 6.7 indicate that both systems are damped quite viscously in the sense that envelopes match the decay amplitudes very well. The corresponding damping factors for these two tests are $\zeta_1 = 0.0276$ and $\zeta_2 = 0.0631$. Based on the agreements between experimental responses and decay envelopes, these damping factors will be used as reference values for evaluating results from combined-damping systems.

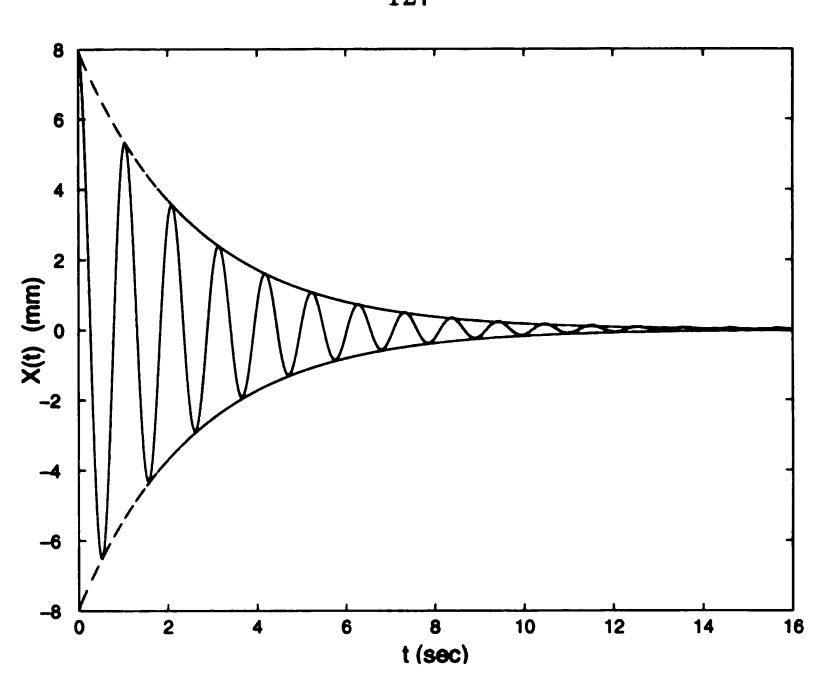


Figure 6.7: Experimental displacement response of system I (the MKC system), case 2.

In the following section, this method is applied to the MKCF system. The MKCF systems have "combined damping effects" which individually correspond to the cases addressed above.

6.4.2 Identification of the MKCF Systems

Figure 6.8 presents the displacement response for the MKCF system of case 1 subjected to initial displacement disturbance. The estimations of nondimensional damping factor, $\hat{\zeta}_1$, and dry-friction parameter, \hat{x}_{k1} , are listed in Table 6.2. In obtaining these estimations, we calculated $\hat{\zeta}$ from every four consecutive extreme excursions and equation (6.10) so that different estimations were obtained through the whole time-domain trace. Then, the mean value and standard deviation were computed and listed in Table 6.2. Once $\hat{\zeta}$ was determined, a similar procedure was

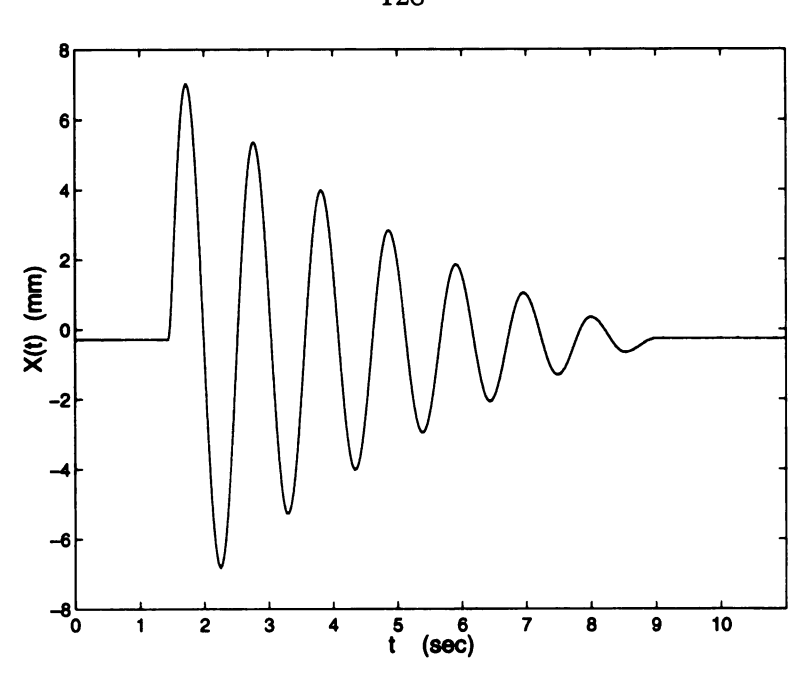


Figure 6.8: Experiment displacement response of system I (the MKCF system), case 1.

adopted for the estimation of dry-friction from equation (6.9). The estimation errors, based on reference values from previous section, are 2.5% and 0.7% respectively. The accuracy of the damping factor estimation can be judged from Figure 6.9 in which the amplitude differences are compared to the exponential decay envelopes. This plot is based on equation (6.10) and the measured amplitudes in Figure 6.8. Since equation (6.10) describes the viscous-damping effect, deviations between amplitude differences (ΔX_i) and exponentially decaying envelopes can be treated as performance index of system's viscous behavior.

In contrast, the larger deviation of the dry-friction estimation may be attributed to the uncertainty associated with friction modeling or any measurement error.

Next, we consider case 2, which has higher viscous damping effect. Figures 6.10 and 6.11 show the displacement response and amplitude decay for this case. The estimations for different parameters are listed in Table 6.2. Observations similar to

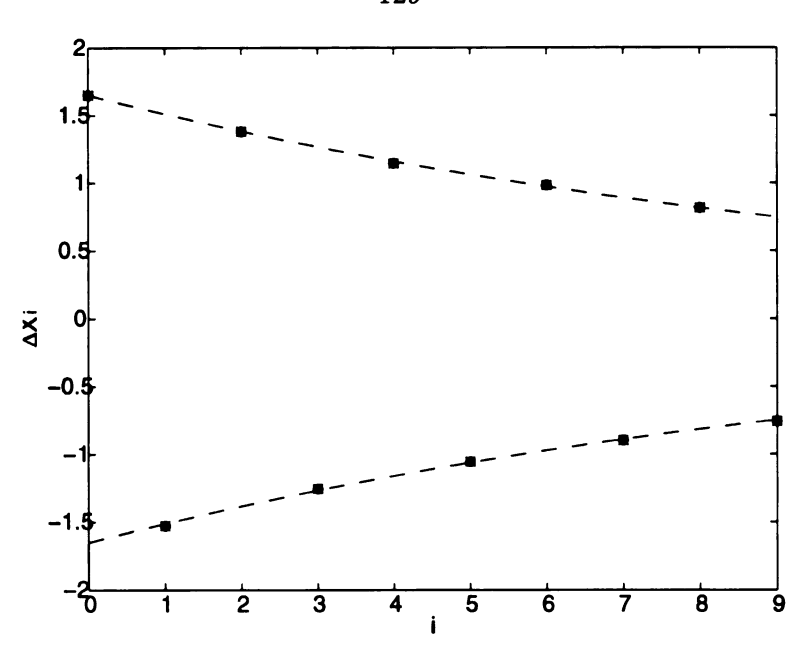


Figure 6.9: Experiment results showing the exponential decay of amplitude differences, system I (the MKCF system), case 1.

case 1 can be obtained from Table 6.2 and Figures 6.10 and 6.11. These include better accuracy in the damping-factor estimation, consistent exponential decay of amplitude differences, and lower accuracy in the estimation of dry friction. In order to further evaluate the estimations made on this case, we numerically integrated the system equation of motion with the estimated parameters and initial conditions. Figure 6.10 demonstrates the comparison between experimental and numerical time-domain responses. It is evident that estimations from the proposed method are able to catch most of the response features.

Although the estimation of the friction force may not be highly accurate, the proposed approach is very efficient in separating individual damping effects from a combined-damping system. This may be attributed to the ability of isolating the friction source. In many industrial systems, this is almost impossible. The following section gives a case study for a typical industrial system in which the

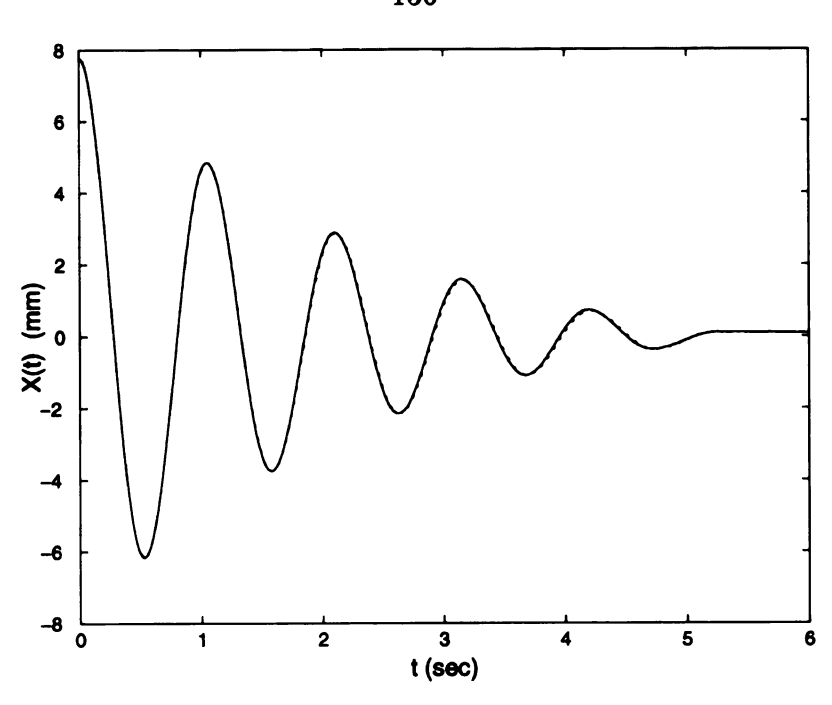


Figure 6.10: Experimental displacement response of system I (the MKCF system), case 2. Comparison between experimental and identified results (solid line: experimental result; dotted line: identified result).

friction characteristics are unknown.

6.5 Experimental System II: A Linear-Bearing System

This section investigates a system with unknown viscous and dry damping coefficients. The system consists of two linear bearings with very low viscous and dry friction effects. The linear bearings were made by Thomson Industries, Inc. (Model, 1CC-08-HAA). In order to compare the estimated results to the data provided by the linear bearing company, the seals at both ends of the linear bearings were removed. A sliding table mounted on the top of linear bearings is connected by three helical springs. The schematic diagram is shown in Figure 6.12. Linear bearings are widely used in high-speed position control systems. It is important to quantify the friction

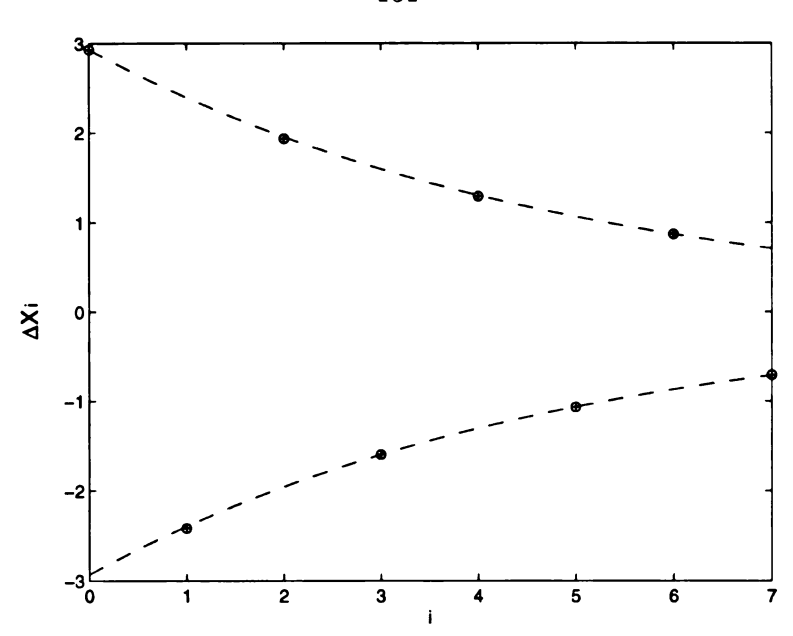


Figure 6.11: Experiment results showing the exponential decay of amplitude differences, system I (the MKCF system), case 2.

contribution to provide modeling information for control engineers.

To investigate damping characteristics of this system, initial conditions were applied to conduct a free-vibration test. Figures 6.13 and 6.14 show the displacement response and the decay trend of amplitude differences respectively. The estimations of system parameters are $\hat{\beta}_3 = 0.0177$, $\hat{\zeta}_3 = 0.0177$ ($\sigma = 0.0164$), and $\hat{f}_k = 0.413$ N ($\sigma = 0.0249$ N).

Figure 6.14 suggests that the system has low viscous damping because the envelopes bend slightly and the deviations of amplitude differences from two envelopes are quite small. To check the validity of our model, we numerically simulated the system response by applying the estimated parameters. The mass and stiffness were determined: m = 1.92 kg and k = 2310 N/m. These parameters were incorporated with the estimated damping information for accomplishing the numerical simulation. The initial conditions in simulation were identical to those of experimental

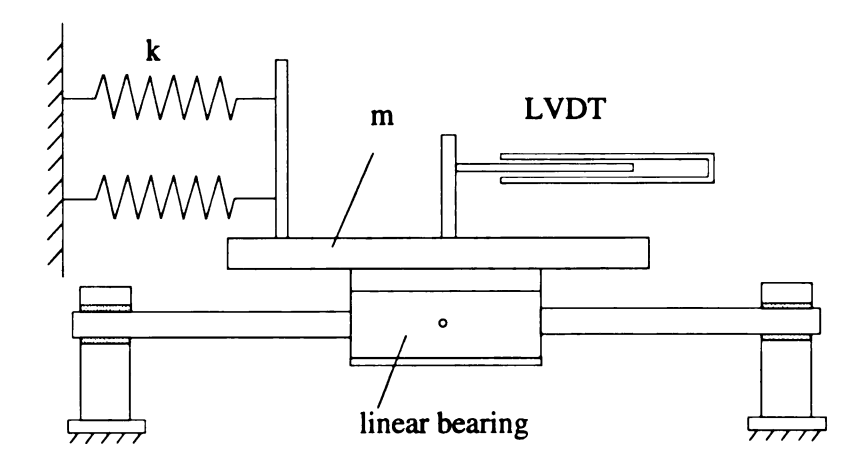


Figure 6.12: A schematic diagram showing the experimental setup of system II.

study. The comparison between numerical and experimental displacement responses is presented in Figure 6.15. Figure 6.15 shows that the numerical result catches most of the features of the experimental data. Based on the recovered system parameters, the modeling of this industrial system is feasible. To compare the estimated damping information with those provided by linear bearing company, we divided the estimated friction force by the weight of sliding table. The coefficient of sliding friction was found to be 0.022, which is about 10 times greater than the value provided by the company. The reason for this discrepancy calls for further investigation.

In the next section, an analysis of the effects caused by measurement error on the estimation is included.

6.6 Error Analysis

The experimental implementation of this proposed method involves measurements of the oscillation amplitudes. The reliability of the estimation depends on the accuracy of the measurements. According to sampling theorem, digital errors

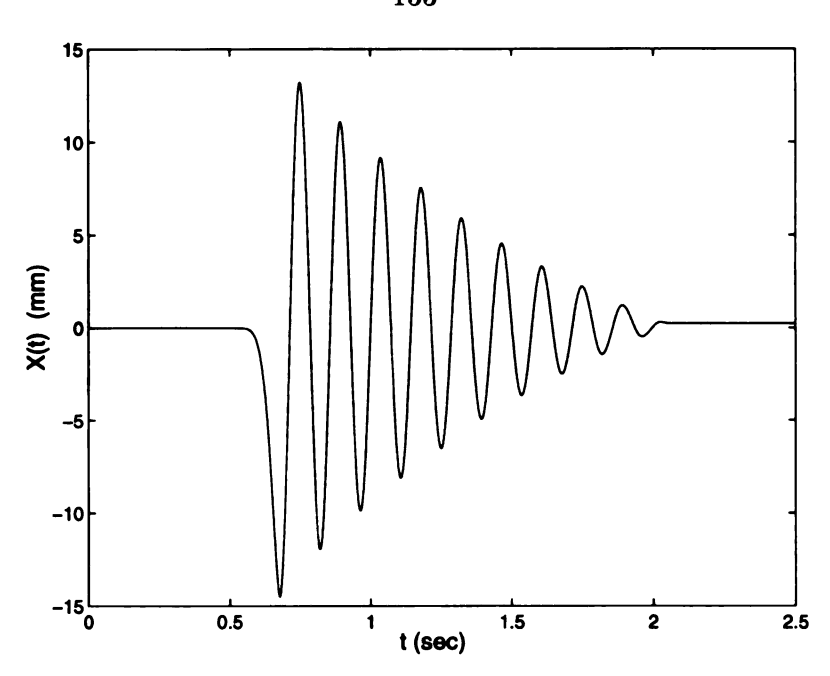


Figure 6.13: Experimental displacement response of system II.

during data acquisition process are inevitable. These include the quantization error and error due to the sampling process in which the first one is caused by the discretization of signal's magnitude and the latter one is by the discretization of time. There might be other sources of error involved in experiment including the random error that caused by manual reading process from readout device and the noise on the transducers' responses. It is of interest to understand how measurement errors affect the estimation accuracy.

6.6.1 Bounds on Estimation Errors

If the measured amplitudes are represented by \bar{X}_i , i=1,2,...,n, then $X_i=\bar{X}_i+\delta_i$, i=1,2,...,n, where δ_i is the error associated with different amplitude measurements and X_i represents the real or physical amplitudes. We assume that δ_i contains different types of errors including digital error, random error, and trans-

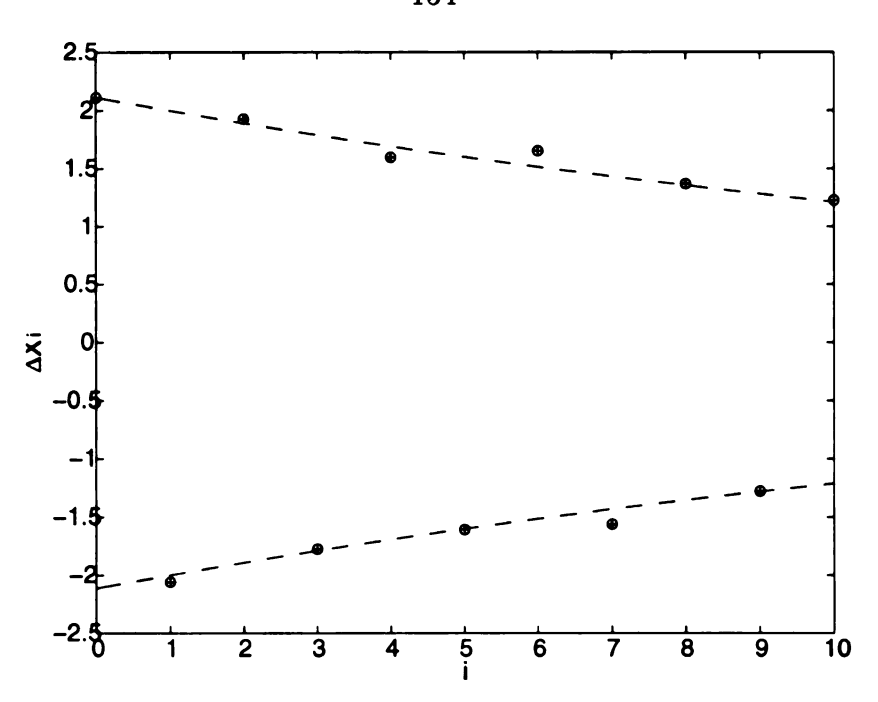


Figure 6.14: Experiment results showing the exponential decay of amplitude differences, system II.

ducer noise etc. Equations (6.10) and (6.11) are the crux of the proposed decrement method for experimental systems. In order to study the effects of measurement error, we extend the idea of equation (6.10) into

$$\frac{X_{i+m+1} - X_{i+m-1}}{X_{i+1} - X_{i-1}} = (-1)^m e^{-\beta m\pi} \quad i = 1, 2, ..., n,$$
and $m = 1, 2, ..., n - i - 1,$ (6.13)

where "m" represents the number of extreme excursions accumulated for the estimation process. If the estimated nondimensional viscous-damping parameter $\bar{\beta}$ (note in previous sections this magnitude was called $\hat{\beta}$) were calculated from equation (6.13) using the measured amplitudes \bar{X}_i , then

$$\frac{\bar{X}_{i+m+1} - \bar{X}_{i+m-1}}{\bar{X}_{i+1} - \bar{X}_{i-1}} = (-1)^m e^{-\bar{\beta}m\pi}$$
(6.14)

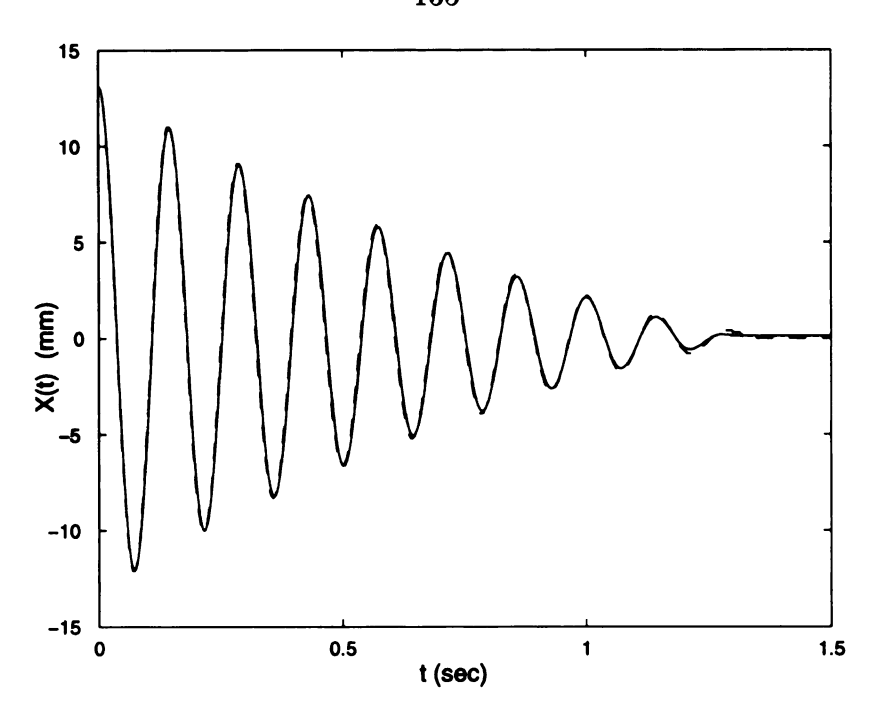


Figure 6.15: Comparison between experimental and identified displacement responses of system II (solid line: experimental result; dashed line: identified result).

We relate the estimated and real damping parameters such that $\beta = \bar{\beta} + \delta \beta$, where $\delta \beta$ represents the estimation error.

It is of importance to understand how the magnitude of estimation error in viscous-damping parameter, $|\delta\beta|$, depends on the measurement error. Therefore, equations (6.13) and (6.14), and expressions $X_i = \bar{X}_i + \delta_i$, and $\beta = \bar{\beta} + \delta\beta$ must be considered. If we expand equation (6.13) into a Taylor series and consider only the first-order terms, the following equation can be achieved:

$$\delta_{i+m+1} - \delta_{i+m-1} = m\pi (-1)^{m+1} e^{-\bar{\beta}m\pi} (\bar{X}_{i+1} - \bar{X}_{i-1}) \delta\beta + (-1)^m e^{-\bar{\beta}m\pi} (\delta_{i+1} - \delta_{i-1}), \tag{6.15}$$

where δ_{i+m+1} , δ_{i+m-1} , δ_{i-1} , δ_{i+1} are measurement errors associated with different amplitudes. We next assume that there exists an upper bound " δ " which confines all

the deviations in amplitude measurements, namely $\delta_j \leq \delta \ \forall j = 1, 2, ..., n$ and $\delta > 0$. Based on this assumption and taking the bounds of both sides of equation (6.15), an expression which relates the magnitude of estimation error $|\delta\beta|$ to the upper bound of measurement error δ can be obtained as follows:

$$|\delta\beta| \le \frac{2(1 + e^{-\bar{\beta}m\pi})\delta}{m\pi e^{-\bar{\beta}m\pi}|\bar{X}_{i+1} - \bar{X}_{i-1}|} = \alpha.$$
 (6.16)

This expression suggests that the bound of the estimation error, α , is directly proportional to the bound of the measurement error δ , and α can be minimized by a clever choice of m. For example, if β is small, the optimal choice of m will be large. Additionally, to increase $|\bar{X}_{i+1} - \bar{X}_{i-1}|$ so as to reduce α , the first couple cycles of a free-vibration response is recommended because larger amplitude difference with the same sign can be achieved.

We proceed to investigate the estimation of the dry-friction effect. In order to investigate this issue, equation (6.9) is of concern. As with the study of the viscous-damping estimation, the Coulomb friction parameter can be written as $x_k = \bar{x}_k + \delta x_k$. Moreover, suppose equation (6.9) is expressed in a Taylor series, the following equation can be obtained after neglecting the high-order terms:

$$\delta_{i+1} - \delta_i = \pi e^{-\bar{\beta}\pi} (\bar{X}_i - \bar{X}_{i-1}) \delta\beta - e^{-\bar{\beta}\pi} (\delta_i - \delta_{i-1})$$

$$+2(-1)^{i+1} (\pi e^{-\bar{\beta}\pi}) \bar{x}_k \delta\beta + 2(-1)^i (1 + e^{-\bar{\beta}\pi}) \delta x_k$$
(6.17)

Rearranging and taking bounds in the above equation yields

$$|\delta x_k| \le \frac{\pi e^{-\bar{\beta}\pi} (|\bar{X}_i - \bar{X}_{i-1}| + 2\bar{x}_k)}{2(1 + e^{-\bar{\beta}\pi})} |\delta\beta| + \delta = \psi$$
 (6.18)

Applying the bound of the error on β derived for general value of m (inequal-

ity (6.16)) to the above equation, and taking m = 1, leads to

$$|\delta x_k| \le \{1 + \frac{|\bar{X}_i - \bar{X}_{i-1}| + 2\bar{x}_k}{|\bar{X}_{i+1} - \bar{X}_{i-1}|}\}\delta = \gamma \tag{6.19}$$

The first inequality above relates magnitude of the estimation error in dry-friction effect, namely $|\delta x_k|$, to different quantities including the bound of measurement error, δ , magnitude of the estimation error in viscous-damping effect, $|\delta\beta|$, magnitude of measured dry-friction effect, \bar{x}_k , and the span between a consecutive peak and valley, $|\bar{X}_i - \bar{X}_{i-1}|$. The bound on $|\delta x_k|$, ψ , is proportional to $|\delta\beta|$ and δ , and nonlinearly dependent on $\bar{\beta}$. Given $\bar{\beta}$ and \bar{x}_k , ψ decreases if values of δ , $|\delta\beta|$, or $|\bar{X}_i - \bar{X}_{i-1}|$ are small. To reduce δ , a high-precision quantization machine with fast sampling rate and a noise-free experimental environment are required. Procedures of making $|\delta\beta|$ small have been discussed. To achieve small magnitude of $|\bar{X}_i - \bar{X}_{i-1}|$, the amplitudes of the last couple oscillatory cycles are recommended.

In contrast, inequality (6.19) suggests that for given δ and \bar{x}_k , if β were estimated according to four consecutive extreme excursions, γ decreases when β increases. This is true because the quantity $|\bar{X}_{i+1} - \bar{X}_{i-1}|$, representing the amplitude difference between two consecutive peaks (or valleys) and appearing in the denominator of equation (6.19), increases as β increases. Similarly, the magnitude $|\bar{X}_i - \bar{X}_{i-1}|$, corresponding to a span between peak and valley in one cycle, decreases as the viscous damping increases, which will reduce γ as well.

Thus, we have shown that bounds on $|\delta\beta|$ and $|\delta x_k|$ depend directly on the measurement error δ . If the viscous damping is small, a cumulative selection of amplitudes reduces the error bound of viscous-damping estimation. In addition, the error bound of the dry-friction estimation, ψ , depends on the estimation error of the vis-

Table 6.3: Extreme excursions in Figure 6.16 ($\delta = 0.005$)

disp. peaks	$ar{X}_0$	δ_0	$ar{X}_1$	δ_1	$ar{X}_2$	δ_2	$ar{X}_3$	δ_3
magnitude	1.0023	-0.0023	-0.8723	0.0050	0.7513	-0.0042	-0.6417	0.0034
disp. peaks	$ar{X}_4$	δ_4	$ar{X}_5$	δ_5	$ar{X}_6$	δ_6	$ar{X}_{7}$	δ_7
magnitude	0.5436	-0.0038	-0.4551	0.0045	0.3743	-0.0044	-0.3012	0.0044
disp. peaks	$ar{X}_{8}$	δ_8	$ar{X}_{9}$	δ_9	$ar{X}_{10}$	δ_{10}	$ar{X}_{11}$	δ_{11}
magnitude	0.2351	-0.0045	-0.1752	0.0045	0.1213	-0.0049	-0.0721	0.0048

cous damping. Inequality (6.19) shows that smaller γ can be achieved if the viscous damping is large and is estimated from four consecutive extreme excursions.

The following section gives some numerical examples which describe the relationships between different types of measurement errors and estimation results.

6.6.2 Numerical Examples

In this section, we perform several numerical experiments. We will treat the simulation data shown in Figure 6.1 as a perfect case, namely the free-vibration response is treated as the real response (without any type of error). First, a random signal with a known bound, δ , will be superimposed on this perfect signal to simulate the possible random type of error occurring in the experimental process. The signal with noise is shown in Figure 6.16 where the bound of measurement error is taken as $\delta = 0.005$ which is equal to the bound of random numbers superimposed on the pure simulation data shown in Figure 6.1.

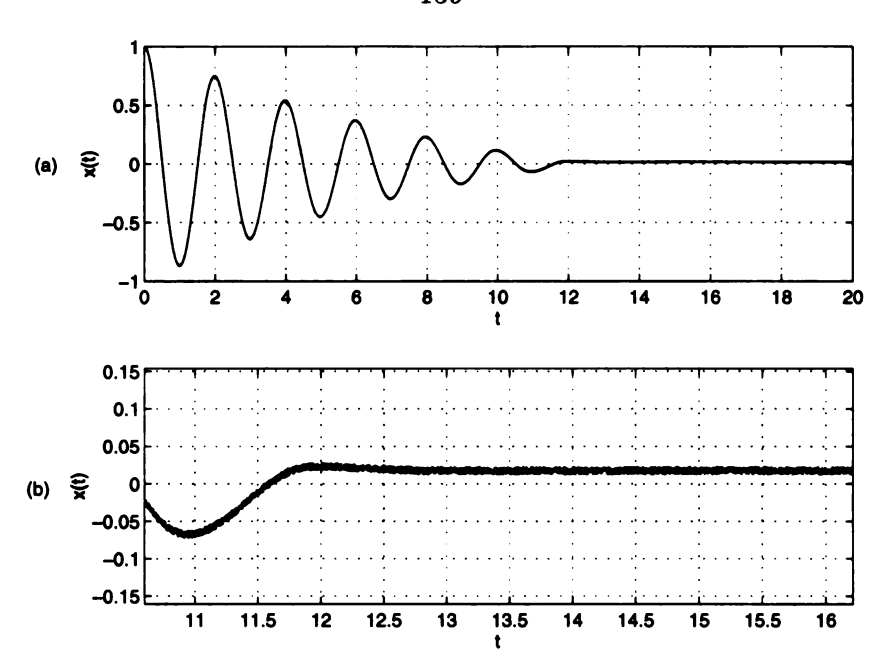


Figure 6.16: Simulation of effects of random error: (a) displacement response and (b) zoom-in detail of random error

From Section 6.3, we realize that the real viscous-damping parameter β can be assumed to be "0.0316" and the real dry friction parameter x_k is "0.02". Next, we calculate the estimated values of $\bar{\beta}$ in accordance with the measured amplitudes listed in Table 6.3. Including in the same table are the measurement errors associated with different extreme excursions, namely δ_i . If we choose i=2, estimations of the viscous-damping effect can be calculated, using equation (6.14), as

•
$$m = 1$$

$$\bar{\beta}_1 = \frac{-1}{\pi} \log \frac{-(\bar{X}_4 - \bar{X}_2)}{(\bar{X}_3 - \bar{X}_1)} = 0.0333 \tag{6.20}$$

•
$$m = 3$$

$$\bar{\beta}_3 = \frac{-1}{3\pi} \log \frac{-(\bar{X}_6 - \bar{X}_4)}{(\bar{X}_3 - \bar{X}_1)} = 0.0328 \tag{6.21}$$

Table 6.4: Estimation errors and bounds for the case of random error ($\delta = 0.005$)

	m	$ar{oldsymbol{eta}}$	$ \deltaoldsymbol{eta} $	$ \deltaeta /eta(\%)$	α
β	1	0.0333	0.0017	5.3	0.0291
(0.0316)	3	0.0328	0.0012	3.8	0.0109
	5	0.0321	0.0005	1.6	0.0073
	7	0.0321	0.0005	1.6	0.0060
d					
	m	\bar{x}_k	δx_k	$ \delta x_k /x_k(\%)$	ψ
x_k	m 1	\bar{x}_k 0.0182	δx_k 0.0018	$\frac{ \delta x_k /x_k(\%)}{9.0}$	ψ 0.0070
x_k (0.02)	<u> </u>				
	1	0.0182	0.0018	9.0	0.0070

•
$$m = 5$$

$$\bar{\beta}_5 = \frac{-1}{5\pi} \log \frac{-(\bar{X}_8 - \bar{X}_6)}{(\bar{X}_3 - \bar{X}_1)} = 0.0321 \tag{6.22}$$

The values of m shown above represent the number of extreme excursions accumulated for the estimation process. From equations (6.20)-(6.22) and the known β value, estimation errors $|\delta\beta|$ for different cases can be obtained. Furthermore, the bound of the viscous-damping estimation, α , can be computed from equation (6.16). Results including the estimation error $|\delta\beta|$ and its bound α for different m values are listed in Table 6.4.

We then proceed to estimate the dry-friction parameter x_k . The calculation of \bar{x}_k follows equation (6.9). The following illustrates a typical calculation

•
$$m = 1$$

$$\bar{x}_{k1} = \frac{\left[(\bar{X}_3 - \bar{X}_2) + e^{-0.0333\pi} (\bar{X}_2 - \bar{X}_1) \right]}{2(1 + e^{-0.0333\pi})} = 0.0182$$
 (6.23)

Similarly, if values of $\bar{\beta}$ corresponding to different m were substituted into the above equation, the other estimations of x_k can be achieved. Conversely, the bound of the estimation error in dry friction can follow inequality (6.18) or (6.19), depending on the value of m. Here, we compute bounds using inequality (6.18). Estimation results of dry friction are also listed in Table 6.4.

According to Table 6.4, estimations of viscous damping are more accurate compared to those of dry friction. Moreover, despite the fact that the bounds on both viscous-damping and dry-friction estimation errors are conservative, they indeed confine the actual estimation errors. This shows the reliability of error analysis performed in the previous section. The source of random error can either be the noise problem associated with transducer/environment or results from the manual reading process of readout device.

Another example, illustrating the effect of measurement error induced by quantization, is given next. Quantization is unavoidable in digital data acquisition process, and can give rise to measurement error due to the resolution problem. The upper bound of measurement error in this example is 0.001 which equals to the quantization step size. The signal with this lower quantization resolution (compared to Figure 6.1) is shown in Figure 6.17. Based on this figure, different amplitude measurements were taken and listed in Table 6.5. Calculations can then be carried out and the results are shown in Table 6.6. Some observations are made from Table 6.6. These include: (1) The bound of viscous-damping error (α) decreases as m increases,

which follows the results of equation (6.16). Furthermore, the magnitudes of α are smaller compared to the previous case since the upper bound δ is smaller in this case. (2) Although the bound of viscous-damping decreases when the value of m increases, the actual error $|\delta\beta|$ does not follow the same trend. This is due to the fact that equation (6.16) addresses nothing about the actual estimation error. More specially, the actual estimation is affected by the effect of different types of errors on the individual amplitudes. (3) The estimation errors of dry friction are less accurate compared to those of viscous damping, and the bound ψ depends on the actual estimation error of viscous damping. This agrees with equation (6.18).

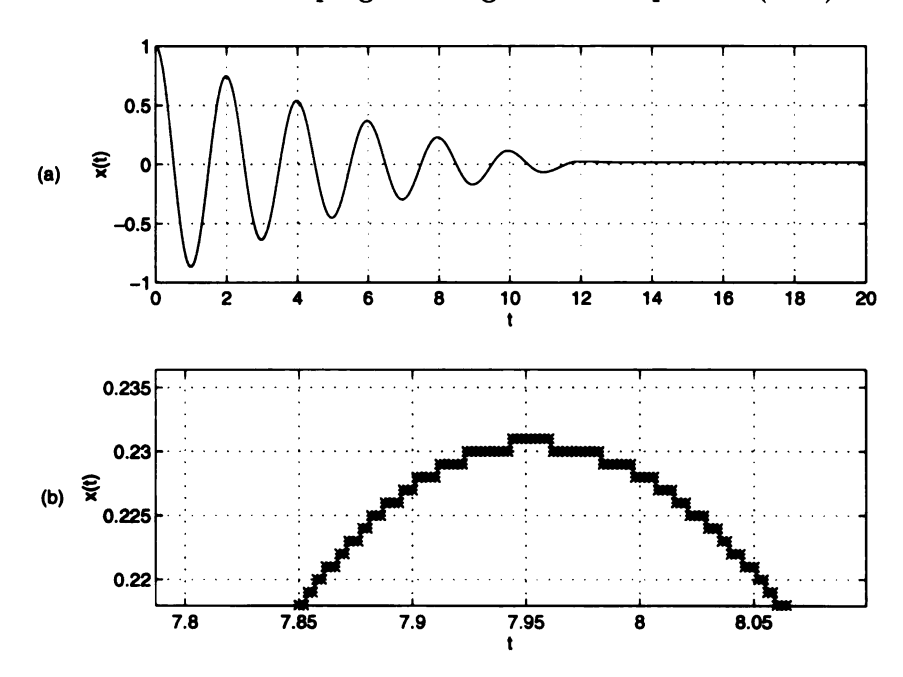


Figure 6.17: Simulation of effects of quantization error: (a) displacement response and (b) zoom-in detail of quantization error.

Finally, we show the measurement error caused by the sampling process. This type of error occurs because of the discretization in time. Showing in Figure 6.18 is a numerical data having a more sparse sampling interval. The upper bound of

Table 6.5: Extreme excursions in Figure 6.17 ($\delta = 0.001$)

disp. peaks	$ar{X}_0$	δ_0	$ar{X}_1$	δ_1	$ar{X}_2$	δ_2	$ar{X}_3$	δ_3
magnitude	1.0	0.0000	-0.8670	-0.0003	0.7470	0.0001	-0.6380	-0.0003
disp. peaks	$ar{X}_4$	δ_4	$ar{X}_5$	δ_5	$ar{X}_6$	δ_6	$ar{X}_{7}$	δ_7
magnitude	0.5400	-0.0002	-0.4510	0.0004	0.3700	-0.0001	-0.2970	0.0002
disp. peaks	$ar{X}_8$	δ_8	$ar{X}_{9}$	δ_9	$ar{X}_{10}$	δ_{10}	$ ilde{X}_{11}$	δ_{11}
magnitude	0.2310	-0.0004	-0.1710	0.0003	0.1160	0.0004	-0.0670	-0.0003

Table 6.6: Estimation errors and bounds for the case of quantization error ($\delta = 0.001$)

	m	$ar{oldsymbol{eta}}$	$ \deltaoldsymbol{eta} $	$ \deltaeta /eta(\%)$	α
β	1	0.0322	0.00055	1.74	0.0059
(0.0316)	3	0.0316	0.00001	0.03	0.0022
	5	0.0318	0.00018	0.58	0.0015
	7	0.0313	0.00028	0.88	0.0012
	m	$ar{x}_{m{k}}$	$ \delta x_k $	$ \delta x_k /x_k(\%)$	ψ
x_k	1	\bar{x}_k 0.0194	$\frac{ \delta x_k }{0.00058}$	$\frac{ \delta x_k /x_k(\%)}{2.91}$	$oldsymbol{\psi}$ 0.0017
x_k (0.02)			 		
	1	0.0194	0.00058	2.91	0.0017

this case was determined to be 0.0038 which is the maximum of the measurement errors associated with different amplitudes. Same procedure was used to calculate various estimations, their corresponding error magnitudes, and the error bounds. The results are presented in Table 6.8, whereas Table 6.7 gives the measurements of the displacement extrema. In accordance with Table 6.8, observations similar to the quantization case can be obtained.

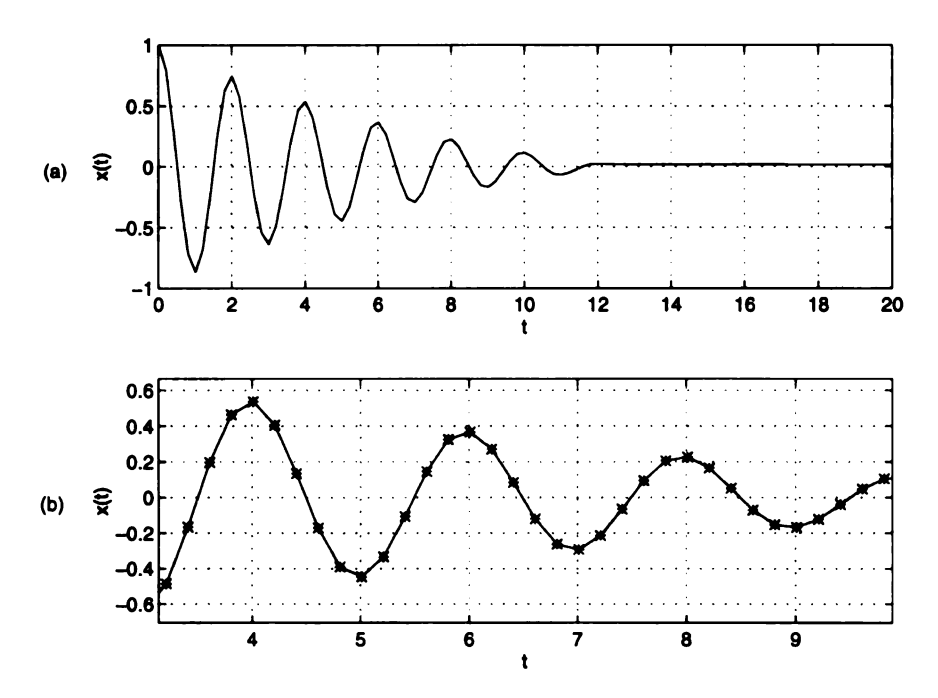


Figure 6.18: Simulation of effects of error of sampling process: (a) displacement response and (b) zoom-in detail of sampling error

To this end, we have shown that the error analysis carried out in the previous section indeed provides bounds on the estimation errors. While the actual error may not have a certain pattern subjected to different types of error, the bound confines all of the estimation errors. Numerical examples show that the bound seems to be conservative. However, it becomes less conservative when the effective bound on the measurements of extreme excursion, $2\delta_{eff}$, (instead of the upper bound 2δ shown in

Table 6.7: Extreme excursions in Figure 6.18 ($\delta = 0.0038$)

disp. peaks	$ar{X}_0$	δ_0	$ar{X}_1$	δ_1	$ar{X_2}$	δ_2	$ar{X}_3$	δ_3
magnitude	1.0	0.0000	-0.8662	-0.0011	0.7453	0.0018	-0.6359	-0.0024
disp. peaks	$ar{X}_4$	δ_4	$ar{X}_5$	δ_5	$ar{X}_6$	δ_6	$ar{X}_7$	δ_7
magnitude	0.5368	0.0030	-0.4472	-0.0034	0.3662	0.0037	-0.2930	-0.0038
disp. peaks	$ar{X}_8$	δ_8	$ar{X}_9$	δ_9	$ar{X}_{10}$	δ_{10}	$ar{X}_{11}$	δ_{11}
magnitude	0.2270	0.0036	-0.1676	-0.0031	0.1140	0.0024	-0.0659	-0.0014

Table 6.8: Estimation errors and bounds for the case of sampling-type error ($\delta = 0.0038$)

	m	$ar{oldsymbol{eta}}$	$ \delta oldsymbol{eta} $	$ \deltaeta /eta(\%)$	α
β	1	0.0317	0.0001	0.32	0.0221
(0.0316)	3	0.0318	0.0002	0.63	0.0082
	5	0.0321	0.0005	1.58	0.0056
	7	0.0324	0.0007	2.21	0.0046
	m	\bar{x}_k	$ \delta x_k $	$ \delta x_k /x_k(\%)$	ψ
x_k	$\frac{m}{1}$	\bar{x}_k 0.0204	$ \delta x_k $ 0.0004	$\frac{ \delta x_k /x_k(\%)}{2.00}$	ψ 0.0039
x_k (0.02)					
	1	0.0204	0.0004	2.00	0.0039

ror $(\delta =$	= 0.0	05)			
	m	$ar{oldsymbol{eta}}$	$ \delta eta $	α_e	α
β	1	0.0333	0.0017	0.0047	0.0291
(0.0316)	3	0.0328	0.0012	0.0018	0.0109
	5	0.0321	0.0005	0.0012	0.0073

0.0321

Table 6.9: Estimation errors and bounds for the case of random error ($\delta = 0.005$)

equation 6.16) is used to calculate the bound of estimation error. The explanation of this follows.

0.0005

0.0010

0.0060

Considering equation (6.15) and taking an effective bound $(2\delta_{eff})$ which is equal to the maximum of $|\delta_{i+m+1} - \delta_{i+m-1}|$ and $|\delta_{i+1} - \delta_{i-1}|$ yields

$$m\pi(-1)^{m+1}(\bar{X}_{i+1} - \bar{X}_{i-1})\delta\beta \le 2(1 + (-1)^{m+1}e^{-\bar{\beta}m\pi})\delta_{eff}$$
 (6.24)

From this equation, we define an effective bound on the estimation error of viscous damping, namely

$$|\delta\beta| \le \frac{2(1 + (-1)^{m+1}e^{-\bar{\beta}m\pi})\delta_{eff}}{m\pi(-1)^{m+1}|\bar{X}_{i+1} - \bar{X}_{i-1}|} = \alpha_e$$
(6.25)

In some cases, the effective bound on the measurements $2\delta_{eff}$ is significantly smaller than the upper bound 2δ . In these cases, the effective bound of the estimation error in viscous damping (α_e) is smaller compared to α . In other words, this effective bound is less conservative. However, in the real situations, the $2\delta_{eff}$ may not be known while 2δ is more feasible. In order to illustrate this, numerical examples for different types of measurement error are revisited and the results are shown in Table 6.9-6.11.

Table 6.10: Estimation errors and bounds for the case of quantization error ($\delta = 0.001$)

CITOI	<u> </u>	0.001)			
	m	$ar{oldsymbol{eta}}$	$ \deltaeta $	α_e	α
β	1	0.0322	0.00055	0.00088	0.0059
(0.0316)	3	0.0316	0.00001	0.00011	0.0022
	5	0.0318	0.00018	0.00022	0.0015
	7	0.0313	0.00028	0.00048	0.0012

Table 6.11: Estimation errors and bounds for the case of sampling-type error ($\delta = 0.0038$)

	m	$ar{oldsymbol{eta}}$	$ \delta eta $	α_e	α
β	1	0.0317	0.0001	0.0038	0.0221
(0.0316)	3	0.0318	0.0002	0.0014	0.0082
	5	0.0321	0.0005	0.0010	0.0056
	7	0.0324	0.0007	0.0008	0.0046

match perfectly with the simulated data. Two types of real systems were investigated in experimental studies, including a system which has a controllable friction source. Consistencies were shown in both the comparison between numerical simulations and experimental results, and the low estimation errors.

An industrial system was investigated to estimate the damping characteristics. Although there is no damping information provided for this system, the numerical simulation of identified model captures most of the features of the experimental results.

An error analysis addressed the effect of measurement error on the estimations. A cumulative-based approach is recommended for reducing bounds of estimations in viscous damping when this damping is small. The error bound of the dry-friction estimation depends on the estimation of viscous damping. Bounds of both estimation errors are proportional to measurement error. Numerical examples have shown the validity of error analysis results. They also showed that the bounds on the estimation errors are conservative compared to the actual estimation errors.

CHAPTER 7

SQUEAK MECHANISM OF A RUBBER-ON-STEEL CONTACT

7.1 Introduction

This chapter describes experimental investigations of the friction-induced noise problem with a rubber-on-steel contact. The study is motivated by the high-frequency "squeak" problem seen in the automobile stabilizer bar which has rubber bushings mounted on an epoxy-coated steel bar. Under some circumstances, this rubber-on-steel contact generates an annoying high-frequency frictional noise which we called squeak. A rough definition of squeak is as follows. A squeak is a high-frequency frictional noise induced by low-frequency sliding excitation. Its appearance tends to be of short-duration and intermittent which distinguishes squeak from brake squeal, which is a sustained noise.

While dry friction often generates a dissipative damping force, in some cases it is the cause of self-excited vibrations in mechanical systems such as brakes and clutches. The friction force, under some conditions, transfers energy from the steady-state sliding motion to excite and sustain limit-cycle oscillations (Dweib and D'Souza [20]). It is conceivable that the frictional noise results from resonation of the structure by means of the unstable sliding at the frictional interfaces. We will concentrate on the case where a high-pitched screaming noise occurs.

According to literature, there are many mechanisms that are suspected to be responsible for sliding instability (or self-excited vibration). These include stick-slip, sprag-slip, negative slope in the friction-velocity characteristic, and the coupling of degrees of freedom (D'Souza and Dweib [18]). A "stick-slip" self-excited vibration occurs typically in a single DOF, unidirectional belt-driven system incorporated with a specific friction property in which the kinetic coefficient is less than the static coefficient. Thus, during the sticking phase, the relative velocity at the frictional interface is zero and the elastic energy associated with the slider stiffness is stored. The energy discharges quickly during the slipping phase. As a result, the stick-slip displacement is seen as a saw-tooth waveform, as observed by Ko and Brockley [38]. The "sprag-slip" mechanism was observed by Spurr [71]. The self-excited vibrations, according to this mechanism, are induced by a "digging-in" action of the slider into the sliding interface. During the sprag phase, the slider is forced to move with the sliding surface because of the digging action. The slip commences when the friction reduces its magnitude due to the change of the inclination angle [71].

Depending on the contact materials, it is possible that the kinetic coefficient can possess a "negative slope" in a certain velocity region. For instance, Kaidanovsky and Haiken, as reported in [9], have observed the existence of a negative-slope region when sliding surface undergoes friction-induced vibrations. The negative slope can cause a stable steady sliding to become unstable, or even self-excited vibrations. Another mechanism that can induce self-excited vibration is the "coupling" of degrees of freedom. Phase angle differences can exist among the responses of different degrees of freedom. Experimental friction studies by Jarvis and Mills [35], Earles and Lee [21],

Aronov et al. [6], [4], [5], and Dweib and D'Souza [20] have illustrated that frictional sliding instability can arise due to the effect of coupling between subsystems including the tangential, normal, and torsional degrees of freedom.

Most of the previous studies on the sliding instability problems, however, adopted the unidirectional, constant-velocity sliding input. The approach also involved gradually increasing normal load. General observations from the literature can be described as the following (Aronov et al. [6], Dweib and D'Souza [20], Nakai and Yokoi [51], Tworzydlo et al. [77]). (1) The instability of sliding motion occurred when the normal load reached certain level (Aronov et al. [6], Dweib and D'Souza [20], Nakai and Yokoi [51], Tworzydlo et al. [77]). (2) Different friction behaviors can be observed depending on the magnitudes of normal load. These include the stable sliding motion characterized by small-amplitude random vibrations (light normal load), intermittent sliding motion which is characterized by irregular and short occurrences of self-excited vibrations (medium normal load), and self-excited vibrations with vibration amplitudes that are much larger than the other sliding motions (high normal load). (3) Associated with the unstable sliding motion, coupling between subsystems was often observed. (4) The magnitude of friction force changes in the transition from intermittent sliding motion to self-excited vibration. However, the change tends to be system dependent. For example, more abrupt drop of friction force was observed in the work of Aronov et al. [4], but not in the Dweib's study [20].

In accordance with these observations, a large normal load seems to be critical in generating the sliding instability. Furthermore, since these experiments focused on the unidirectional, constant-velocity input, the friction-velocity characteristics have not been examined carefully (except for the study in [51], which was a study on a metallic contact problem with unidirectional sliding input). Correlations between sound and oscillations were seldom addressed in previous investigations except for the one accomplished by Nakai and Yokoi [51]. In this chapter, we generate the unstable sliding motion with a reasonable normal load and two-directional harmonic excitations. The friction-velocity features during the unstable sliding motion will be addressed, so will be the noise-dynamics correlations.

Regarding the stabilizer bar problem, investigations have been put forth by De Togni et al. [22] in which a real system, consisting of the rubber bushing and the epoxy-coated shaft, was directly employed to study the frictional dynamics over different system parameter ranges. However, a unidirectional excitation was considered and no correlation between the noise level and dynamical responses was reported in the study. Our approach adopts the experiment system developed in this thesis which has simpler geometry in the friction contact. The study of this fundamental system can hopefully provide some guidelines for exploring the real stabilizer bar problem which possesses more complicated contact geometry and excitations.

This chapter is organized as follows. In the next section, we illustrate some experimental sliding responses and the friction-displacement and friction-velocity characteristics. These experimental results were obtained from both stable and unstable sliding conditions. We use moisture as a parameter for changing the friction characteristics and sliding stability. According to the reports in automakers, humidity is one of the important parameters in generating squeak noise. Section 7.3 focuses on the dynamical responses of unstable sliding motion. Time-domain traces are illustrated

to show the correlations between dynamical responses and sound measurements. Evidence of coupling between tangential, normal, and torsional degrees of freedom are illustrated using time-domain signals. In section 7.4, a brief conclusion is given to conclude this chapter.

7.2 Features in f- \dot{x} plots

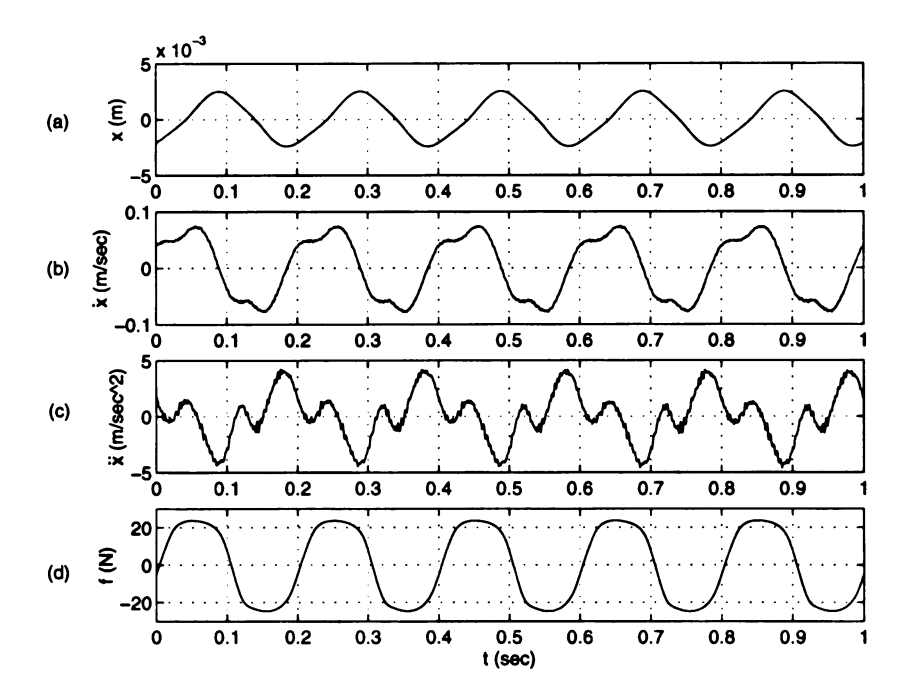


Figure 7.1: The stable sliding motion in rubber-on-steel contact, high normal-load and dry friction interface case (nominal normal load=6.13 N), $\omega = 5$ Hz, response of (a) displacement, (b) velocity, (c) acceleration, and (d) friction force.

The experimental system used in this chapter is the same as that in Chapter 2, except that two hemispheric natural-rubber contact were used to substitute for the steel ones which were used in the studies of Chapters 2, 3, and 4. Moreover, the air-track system is replaced by the linear-bearing system. The nominal normal load of the experiments addressed in this section was 6.13 N which was sensed by strain

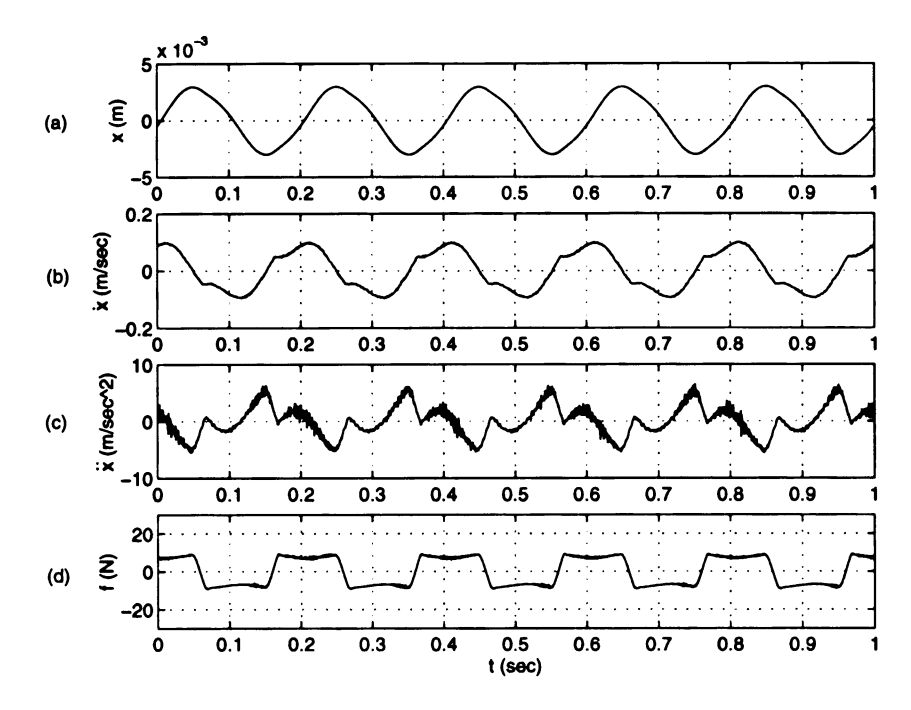


Figure 7.2: The unstable sliding motion in rubber-on-steel contact, high normal-load and wet friction interface case (nominal normal load=6.13 N) $\omega = 5$ Hz, response of (a) displacement, (b) velocity, (c) acceleration, and (d) friction force.

gauges (Measurement Group, Inc., type CEA-13-250UW-350). These strain gauges were incorporated with a signal conditioning system (Measurement Group, Inc., type 2200) and a full Wheatstone bridge configuration. The frequency of the base-motion excitation was 5.0 Hz.

According to the reports from the automakers, the squeak problem often occurs during high humidity; rubber slides on rigid and smooth surface often generates the screaming noise if the interface is wet. This agrees with our daily experience. Water was also employed as a lubricant in many friction investigations. See for instance, Aronov et al. [6], Ibrahim [33]. Therefore, we first examine the rubber-on-steel contact problem with different humidity conditions, including the one without water denoted as case 1, and the other one with the presence of water in the friction interface denoted as case 2.

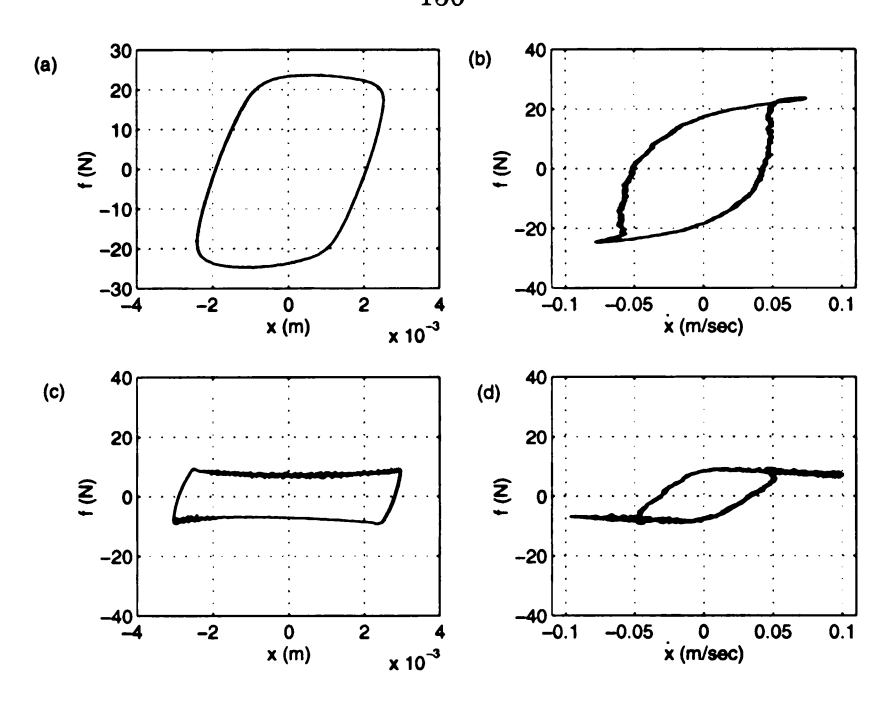


Figure 7.3: Comparison of the f-x and f- \dot{x} plots between the stable and unstable sliding motions for nominal normal load=6.13 N, (a) f-x and (b) f- \dot{x} characteristics of the stable sliding (dry friction interface), (c) f-x and (d) f- \dot{x} characteristics of the unstable sliding motion (wet friction interface).

In this section, we compare features of stable and unstable sliding motions seen in the f- \dot{x} plots for dry and wet cases. Figures 7.1 and 7.2 show two sliding experiments in which Figure 7.1 corresponds to case 1, and Figure 7.2 shows the results of case 2. The sliding motion in Figure 7.1 is stable, and that of Figure 7.2 is unstable. During the unstable sliding motion, the screaming noise occurred. Correlations between noise and dynamics will be addressed in the next section.

Although the excitations in Figures 7.1 and 7.2 are not identical, the magnitudes of motion responses $(x, \dot{x}(t), \ddot{x}(t))$ are comparable. Conversely, the friction forces of these two experiments, resulting from the same nominal normal load, are completely different. Furthermore, high-frequency vibrations appear during the sliding phase of case 2, and are evident in the acceleration and friction force traces. These high-

frequency vibrations depict the unstable sliding motion.

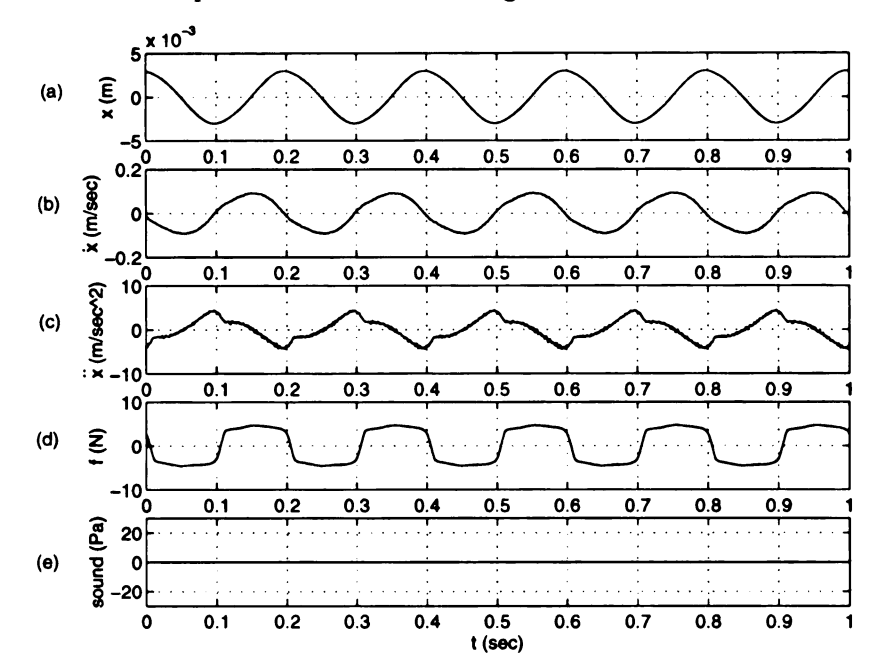


Figure 7.4: The stable sliding motion in rubber-on-steel contact, low normal-load and dry friction interface case (nominal normal load=1.23 N), $\omega = 5$ Hz, response of (a) displacement, (b) velocity, (c) acceleration, and (d) friction force.

In order to further demonstrate changes of the friction behaviors due to moisture, we plot the friction-velocity characteristics as shown in Figure 7.3 in which plots (a) and (b) present the results of case 1, whereas (c) and (d) show the results of case 2. Based on Figure 7.3, the following observations arise. (1) The average friction level decreases dramatically with the presence of water. (2) A negative slope emerges in the f- \dot{x} plot of case 2, and the case 1 has positive slope. (3) High-frequency vibrations occur during the sliding phase in case 2. This can be seen in the f-x plots shown in Figure 7.3(c). (4) The dry friction of the "linear-bearing" system is 0.413 N (Section 6.5), which is about 1/50 of the friction magnitude in case 1 and 1/20 in case 2. Moreover, the viscous damping effect of linear-bearing system is not only small ($\hat{\zeta} = 0.0177$, in Section 6.5), its effect in the f- \dot{x} plot will produce a positive

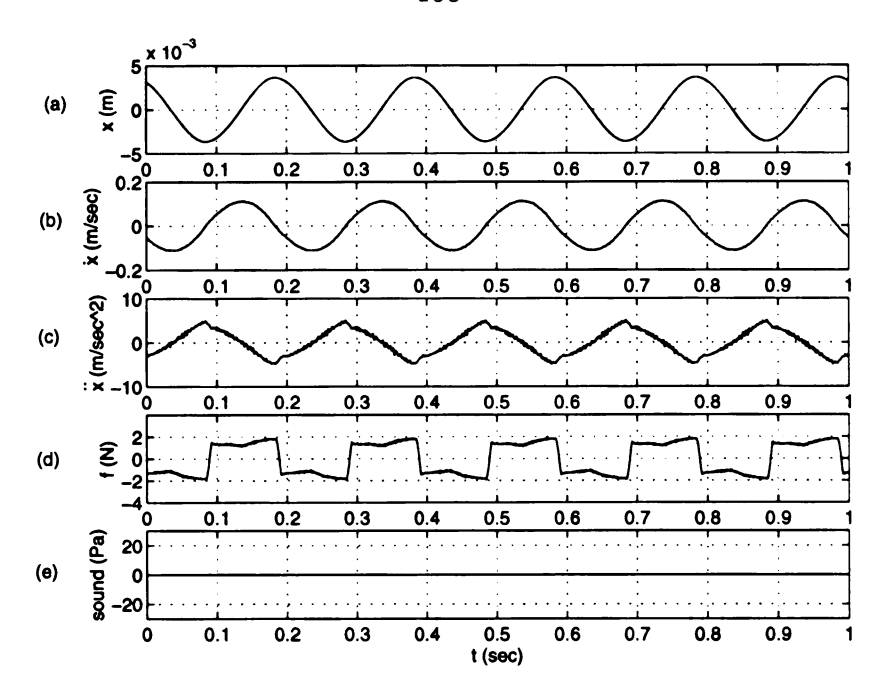


Figure 7.5: The stable sliding motion in rubber-on-steel contact, low normal-load and wet friction interface case (nominal normal load=1.23 N), $\omega = 5$ Hz, response of (a) displacement, (b) velocity, (c) acceleration, and (d) friction force.

slope. But, the viscous damping effect of the linear-bearing system does not affect the fact that the slope in the f- \dot{x} plot changes from positive to negative due to the presence of water in the friction interface.

In summary, we have found that a negative slope in the f- \dot{x} characteristic emerges when the unstable sliding motion occurs under the wet friction interface. Associated with this phenomenon is an dramatic decrease of the average friction force. The reason for these two phenomena is not clear to this point. It can be either the material change due to the presence of water or an apparent characteristic caused by elastic interactions during unstable sliding motion.

In order to clarify the mechanisms of these phenomena, we reduced the nominal normal load to 1.23 N, and conducted similar sliding experiments (with and without the presence of water). Results of these light normal load experiments are shown in

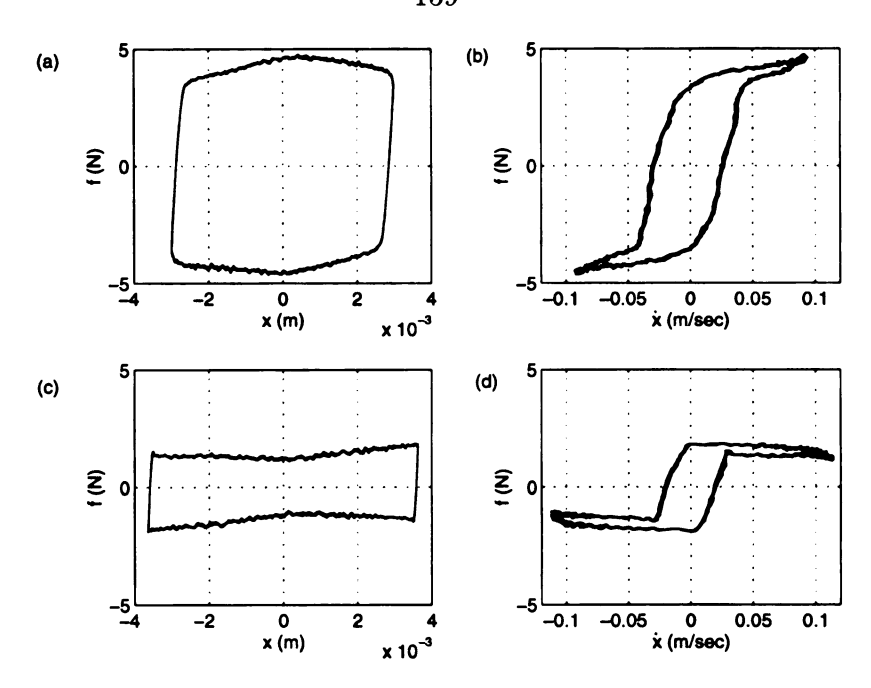


Figure 7.6: Comparison of the f-x and f- \dot{x} plots between different interface conditions for nominal normal load=1.23 N, (a) f-x and (b) f- \dot{x} characteristics of the stable sliding motion (dry friction interface), (c) f-x and (d) f- \dot{x} characteristics of the stable sliding motion (wet friction interface).

Figure 7.4-7.6. In Figures 7.4 and 7.5, we also show the sound pressure. Figure 7.4 corresponds to the case where the frictional interface is dry, whereas Figure 7.5 is the case with wet sliding interface. It can be seen in these plots that although the friction force does decrease because of the presence of water, there is no unstable sliding involved. This can be justified by the sound pressure traces in Figures 7.5 and 7.4 where no bursting of sound signal was registered.

In contrast, Figure 7.6 illustrates that the slope in f- \dot{x} changes from positive to negative in these two experiments without the occurrence of squeak. This result suggests that the presence of water in the frictional interface is responsible for the dramatical decreasing of average friction level and the negative slop observed in the f- \dot{x} plot. Furthermore, the negative slope in the f- \dot{x} characteristic is not a sufficient

condition for the sliding instability or the squeak generation.

Based on the observations from our experiments with different normal loads, a certain value of the normal load is required for the sliding instability to occur. This normal-load dependence on the sliding instability actually agrees with the previous studies which states that high normal load is a critical factor for the sliding instability (Dweib and D'Souza [20], Aronov et al. [4], Nakai and Yokoi [51]).

In the next section, we illustrate the coupling between subsystems and the correlations between dynamics and noise.

7.2 Coupling Between Subsystems

This section investigates the coupling between the dynamics of the normal, tangential, and rotational DOF systems and the correlations between dynamics effects and noise generation. In order to illustrate the existence of rotational dynamics, the torsional velocity was measured. Additionally, the normal directional acceleration was sensed by an accelerometer to show the dynamics in normal direction. Figure 7.7 depicts the configuration of these two transducers and the microphone which was used to measure sound pressure.

The torsional velocity was sensed by the laser velocity transducer (B&K, type 3544) which picked up the velocity at the end of an attached beam. The readout from the laser transducer actually has a factor relationship with the real torsional velocity. Nevertheless, the purpose of this measurement is to qualitatively illustrate the existence of the torsional dynamics during the unstable sliding motion. The data of $\dot{\theta}(t)$ presented below is the raw readout from the laser beam sensor. In contrast,

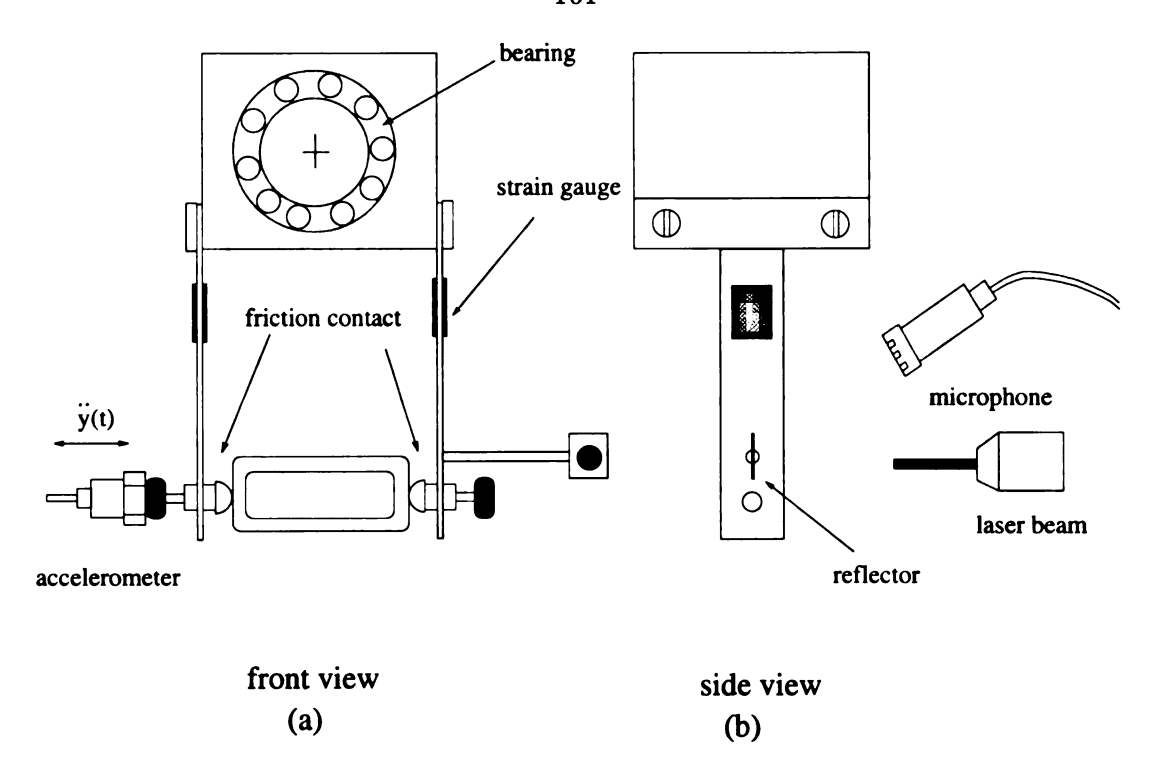


Figure 7.7: A schematic diagram showing the transducers for measuring normal and torsional vibrations, and sound pressure.

the normal acceleration was measured by the accelerometer PCB 303 A02 which has the nominal sensitivity of 10 mv/g. The sound pressure was sensed by a microphone (B&K, type 4166) with an amplifier (B&K, type 2610). The sound pressure signal was low-passed with a cut-off frequency equal to 5.0 kHz for the purpose of antialiasing. The sampling rate in this section was 10 kHz.

In Figures 7.8 and 7.9, we show the time-domain responses of the friction force, tangential acceleration, normal acceleration, torsional velocity, and sound pressure of a unstable sliding motion. Because the data acquisition system adopted here only allows for 4-channel simultaneous sampling, we recorded two sets of data separately. As can be seen in these two figures, the coupling between various degrees of freedom is evident. This feature was indicated by the fact that when the high-frequency

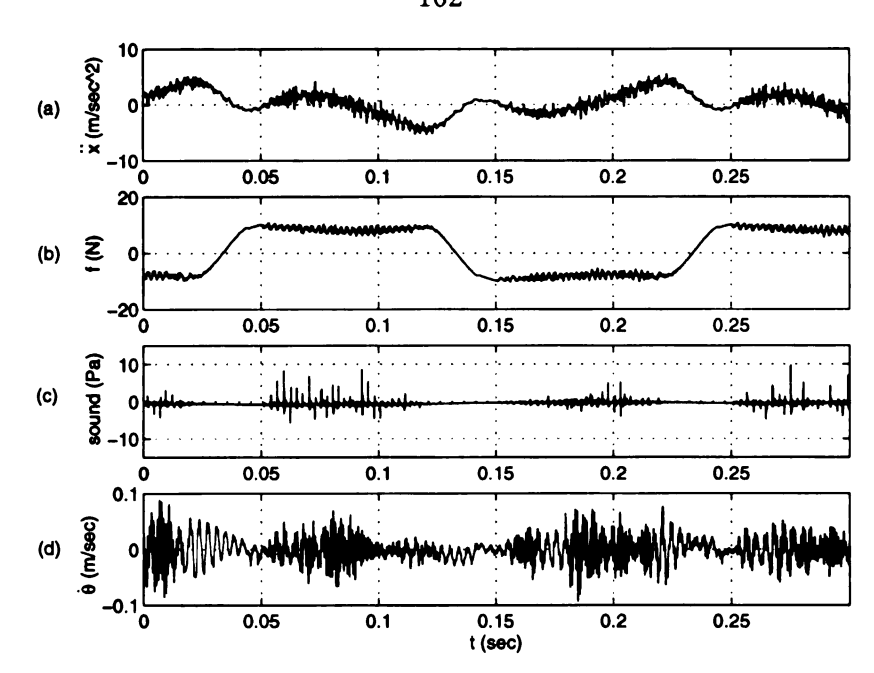


Figure 7.8: Time-domain responses of (a) tangential acceleration $\ddot{x}(t)$, (b) friction force f(t), (c) sound pressure, and (d) torsional velocity $\dot{\theta}(t)$ during unstable sliding motion, with high normal load and wet friction interface, $\omega = 5$ Hz, sampling rate=10 kHz, the sound pressure signal low-passed with 5 kHz cut-off frequency.

vibration occurs in the tangential acceleration or friction force, high-frequency events also took place in both normal and torsional signals. Moreover, the sound pressure signal shows that correlation exists between the high-frequency dynamics and the noise signal. Thus, we have demonstrated the existence of coupling between multiple DOF system and the dynamics-sound correlation. Next, we investigate the frequency contents of different signals.

A fast Fourier transform was applied to different measurements, and the results are presented in Figures 7.10 and 7.11. According to these plots, there is a harmonic below but close to 500 Hz which was registered by all spectra except the one of torsional velocity. This frequency was verified to be one of the resonant bending frequencies of the pinching beam that has friction contact engaged. Without the

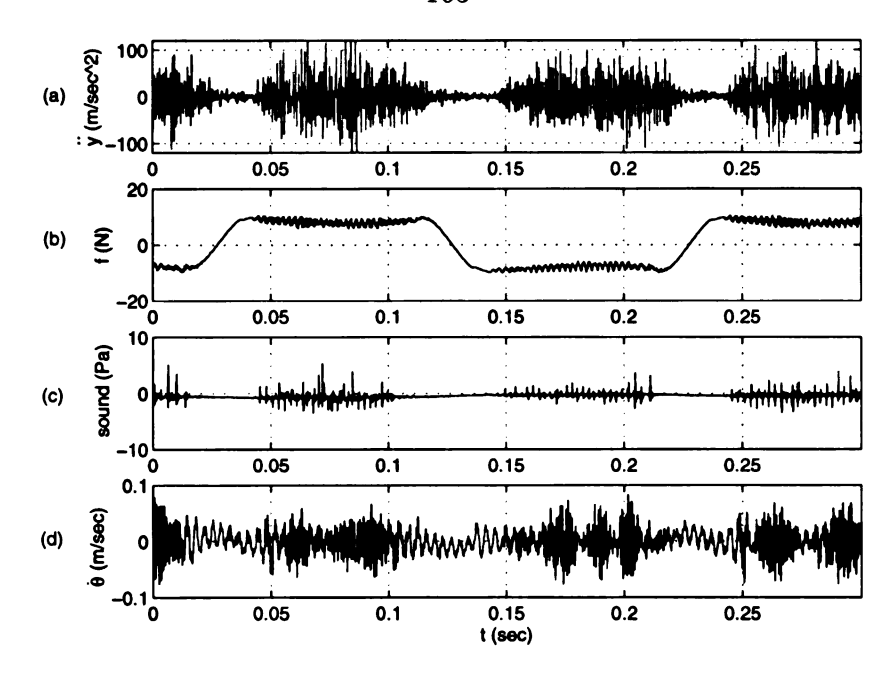


Figure 7.9: Time-domain responses of (a) normal acceleration $\ddot{y}(t)$, (b) friction force f(t), (c) sound pressure, and (d) torsional velocity $\dot{\theta}(t)$ during unstable sliding motion, with high normal load and wet friction interface, $\omega = 5$ Hz, sampling rate=10 kHz, the sound pressure signal low-passed with 5 kHz cut-off frequency.

friction contact, the fundamental bending frequency of this beam, in a clamped-free configuration, is about 185 Hz. The beam with friction contact had many resonant bending frequencies below 500 Hz, although none were obviously excited in this case. On the other hand, a 250 Hz harmonic shows up in the measurement of $\dot{\theta}(t)$. This harmonic corresponds to the fundamental bending frequency of the attached beam for mounting the reflector with the friction contact (shown in Figure 7.7). The natural frequencies mentioned above (except for the 185 Hz one) were detected with different sensors at positions shown in Figure 7.7 when harmonic excitations were input. The maximum dB value of the sound, during a squeak condition, was about 110-120 dB (when the microphone was 1 in away from the sliding surfaces), whereas the noise level of the environment was about 55 dB.

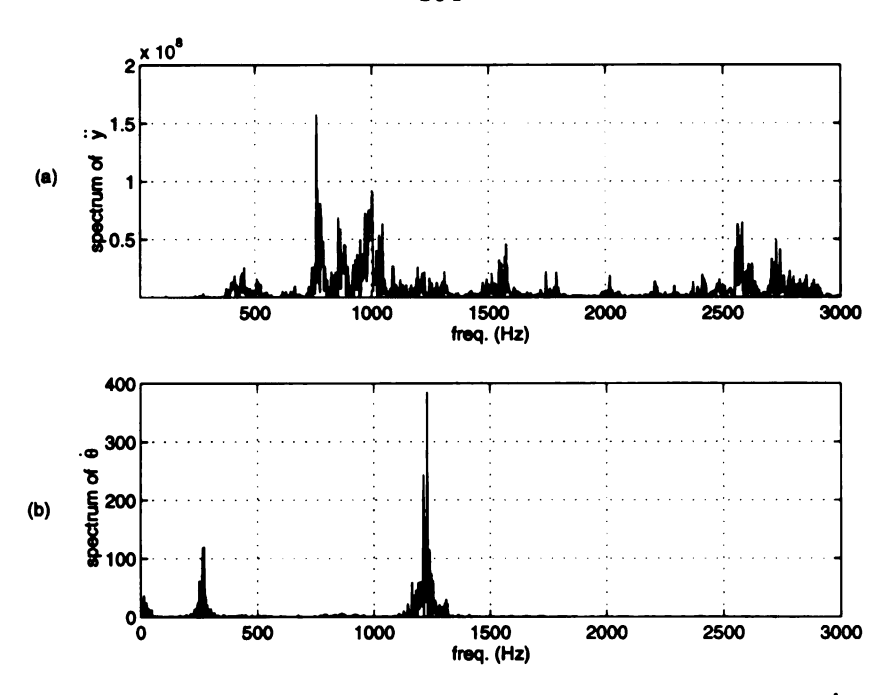


Figure 7.10: Power spectrum of (a) $\ddot{y}(t)$ in Figure 7.9, and (b) $\dot{\theta}(t)$ in Figure 7.9.

There is no evidence which points to the occurrence of an obvious frequency relationship between responses of different degrees of freedom, namely the oscillation during the unstable motion does not resemble an almost purely harmonic motion as seen in Dweib and D'Souza [20]. This differs from the investigations reported in the literature (Dweib and D'Souza [20], Aronov et al. [6] etc.). Since the contact involving the rubber has a highly nonlinear property (Rorrer [65]), it may contain different modes and coupling effects compared to metallic contact problems as addressed in [20] and [6]. More investigation is required to conclude the reason for this difference.

To this end, we have shown that the coupling effect indeed occurs with the appearance of unstable sliding motion, although simple harmonic-like motion is not observed. Moreover, correlations exist between system dynamics and noise generation. In the next section, a brief conclusion is given to discuss the possible mechanism

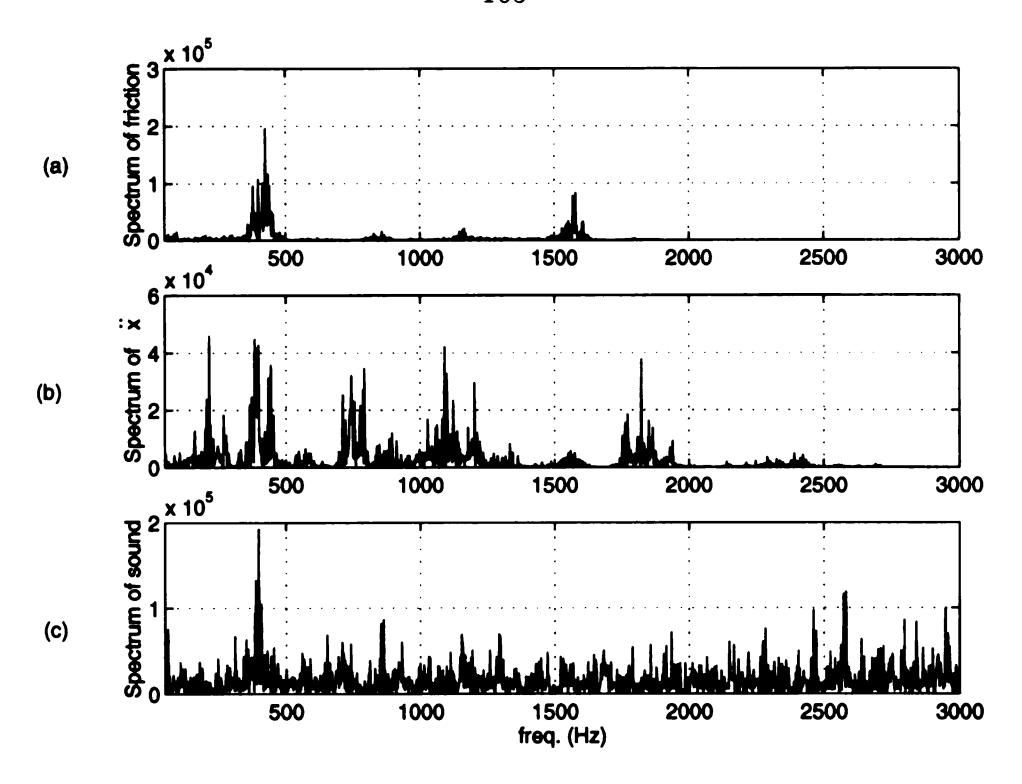


Figure 7.11: Power spectrum of (a) friction force in Figure 7.9(b), (b) $\ddot{x}(t)$ in Figure 7.8(a), and (c) sound pressure in Figure 7.9(c).

for the squeak generation in rubber-on-steel contact.

7.4 Conclusions

The observations during the occurrence of sliding instability and squeak can be summarized as follows. (1) The frictional noise is speculated to be the result of resonation of structure dynamics which is caused by sliding instability. (2) During the unstable sliding motion, the occurrence of coupling between different degrees of freedom can be observed. In order to excite this effect, a certain normal load level is required to produce sufficient friction force. (3) The presence of water in the frictional interface will facilitate the occurrence of sliding instability. The possible reason for this phenomenon is that the critical normal load may be reduced in the presence of

water. (4) Associated with this change of contact material, a dramatical decrease of average friction force occurs and the negative slope in the f- \dot{x} plot emerges.

CHAPTER 8

CLOSING REMARKS

8.1 Conclusions

In this thesis, a comparison between two common friction measurements was conducted in Chapter 2. Thorough investigations of effects of tangential contact stiffness on a harmonically forced oscillator were accomplished in Chapters 3 and 4. Chapter 3 was devoted to study the effects of contact stiffness when the mass has pure-sliding motion, whereas Chapter 4 focused on the exploration of transition oscillations and sticking dynamics. Wavelet analysis was applied to acceleration signals to examine stick-slip, transition features associated with mathematical friction models and experimental results. In Chapter 6, we proposed a new decrement method for the simultaneous estimation of dry friction and viscous damping. Through this method, damping information was identified for the linear-bearing system. The linear-bearing system was used to conduct the squeak study of the rubber-on-steel contact. This squeak problem was motivated by a frictional noise problem observed in an automobile stabilizer bar. A basic squeak mechanism for rubber-on-steel contact was proposed in Chapter 7 based on experimental observations.

Through the comparison between direct and indirect friction measurements, we have shown that while a piezoelectric load cell has been widely used in measuring

friction, it is not able to completely reflect the dynamical friction. The load cell may attenuate the high-frequency friction components to some degree. The computation approach, on the other hand, incorporating the system's ODE with motion measurements, requires more than one transducer. The drawback is that the phase shift between various transducers must be taken care of. Through careful calibration of sensors, reliable friction measurements over a reasonable frequency range can be achieved from this method. However, the frequency response of an individual sensor can always cause a phase angle when the operating range is significant compared to the sensor's resonant frequency. This phase angle may vary with the frequency content of signal as well. Thus, both direct and indirect friction measurements have limitations in application.

Among various friction isolating techniques, we adopted the air-track system in our investigation. The equivalent viscous-damping effect of this air-track system was estimated using the logarithmic decrement method. This damping effect was very small, making the air track an excellent environment for isolating the friction source. Nevertheless, there is random acoustic noise associated with the air-track system that cannot be eliminated because a certain air pressure is required to support the sliding mass. In order to study the frictional noise problem, a different anti-friction device (linear-bearing system in this study) is required.

The existence of contact compliance has been reported in friction literature. We have also observed this spring-like behavior in our experiment system. In Chapter 3, we analytically investigated an idealized compliant-contact model to predict the detailed spring-like behaviors of a frictional system subjected to harmonic excita-

tions. The transition features occurring during pure macroscopic sliding include the preliminary displacement, the transition speed, and a slanted hysteretic structure in the friction-velocity plot. The analytical predictions matched the experimental results qualitatively and quantitatively. Numerical simulations, focusing on the idealized tangential compliant-contact model, further demonstrated the reliability of this model in describing the elasto-frictional behaviors of a real system. Both the time-domain responses and the f-x and f- \dot{x} features were discussed.

There have been experimental works on friction which reported the existences of the transition oscillations during the stick-slip process. However, no detailed investigation has been offered. In Chapter 4, we first applied the tangential compliant-contact model to predict the frequency of the transition oscillation. This predicted frequency agreed with the measured frequency obtained from a free-vibration test with the contact engaged. Therefore, the high-frequency oscillations occurring during stick-slip transitions are likely to be induced by the contact compliance. Moreover, a "double" stick-slip event took place in the experimental stick-slip data. Numerical simulation based on the tangential compliant contact with light damping was used to reproduce this double stick-slip event. The mechanism associated with this double stick-slip event was discussed. The occurrence of this event implies that the transition oscillations can be more complicated than a purely sinusoidal motion.

In order to illustrate the other possible mechanism of the microscopic stick-slip process, numerical studies were given to investigate a compliant-contact problem in which both the compliance and inertial effects were included in the contact model. The contact was subjected to an imposed harmonic motion. Through simulations,

the occurrence of a high-frequency micro stick-slip event was demonstrated in this compliant contact problem. Characteristics in both time-domain responses and phase portraits were discussed.

Numerical investigations of the state-variable friction model conducted in Chapter 4 dictate that the state-variable friction model, over some parameter ranges, can give rise to the transition oscillations during a stick-slip process. However, the oscillation is not close to sinusoidal, which was observed in the experimental results as well as the simulations of tangential compliant-contact model. Furthermore, during the macroscopic sliding motion, the state-variable friction model cannot capture the microsticking event that has been observed in the experiment in Chapter 3. Lacking a physical contact mechanism, this model cannot completely describe the transition oscillations observed in a real system during the macroscopic stick-slip process. Nevertheless, a slanted hysteretic feature was found in the simulated f- \dot{x} plot. This hysteretic feature resulted from the tracking property of state-variable model. It has been shown that the degree of slanting increased with the excitation frequency if the asymptotic tracking parameters were kept constant.

The wavelet transform was applied to analyze the stick-slip transition behaviors in Chapter 5. Different transition features associated with various friction models were distinguished in the wavelet transforms. The wavelet transform also characterized the nearly sinusoidal transition oscillations and the microscale stick-slip event. A local maximum in wavelet contour plot, during each transition phase, states the nature of the nearly sinusoidal high-frequency transition oscillation. In contrast, a grouped-spike structure in the contour plot during the transition represents the

microscale stick-slip event. Comparison between the experimental stick-slip data with the simulation of the tangential contact model with light damping demonstrated good agreement in the wavelet contour plots. The efficiency of the wavelet transform as an analyzing tool in detecting the occurrence and detailed features of the high-frequency transition oscillations has been shown.

One of the motivations of this thesis is to understand the possible mechanism of the squeak problem in the rubber-on-steel contact. In order to acquire a quiet anti-friction slider system, we introduced the linear-bearing system to conduct the squeak study. However, damping exists in this linear-bearing system. Thus, we proposed a decrement method to simultaneously estimate the viscous and dry friction of the linear-bearing system. We solve the piecewise linear differential equation of the system first. A decrement equation, relating viscous-damping effect to amplitudes of a free-vibration test on this combined-damping system, was obtained. The dry friction can then be estimated based on the information of the viscous-damping. To validate the method, a numerical study was performed with known damping parameters. The damping estimations obtained from the numerical simulation matched perfectly with the given parameter values.

Two types of real systems were investigated experimentally to further show the reliability of this method. The real systems included a fundamental system and an industrial system. The fundamental system had friction source that can be isolated. In the industrial system (the linear-bearing system), in contrast, no damping information was known a priori. Experimental results showed that this decrement method is very efficient in estimating damping information from the fundamental

system. Consistencies appeared in the comparison between the experimental data and the numerical simulations based on the estimated damping parameters. Furthermore, low estimation errors occurred in the estimations of viscous damping. The experiments of the linear-bearing system illustrated that this system has low viscous damping with a certain amount of dry friction.

An error analysis was carried out to account for effects of measurement error on the estimation results. Bounds on estimation error were achieved using Taylor series expansions. Relationships between measurement error and bounds of estimation error were studied. It was found that, for a low viscous damping case, a cumulative selection of amplitudes gave a smaller bound of the estimation error in the viscous damping factor. The error bound of the dry-friction estimation depends on the viscous-damping estimation. Numerical experiments have been performed to validate the results of error analysis. Reliabilities of different bounds were demonstrated, as were the calculation procedures.

In Chapter 7, we focused on a rubber-on-steel contact problem in which the frictional noise study was accomplished. This problem was motivated by the squeak noise seen in stabilizer bar of automobile. Compared to the friction levels in the squeak experiments, the dry friction effect of the linear-bearing system is negligible. Moreover, the viscous damping effect did not affect the observations obtained in the squeak investigations. Different moisture conditions were examined in order to search for proper mechanism of squeak generation.

The frictional noise was found to be a result of structure resonation due to the unstable sliding motion taking place in the frictional interface. There are many pos-

sible mechanisms responsible for the unstable sliding motion, and the one that we found in the rubber-on-steel contact was the coupling between different degrees of freedom. To excite this coupling effect, a certain level of friction force is required. This was shown by experiments with different normal loads, and consequently, different friction force levels. It ended up that the sliding motion with light normal load was stable even though a negative slope appeared in the f- \dot{x} plot due to the presence of water in friction interface. This result dictates that large friction force is required to excite the coupling between subsystems, which is consistent with the results addressed in the literature (Aronov [4], Dweib and D'Souza [20], Nakai and Yokoi [51]).

Including water in friction interface dramatically decreased the friction level and induced a negative slope in the f- \dot{x} plots. While neither the moisture nor the negative slope in the f- \dot{x} seemed to be a sufficient condition in generating the coupling between different degrees of freedom, the moisture probably caused a change of the critical normal load (or friction force) at which the instability occurred. Thus, the system behaved differently with the presence of water. In summary, the frictional noise resulted from the resonation of structure dynamics which in turn was caused by the coupling between degrees of freedom. To excite this coupling, a certain level of friction was required.

8.2 Future Studies

In the study of compliant-contact problem, we have shown the consistencies between analytical and experimental results for the harmonic excitation case. However, the tangential contact model was incorporated with Coulomb law in the sliding regime. Many boundary-lubricated systems may not possess such a friction characteristic, it is therefore of interest to extend the idea of compliant contact to other steady-state friction features such as the Stribeck law. Moreover, many previous research works have also shown the existence of the frictional memory effect in the sliding regime (Rice and Ruina [63], Hess and Soom [28] etc.). To describe the frictional memory effect, either the state-variable or the time-delay friction model is a possible candidate. Thus, the modeling efforts can integrate different steady-state friction characteristics with the state-variable or time-delay friction model for describing the boundary-lubricated systems.

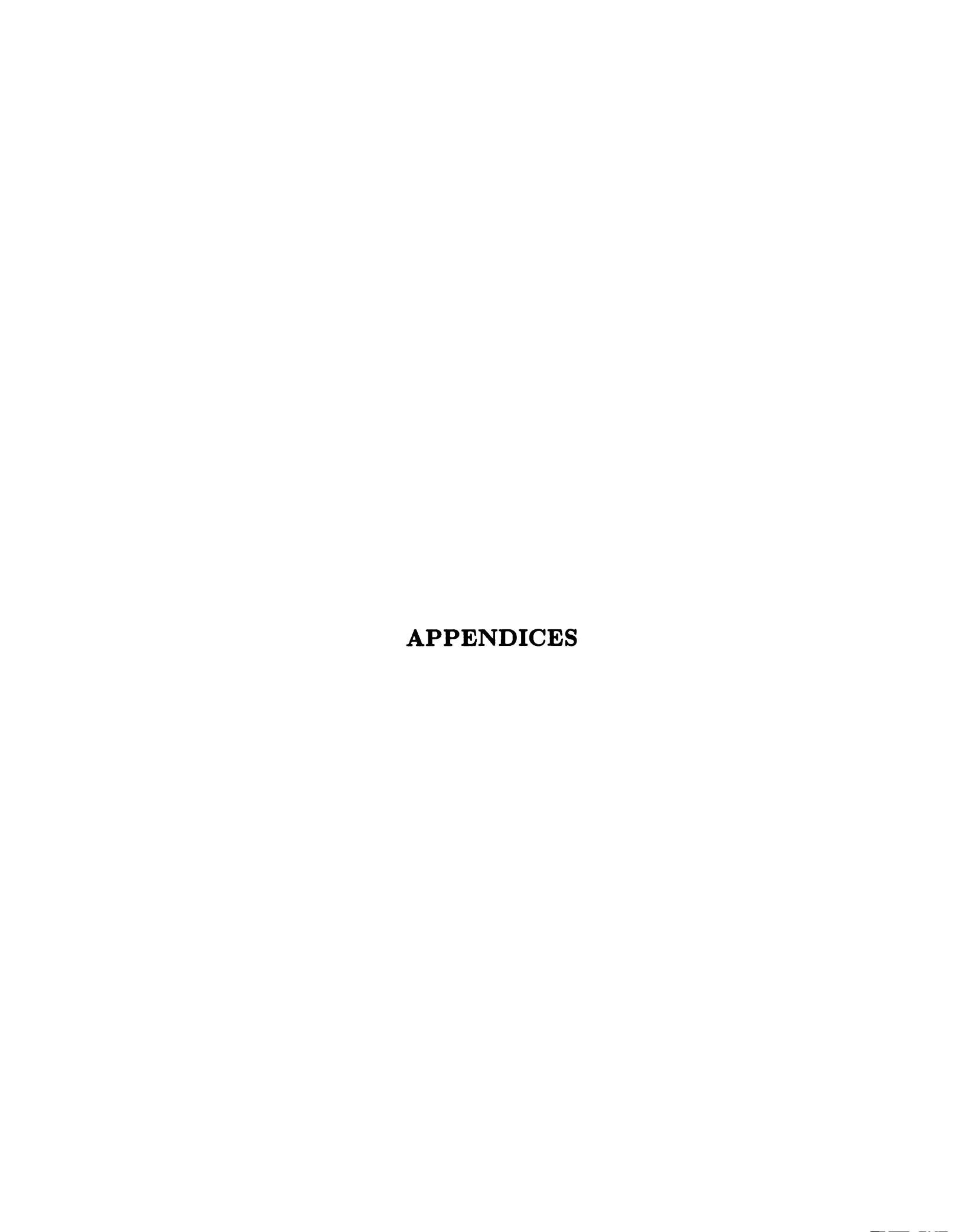
The study of the compliant contact problem can also be extended to different material combinations at the contact such as Teflon-on-steel, aluminum-on-steel etc. The microsticking behaviors with different contact materials can be investigated. It is conceivable that the elastic deformation process during the microsticking process is not necessary to be nearly linear for different material combinations.

More work can be accomplished in the investigations of the high-frequency transition oscillations. For instance, different contact geometry and normal load may affect the oscillation frequency and the appearance of micro scale stick-slip event. In addition, the high-frequency microscale stick-slip event can conceptually be a mechanism of high-frequency frictional noise, while it calls for more investigations. The study in transition oscillation can also provide selection considerations for the dither signal which can be used to eliminate the stick-slip process in control applications.

In studying the frictional noise problem, an actuator capable of generating long-

stroke harmonic functions in high normal load is important. As mentioned before, a high normal load is critical for the occurrence of coupling effect between different subsystems. Unfortunately, most of the commercial shakers can only provide short strokes (about 1 in). In order to be able to generate long-stroke harmonic motions, a motor-drive system incorporated with some mechanism for converting rotating motion into rectilinear motion can be considered.

Regarding the squeak study in rubber-on-steel contact, modeling can include different degrees of freedom, such as tangential, rotational, and normal coordinates. Although some work has been done by Dweib and D'Souza [20] to show the dependence of stability on the normal load, the system considered in that study did not have a negative slope in the friction-velocity relationship. It is of interest to understand how the coupling effect between different subsystems can overrule the negative damping effect in the tangential direction of motion, so that the sliding motion is stable when the normal load is low (Figures 7.4-7.6). Tworzydlo [77] applied Oden and Martins' friction model with coupling effects between different coordinates. While this work can predict unstable sliding motion, the features seem to be different from our study. For example, in [77], collapse of the natural frequency between rotational and normal degrees of freedom was shown to be critical. However, we did not observe this event in our experiments. Moreover, most of the previous research work focusing on the metallic contact which is different from the contact in this study.



APPENDIX A

THE MOVING AVERAGE METHOD

The moving average method has been broadly used in data filtering or smoothening applications (Dupont [19] and Sakamoto [67]). In this dissertation, we differentiated displacement signal in order to obtain the velocity response. Due to the quantization process and sampling theorem, noise associated with this differentiation process is inevitable. Thus, a five-point moving algorithm was employed to smoothen the signal after differentiation process. While many moving average methods exist, the five-point algorithm has been shown to have best compromise between phase shift and smoothening effects (Sakamoto [67]). This method can be described as follows.

For a data sequence $y_i, i = 1, 2.., n$, the equations for computing averages are

$$\bar{y}_i = \frac{1}{5}(y_{i-2} + y_{i-1} + y_i + y_{i+1} + y_{i+2}) \quad i = 2, 3, ..., n - 2$$

$$\bar{y}_0 = \frac{1}{5}(3y_0 + 2y_1 + y_2 - y_4)$$

$$\bar{y}_1 = \frac{1}{10}(4y_0 + 3y_1 + 2y_2 + y_3)$$

$$\bar{y}_{n-1} = \frac{1}{10}(y_{n-3} + 2y_{n-2} + 3y_{n-1} + 4y_n)$$

$$\bar{y}_n = \frac{1}{5}(-y_{n-4} + y_{n-2} + 2y_{n-1} + 3y_n)$$
(A.1)

Equation (A.1) shows that each averaged datum is the mean value of five surrounding data points. There are special formulations for both the first and the last

two points.

The moving average method can be considered as a low-passed filter. Thus, it has frequency response and phase relationship between the input and output data. In order to understand the frequency-domain characteristic of the five-point moving average method, a discrete-time Fourier transform is taken with respect to the formulation for a general data point "i" to achieve

$$H(\omega) = 1/5(2\cos(2\omega) + 2\cos(\omega) + 1).$$
 (A.2)

Based on this equation, the magnitude and phase responses can be depicted as Figure A.1 in which the phase angle changes due to the fact that the magnitude of $H(\omega)$ has different sign.

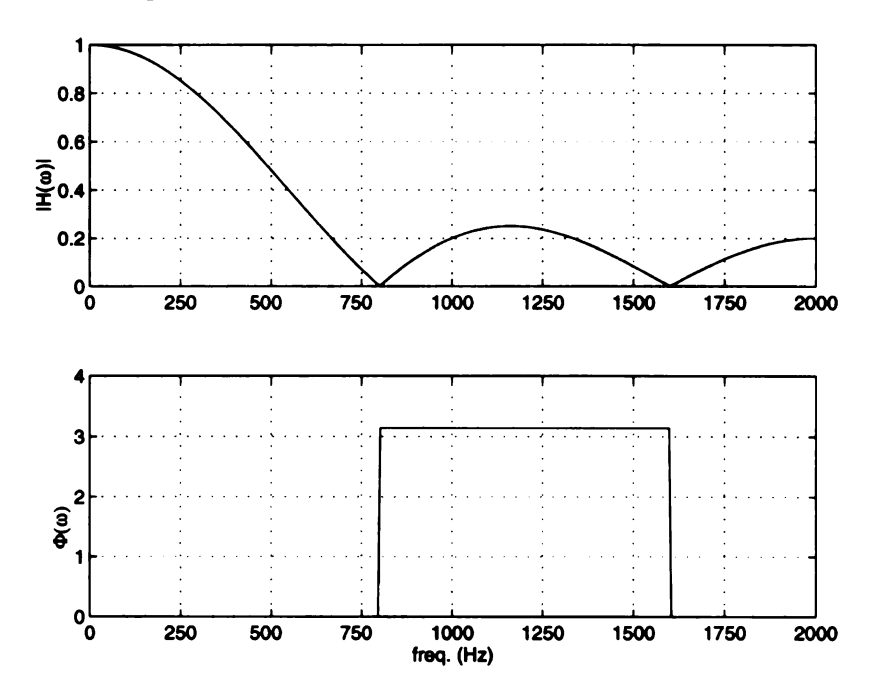


Figure A.1: Magnitude and phase response of five-point moving average method.

In Figure A.1, the frequency range is 2 kHz, which is called the folding frequency and is equal to half of the typical sampling frequency (4 kHz) using in this thesis.

As expected, the moving average method possesses a low-pass filter characteristic. In addition, consider the facts that we applied this method to the velocity signal which does not have very high frequency content, and the method causes zero phase in the frequency range less than 750 Hz, it can be concluded that this method will not introduce severe phase problem to the velocity data.

APPENDIX B

DISCHARGE CHARACTERISTIC OF LOAD CELL

B.1 Discharge Time Constant

In the application of piezoelectric load cell, a long discharge time constant (DTC) is necessary for a low-frequency response. The DTC is defined as the time required for a sensor or measuring system to discharge its signal to 37% of the original value from a step change of the signal. This time constant directly relates to the low-frequency measuring capacity for both transient and sinusoidal events. In order to take full advantage of the long DTC built into the force sensor or the accelerometer, it is best to DC couple from the sensor to the readout device. When DC coupling a system, it is important to DC couple the entire system and not just the sensor to the signal conditioner.

In our instrumentation, signal conditioner PCB482B was adopted for DC coupling the load cell and the data acquisition unit (Masscomp, 5550). The DTC for the load cell (PCB 208B) was 50 seconds. On the other hand, the signal conditioner (PCB 482A10) was used to DC coupling the accelerometer and the data acquisition unit. In both cases, data acquisition unit were set to DC coupling mode so that there was no AC coupling involved in the entire system.

B.2 Decay Rate in the Low-Frequency Signal Measurement

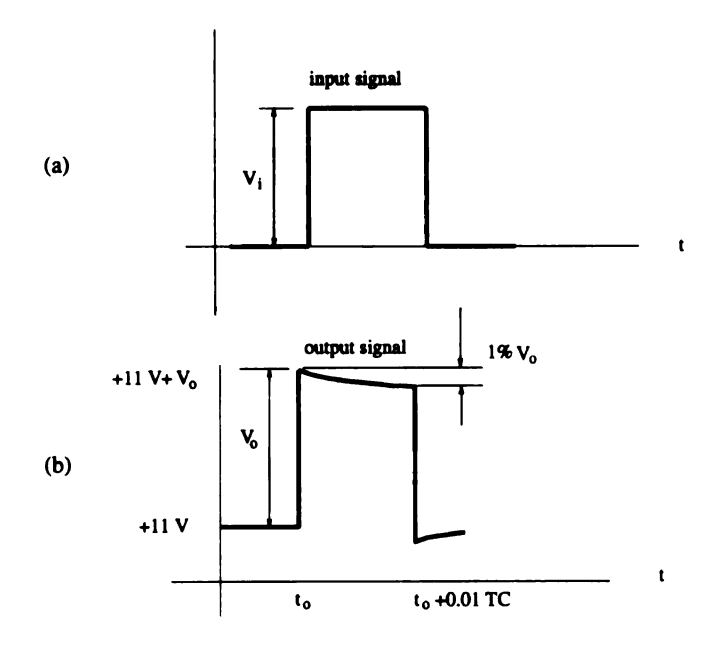
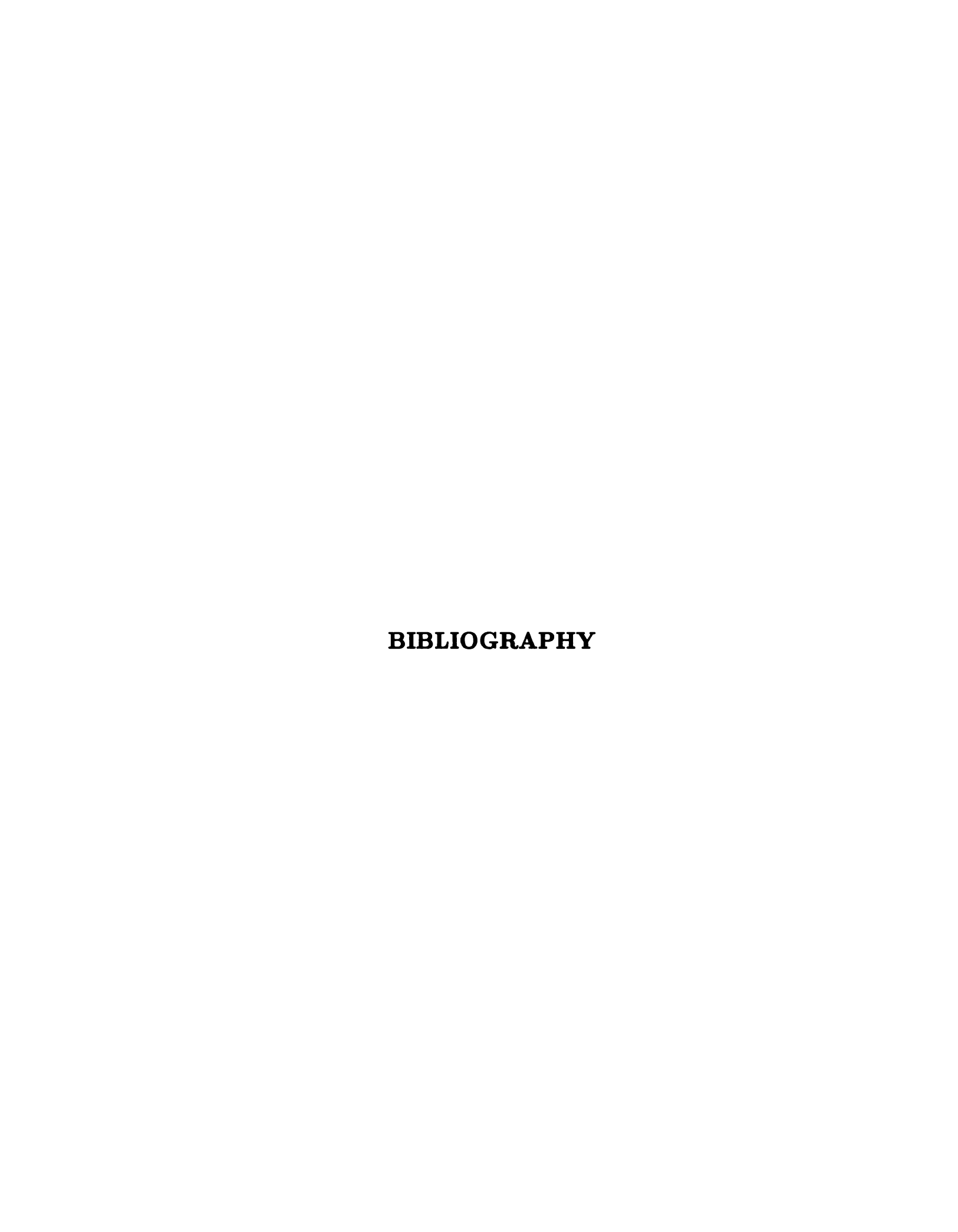


Figure B.1: A schematic diagram showing the discharge characteristic.

Under the DC coupling of the measuring system, the signal will eventually decay to zero. However, the decaying speed was kept as slow as possible to achieve a good reading. For instance, in the load cell application, the rule of thumb for the signal discharge is as follows. For the first 10% of the discharge time constant, the signal lost is approximately proportional to the time elapsed. Which dictates that if the DTC of the load cell is 50 seconds, the signal will lose approximately 10% of its output level 5 seconds (10% of 50) after the application of a steady-state force within the measuring range. A schematic diagram depicting this discharging event is presented in Figure B.1 in which the 11 volt DC level represents the bias elimination range to prevent the input DC bias.

In our experimental study, intervals of "steady" friction forces appeared in the macroscopic stick-slip process. The lowest oscillation frequency of the stick-slip pro-

cess was 2.5 Hz. Therefore, the maximum duration of a steady friction force interval is 0.2 sec. Based on the DTC of the load cell (PCB 208B), this maximum duration corresponds to 0.4% of the DTC. Thus, at most 0.4% of the original friction level has drifted during a steady sliding interval. Consider a typical case in previous study which has a friction force of 1 N. The drifted value of this case will be less than 0.004 N which is small. The acceleration measurement does not have similar interval of steady response, so that there is no drift problem associated with it.



BIBLIOGRAPHY

- [1] Allen, J. B. and L. R. Rabiner 1977. A unified approach to short-time fourier analysis and synthesis. In *Proc. IEEE*, Vol. 65, No. 11 1558-1564.
- [2] Antoniou, S. S., A. Cameron, and C. R. Gentle 1976. The friction-speed relation from stick-slip data. Wear 36:235-254.
- [3] Armstrong-Hélouvry, B., P. Dupont, and C. CanudasdeWit 1994. A survey of methods, analysis tools and computation methods for the control of machines with friction. *Automatica* 30(7):1083-1138.
- [4] Aronov, V., A. D'Souza, S. Kalpakjian, and I. Shareef 1984. Interactions among friction, wear, and system stiffness-part 1: Effect of normal load and system stiffness. *Journal of Tribology* 106:54-58.
- [5] Aronov, V., A. D'Souza, S. Kalpakjian, and I. Shareef 1984. Interactions among friction, wear, and system stiffness-part 2: Vibrations induced by dry friction. *Journal of Tribology* 106:59-69.
- [6] Aronov, V., A. F. D'Souzza, S. Kalpakjian, and I. Shareef 1983. Experimental investigation of the effect of system rigidity on wear and friction-induced vibrations. *Journal of Lubrication Technology* 105:206-211.
- [7] Bell, R. and M. Burdekin 1966. Dynamic behavior of plain slideways. Proc. of the Instn. of Mechanical Engineers 181, pt. 1(8):169-183.
- [8] Brandenburg, G. and U. Schäfer 1991. Influence and compensation of coulomb friction in industrial pointing and tracking systems. In *Proc. of the Indus. App. Soc. Annual Meeting, IEEE* 1407-1413. Dearbon, MI.
- [9] Brockley, C. A. and P. L. Ko 1970. Quasi-harmonic friction-induced vibration. Journal of Lubrication Technology, Trans. of the ASME 550-556.
- [10] CanudadeWit, C., H. Olsson, K. J. Astrom, and P. Lischinsky 1995. A new model for control of systems with friction. *IEEE Transactions on Automatic* Control 40(3):419-425.
- [11] Chen, D. J. and W. J. Wang 1995. Pattern changes of time-shifted vibration signals on wavelet time-scale maps. In DE-Vol, 84-1, 1995 Design Engineering Technical Conference Volume 3-Part A, ASME 1345-1349.
- [12] Coulomb, C. A. Theorie des machines simples. Paris.

- [13] Courtney-Pratt, J. and E. Eisner 1957. The effect of a tangential force on the contact of metallic bodies. *Proc. Royal Society* A238:529-550.
- [14] Dahl, P. 1968. A solid friction model. Tech. Rep. TOR-0158(3197-18)-1. E1 Segundo, CA: Aerospace Corp.
- [15] Den-Hartog, J. P. 1930. Forced vibration with combined coulomb and viscous damping. Transactions of the American Society of Mechanical Engineering 53:107-115.
- [16] Dieterich, J. H. Modeling of rock friction: 1. experimental results and constitutive equations. J. Geophys. Res. 84 (B5):2161-2168.
- [17] Dieterich, J. H. 1991. Micro-mechanics of slip instabilities with rate- and statedependent friction. volume Fall Meeting Abstract Volume 324. Eos, Trans. Am. Geeophys. Union.
- [18] D'Souza, A. F. and A. H. Dweib 1990. Self-excited vibrations by dry friction, part 2: Stability and limit-cycle analysis. *Journal of Sound and Vibration* 137(2):177-190.
- [19] Dupont, P. E. and E. P. Dunlap 1995. Friction modeling and pd compensation at very low velocities. *Journal of Dynamic Systems, Measurement, and Control, Trans. of the ASME* 117:8-14.
- [20] Dweib, A. H. and A. F. D'Souza 1990. Self-excited vibrations by dry friction, part 1: Experimental study. *Journal of Sound and Vibration* 137(2):163-175.
- [21] Earles, S. W. E. and C. K. Lee 1976. Instabilities arising from the frictional interaction of a pin-disk system resulting in noise generation. *Journal of Engineering for Industry* 81-86.
- [22] Eiss, R. S. D. T. N. S. and R. A. L. Rorrer 1992. The role of system dynamics on the behavior of elastomeric friction. In *Wear and Friction of Elastomers*, ASTM Special Technical Publication number 1145 30-49.
- [23] Feeny, B. F. 1992. A nonsmooth coulomb friction oscillator. Physica D 59:25-38.
- [24] Feeny, B. F. and J. W. Liang 1996. A decrement method for the simultaneous estimation of coulomb and viscous friction. *Journal of Sound and Vibration*.
- [25] Feeny, B. F. and F. C. Moon 1994. Chaos in a dry-friction oscillator: Experiment and numerical modeling. *Journal of Sound and Vibration* 170:303-323.
- [26] Harnoy, A., B. Friedland, and H. Rachoor 1994. Modeling and simulation of elastic and friction forces in lubricated bearing for precise motion control. Wear 172:155-165.

- [27] Helmholtz, H. L. F. 1954. On the Sensations of Tone as a Physical Basis for the Theory of Music.: Dover, New York, translation by A. J. Ellis of Die Lehre von dem Tonempfindungen, fourth edition, 1877, first edition published in 1863.
- [28] Hess, D. P. and A. Soom 1990. Friction at a lubricated line contact operating at oscillating sliding velocities. *Journal of Tribology* 112:147-152.
- [29] Hsu, G. Stochastic Modeling and Identification of Friction Dynamics from Noise Data. PhD thesis Mechanical Engineering, The University of Michigan 1995.
- [30] Hundal, M. S. 1985. Response of a base excited system with coulomb and viscous friction. *Journal of Sound and Vibration* 64:371-378.
- [31] Hunt, H. E. M. 1995. Monitoring offshore pipelines using forced transverse vibration: Data analysis. In DE-Vol, 84-1, 1995 Design Engineering Technical Conference Volume 3-Part A, ASME.
- [32] Ibrahim, R. A. 1992. Friction-induced vibration, chatter, squeal, and chaos: Part i mechanics of friction, asme. volume DE-Vol. 49 107-121.
- [33] Ibrahim, R. A. 1992. Friction-induced vibration, chatter, squeal, and chaos: Part ii dynamics and modeling, asme. volume DE-Vol. 49 123-138.
- [34] Ioannou, P. A. and J. Sun 1995. Robust Adaptive Control.: Printice-Hill.
- [35] Jarvis, R. P. and B. Mills 1963-64. Vibration induced by dry friction. In Proceedings of the Institution of Mechanical Engineers volume 175(32).
- [36] Kato, S., N. Sato, and T. Matsubayshi 1972. Some considerations on characteristics of static friction of machine tool slideway. *Journal of Lubrication Technology* 94:234-247.
- [37] Kishimoto, K., H. Inoue, M. Hamada, and T. Shibuya 1995. Time frequency analysis of dispersive waves by means of wavelet transform. *J. of Applied Mechanics* 62:841-846.
- [38] Ko, P. L. and C. A. Brockley 1970. The measurement of friction and friction-induced vibration. *Journal of Lubrication Technology* 543-549.
- [39] Li, C. J. and J. Ma 1992. Bearing localized defect detection through wavelet decomposition of vibrations. In Sensors and Signal Processing for Manufacturing volume PED-Vol, 55 187-195.
- [40] Liang, J. W. and B. F. Feeny 1995. Wavelet analysis of stick-slip in an oscillator with dry friction. In Friction Damping and Friction-Induced Vibration volume DE-Vol. 84-1, Vol.3 Part A. Boston, Massachusetts.
- [41] Lorenz, H. Lehrbuch der Technischen Physik. Erster Band: Technische Mechanik starrer Gebilde. Berlin: Verlag von Julius Springer.

- [42] Makris, N. and M. C. Constantinou 1991. Analysis of motion resisted by friction. i. constant coulomb and linear/coulomb friction. *Mech. Struct. and Mach.* 19(4):477-500.
- [43] Maqueira, B. and M. K. Masten 1993. Adaptive friction compensation for line-of-slight pointing and stabilization. In *Proc.* 1993 American Control Conference 1942-1946. San Francisco, CA.
- [44] Marui, E. and S. Kato 1984. Forced vibration of a base-excited single-degree-of-freedom system with coulomb friction. *Journal of Dynamic Systems, Measurement, and Control* 106:280-285.
- [45] Meijaard, J. P. 1994. Efficient simulation of systems with discontinuities and time-varying topology,. Blacksburg.
- [46] Meirovitch, L. 1986. Elements of Vibration Analysis. : McGraw-Hill, Inc. 2nd edition edition.
- [47] Mooney, J. A. and A. Soom 1995. Optimal windows for the time-frequency analysis of arbitrary swept frequency signals. In *DE-Vol*, 84-1, 1995 Design Engineering Technical Conference Volume 3-Part A 1351-1362.
- [48] Morin, A. J. 1833. New friction experiments carried out at metz in 1831-1833. Proc. of the French Royal Academy of Science 4:1-128.
- [49] Morlet, J., G. Arens, E. Fourgeau, and D. Giard 1982. Wave propagation and sampling theory-part i: Complex signal and scattering in multi-layered media. *Geophysics* 47:203-221.
- [50] Morlet, J., G. Arens, E. Fourgeau, and D. Giard 1982. Wave propagation and sampling theory-part ii: Sampling theory and complex waves. *Geophysics* 47:222-236.
- [51] Nakai, M. and M. Yokoi 1990. Generation mechanism of friction noise in dry friction. *Japanese Journal of Tribology* 35(5).
- [52] Newland, D. E. 1994. Wavelet analysis of vibration part 1: Theory. *Journal of Vibration and Acoustics* 116:409-416.
- [53] Newland, D. E. 1994. Wavelet analysis of vibration part 2: Wavelet maps. Journal of Vibration and Acoustics 116:417-425.
- [54] Oden, J. T. and J. A. C. Martins 1985. Models and computational methods for dynamic friction phenomena. *Comput. Meth. Appl. Mech. Eng.* 52(1-3):527-634.
- [55] Onsay, T. and A. G. Haddow 1994. Wavelet transform analysis of transient wave propagation in a dispersive medium. J. Accoust. Soc. Am. 95(3):1441-1449.

- [56] Polycarpou, A. and A. Soom 1992. Transitions between sticking and slipping at lubricated line contacts. In *Transitions Between Sticking and Slipping at Lubricated Line Contacts* volume DE-Vol 49 139-148.
- [57] Polycarpou, A. A. and A. Soom 1995. Boundary and mixed friction in the presence of dynamic normal loads: Part ii- friction transients. *Journal of Tribology* 117:261-266.
- [58] Popp, K. 1992. Some model problems showing stick-slip motion and chaos. In Friction-Induced Vibration, Chatter, and Squeal volume DE-Vol 49 1-12. ASME Winter Annual Meeting.
- [59] Portnoff, M. R. 1980. Time-frequency representation of digital signals and systems based on short-time fourier analysis. *IEEE Transactions on Acous.*, Speech, Signal Proc. 28:55-69.
- [60] Rabinowicz, E. 1958. The intrinsic variables affecting the stick-slip process. Proc. Physical Society of London 71:668-675.
- [61] Radcliffe, C. J. and S. C. Southward 1990. A property of stick-slip friction models which promotes limit cycle generation. In Proc. 1990 Ameican Control Conference, ACC 1198-1203. San Diego, CA.
- [62] Rayleigh, L. 1877. The Theory of Sound.: reprinted by Dover, New York, 1945, I:46-51.
- [63] Rice, J. R. and A. L. Ruina 1983. Stability of steady friction slipping. J. of Applied Mechanics 50:343-349.
- [64] Rioul, O. and M. Vetterli 1991. Wavelet and signal processing. In *IEEE SP Magazine* 14-38.
- [65] Rorrer, R. A. L. 1995. Friction-induced vibration of multi-degree of freedom sliding subsystems. In *Design Engineering Technical Conference* volume DE-Vol. 84-1, Volume 3-Part A 1179-1186. Boston.
- [66] Ruina, A. Friction Laws and Instabilities A Quasistatic Analysis of Some Dry Frictional Behavior. PhD thesis Division of Engineering Brown University 1980.
- [67] Sakamoto, T. 1985. Normal displacement of the sliding body in a stick-slip friction process. In PROCEEDINGS OF THE JSLE INTERNATIONL TRI-BOLOGY CONFERENCE 141-146.
- [68] Sakamoto, T. 1987. Normal displacement and dynamical friction characteristics in a stick-slip process. *Tribology International* 20(1):25-31.
- [69] Shaw, S. W. 1986. On the dynamic response of a system with dry friction. Journal of Sound and Vibration 108:305-325.

- [70] Southward, S. C., C. J. Radcliffe, and C. R. MacCluer 1991. Robust nonlinear stick-slip friction compensation. ASME J. of Dynamic Systems, Meaurement and Control 113(4):639-645.
- [71] Spurr, R. T. 1961-1962. A theory of brake squeal. In Proc. Auto. Div. Instn. Mech. Engrs. 33-40.
- [72] Stry, G. I. and D. J. Mook 1992. An experimental study of nonlinear dynamic system identification. *Nonlinear Dynamics* 3:1-11.
- [73] Suzuki, A. and M. Tomizuka 1991. Design and implementation of digital servo controller for high speed machine tools. In *Proc. 1991 American Control Conference*, AACC 1246-1251. Boston, MA.
- [74] Tansel, I. N., C. Mekdeci, and C. McLaughlin 1993. Detection of tool failure in end milling with wavelet transformations and neural networks (wt-nn). In Manufacturing Science and Engineering, ASME volume PED-Vol. 64 369-374.
- [75] Tolstoi, D. M. 1967. Significance of the normal degree of freedom and natural normal vibrations in contact friction. Wear 10:199-213.
- [76] Tworzydlo, W. W. and E. Becker 1991. Influnce of forced vibrations on the static coefficient of friction numerical modelin. Wear 143:175–196.
- [77] Tworzydlo, W. W., E. B. Becker, and J. T. Oden 1992. Numerical modeling of friction-induced vibrations and dynamic instabilities. In *Friction-Induced Vibration*, Chatter, Squeal, and Chaos, ASME Winter Meeting volume DE-Vol. 49 13-32.
- [78] Vetterli, M. and C. Herley 1992. Wavelet and filter banks: Theory and design. *IEEE Transactions on Signal Processing* 40(9):2207-2232.
- [79] Williams, J. R. and K. Amaratunga 1994. Introduction to wavelets in engineering. International Journal for Numerical Methods in Engineering 37:2365-2388.
- [80] Wojewoda, J. and T. Kapitaniak 1992. Chaotic behavior of friction force. International Journal of Bifurcation and Chaos 2(1):205-209.